Tutorial Vol. 14, No. 1 / March 2022 / Advances in Optics and Photonics 87

Advances in Optics and Photonics

Rogue waves in nonlinear optics

M. Tlidi[1] and M. Taki[2,*]

[1] Faculté des Sciences, Université Libre de Bruxelles (U.L.B), CP 231, Campus Plaine, B- 1050 Bruxelles, Belgium
[2] Université de Lille, CNRS, UMR 8523 PhLAM - Physique des Lasers Atomes et Molécules, F-59000 Lille, France
*Corresponding author: abdelmajid.taki@univ-lille.fr

Received July 15, 2021; revised December 28, 2021; accepted January 10, 2022; published 24 March 2022

Understanding the phenomenon of rogue wave formation, often called extreme waves, in diverse branches of nonlinear science has become one of the most attractive domains. Given the great richness of the new results and the increasing number of disciplines involved, we are focusing here on two pioneering fields: hydrodynamics and nonlinear optics. This tutorial aims to provide basic background and the recent developments on the formation of rogue waves in various systems in nonlinear optics, including laser physics and fiber optics. For this purpose we first discuss their formation in conservative systems, because most of the theoretical and analytical results have been realized in this context. By using a multiple space–time scale analysis, we review the derivation of the nonlinear Schrödinger equation from Maxwell's equations supplemented by constitutive equations for Kerr materials. This fundamental equation describes the evolution of a slowly varying envelope of dispersive waves. This approximation has been widely used in the majority of systems, including plasma physics, fluid mechanics, and nonlinear fiber optics. The basic property of this generic model that governs the dynamics of many conservative systems is its integrability. In particular, we concentrate on a nonlinear regime where classical prototypes of rogue wave solutions, such as Akhmediev breathers, Peregrine, and Ma solitons are discussed as well as their experimental evidence in optics and hydrodynamics. The second part focuses on the generation of rogue waves in one- and two-dimensional dissipative optical systems. Specifically, we consider Kerr-based resonators for which we present a detailed derivation of the Lugiato–Lefever equation, assuming that the resonator length is shorter than the space scales of diffraction (or the time scale of the dispersion) and the nonlinearity. In addition, the system possesses a large Fresnel number, i.e., a large aspect ratio so that the resonator boundary conditions do not alter the central part of the beam. Dissipative structures such as solitons and modulational instability and their relation to frequency comb generation are discussed. The formation of rogue waves and the control employing time-delayed feedback are presented for both Kerr and semiconductor-based devices. The last part presents future perspectives on rogue waves to three-dimensional dispersive and diffractive nonlinear resonators.

https://doi.org/10.1364/AOP.438025

Rogue waves in nonlinear optics

M. Tlidi and M. Taki

1. INTRODUCTION

Ever since the first confirmed field measurements of a freak wave in the North Sea at the Draupner platform on January 1, 1995, and reported in Refs. [1,2], extreme waves or rogue waves have been of great interest to both researchers and engineers [3–6]. The Draupner wave measured at a crest amplitude of 25.6 m on a sea state with a significant wave height (SWH) of 12 m, and one of the possible theories advanced by Haver [3] involved a self-focusing of energy of a wave group into one majestic wave event. They consist of large-amplitude pulses with a narrow width that appears with low probability. In contrast to typhoons, tsunamis, and storms that can be predicted hours in advance, rogue waves appear unpredictable. The long tail probability distribution is the fundamental characteristic which accounts for the generation of rogue waves. They appear unexpectedly on the ocean's surface which renders them extremely dangerous even for huge ships, marine structures or submarines. They have also been observed in both deep and shallow waters, and also in deep internal layers of the ocean [3–5].

Rogue waves appear not only in the ocean but also in optical fibers [7]. Indeed in 2007, Solli and collaborators observed extraordinary soliton-like pulses with extremely large intensity using fiber in a supercontinuum (SC) generation regime. More importantly, they established an intriguing link between rogue waves in oceans and optical waves along with fiber. In nonlinear optics and laser physics, coherent structures are generated as extreme events from the propagation of laser beams. In particular, the possibility of engineering the parameters of an optical fiber such as nonlinearity and dispersion renders such systems of particular importance for frequency comb generation, which has potential applications in spectroscopy. In addition, the intensity and the phase of the input light may be tailored with advanced data-processing techniques leading to real-time spectrum measurements such as a dispersive Fourier transformation and time-lens techniques. These powerful real-time measurement techniques allow the speed limitations of traditional optical or electronic measurements to be overcome.

A particular experimental originality of the work of Solli and collaborators is in the use of a time-stretch dispersive Fourier transform to map spectral fluctuations into temporal fluctuations in real time. The dispersive Fourier transformation consists of mapping the frequency spectrum onto the temporal waveform [8,9]. Such time-lensing techniques allow for the measurement of ultrashort pulses with sub-picosecond resolution. This method has been applied to observe rogue waves such as Raman rogue waves [10], soliton explosions in lasers and the generation of rogue waves [11], SC generation [12], and Kerr-lens mode-locked [13] and fiber lasers [10,14,15]. On the other hand, the time-lens technique allows one to measure the intensities of localized peaks with a resolution of the order of picoseconds [9]. This comes from temporal imaging systems which are analogous to spatial imaging systems as the time-lens technique allows one to compress or expand the pulse width of optical waveforms without distortion. It has been applied to investigate optical rogue wave (ORW) formation in relation to integrable turbulence [16], and the spontaneous formation of breathers and rogue waves in optical fiber modulational instability (MI) [17]. The combination of dispersive Fourier transformation with a time-lens technique may lead to considerable advances in real-time measurement of ultrafast soliton dynamics. The dispersive Fourier transformation

theory and its applications in physics and photonics is beyond the scope of this contribution, and the interested reader may refer to the review papers [18–21].

Since the seminal paper by Solli *et al.* [7], rogue waves appear in various nonlinear systems such as mode-locked lasers [11,22], cavity semiconductors [23–26], plasma waves [27,28], chemical reaction–diffusion systems [29–31], quantum optics, and even in finance [32,33]. An example of such behavior is shown in Fig. 1 taken in part from Refs. [7,34]. These extreme waves constitute an interdisciplinary issue and considerable progress has been made toward the understanding of their formation, stability, and interaction, though an important number of questions remain open, such as the effect of noisy sources on their formation or their role in turbulent regimes. In particular, optical systems and lasers display such events which arise due to self-focusing nonlinearities, inducing multi-transverse modes and filamentation, which deteriorates the beam quality. The first experimental evidence of rogue waves in fiber optics [7] has triggered several groups to investigate this intriguing phenomenon. The explosive growth of this field of research, can be witnessed by overviews [31,35–44]. Compared with oceanography, there remains a lot to be learned on the mechanisms leading to the formation of rogue waves in optical systems. Access to experimental data is important to better understand the underlying physics. Most systems exhibiting rogue waves, struggle against experimental characterization because of their size or time scales. In this respect, optical and photonics systems constitute an excellent platform for researchers as they are classic examples of dissipative systems which exhibit extreme events that can be experimentally investigated in a reliable way. In particular, high-sensitivity experimental techniques have emerged very recently and can be adapted to ultra-fast-pulse measurements [45,46].

Most of the analytical understanding of rogue waves in conservative systems has been realized in the framework of the nonlinear Schrödinger equation (NLSE). The latter serves as a basic model for the analytical understanding of the formation of rogue waves in conservative systems. More precisely, the link between rogue waves and the rational solutions of the NLSE has been established in the seminal paper by Akmediev and collaborators [47]. It is generally admitted that the origin of rogue waves is related to breather-type solutions of the NLSE [48–50]. Several mechanisms have been suggested to be at the origin of the formation of rogue waves in the literature. In most cases, the MI mechanism together with pulse collisions is considered to be the main mechanism that generates rogue waves as shown by Peregrine [51] and by Akhmediev *et al.* [47]. Experimental confirmation of Peregrine solitons and rogue waves as a result of pulses collision have been demonstrated in optical fibers [52,53] and in water wave tanks [54–56]. In these systems, small-amplitude pulses may grow to large-amplitude pulses provided that their frequencies belong to a band of unstable modes with a positive gain. Nonlinear interaction between these frequencies can lead to complex wave dynamics. For instance, the case of the two frequency solutions of the NLSE in the form of Akhmediev breathers has been analytically studied in Ref. [57] and collisions of Akhmediev breathers have been experimentally evidenced in an optical fiber system [58].

However, in dissipative systems, the NLSE fails to capture the dynamics because it ignores pumping and dissipation. Moreover, in spatially extended systems, when the dimensionality is higher than one, bounded solutions are not admitted by the NLSE due to beam collapse rendering the formation of rogue waves impossible [59]. To circumvent this problem, several physical mechanisms have been proposed in the literature, which perfectly describe the nonlinear dynamics encountered, for example, optical resonators. Indeed, the mean-field approach described by the Lugiato–Lefever type of models for optical cavities have been of significant interest [60] as they take

Figure 1

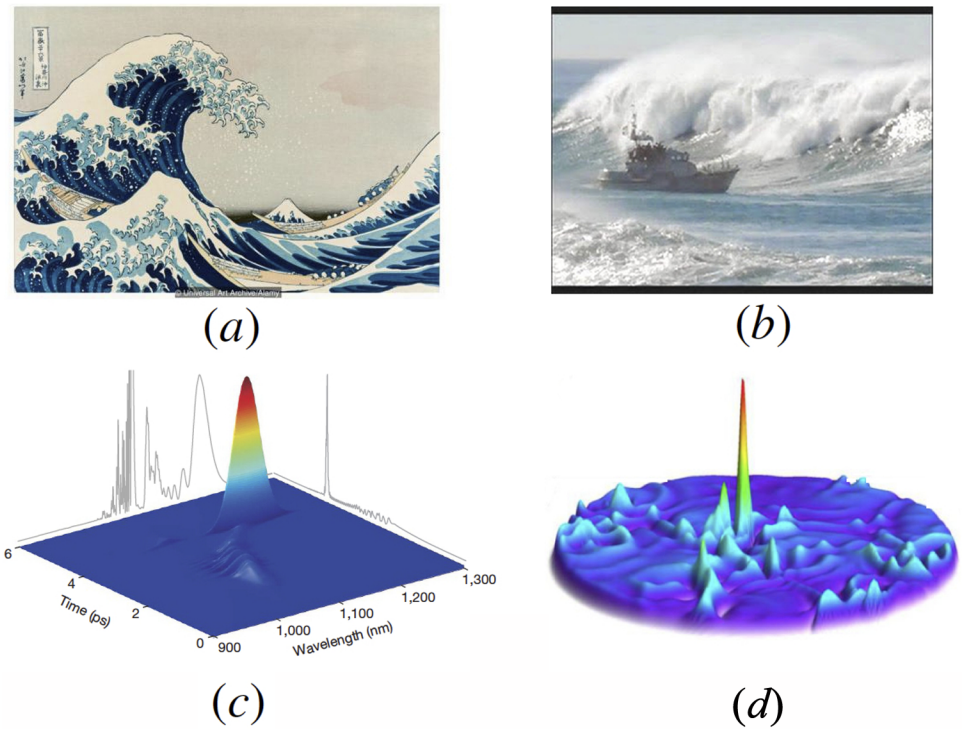

Rogue waves: (a) Japanese artist Katsushika Hokusai's painting, known as "The Great Wave off Kanagawa"; (b) a rough ocean surface with waves towering over a ship; (c) one-dimensional fiber optics; and (d) two-dimensional broad-area lasers. (c) Reprinted by permission from Macmillan Publishers Ltd: Solli *et al.*, Nature, **450**, 1054–1057 (2007) [7]. Copyright 2007. (d) Figure 5(b) reprinted with permission from Gibson *et al.*, Phys. Rev. Lett., **116**, 043903 (2016) [34]. Copyright 2016 by the American Physical Society.

into account, in addition to the nonlinearity, dispersion and/or diffraction, and they also explicitly include pumping and dissipation. The Lugiato–Lefever equation (LLE) has been shown to support the formation of robust stable localized structures (LSs) in one-dimensional (1D), two-dimensional (2D) [61], and in 3D systems [62]. These LSs, often called dissipative solitons or cavity solitons, are one of the most frequently studied nonlinear objects.

In 1D Kerr resonators, temporal [63] and spatial [64] LSs have been observed experimentally. In these systems, the spectral contents of the LSs are the optical frequency combs, referred to as Kerr combs. The link between the formation of temporal LSs and frequency combs have been established in Ref. [65] (see an excellent review by Lugiato *et al.* [66] in the theme issue [67,68]). This phenomenon has attracted a lot of interest because it has applications in the generation of ultra-stable light wave and microwave signals which find direct applications in optical communication networks, microwave photonic systems, and in aerospace engineering [69,70]. This is mainly due to the development of laser-based precision spectroscopy including the optical frequency comb technique [71]. Driven optical microcavities have been widely used for the generation of optical frequency combs which can be modeled by the LLE with unprecedented precision. In optical resonators subject to a high intensity of the injected field, temporal LSs may exhibit complex behavior. Statistical analyses have indicated that this phenomenon belongs to the category of extreme events or rogue waves [23].

In 2D dissipative broad-area devices, rogue waves have been predicted using the mean-field approach and experimentally observed as well [25,26,34,72–75]. In addition to 2D LSs predicted in Kerr resonators, another interesting system is presented, namely, semiconductor cavities. Thanks to the mature semiconductor laser technology and the possibility for application of 2D localized pulses, they have attracted significant interest in all-optical control of light, optical storage, and information processing. In particular, vertical-cavity surface-emitting lasers (VCSELs) were first realized in Ref. [76]. Light confinement has been investigated in VCSELs for which we refer the reader to these recent reviews [77–79]. Rogue waves have been experimentally observed in 1D setting for VCSELs [24]. In 2D settings, rogue waves have been numerically demonstrated in dissipative systems by pumping [25] or by optical feedback [26] in broad-area surface-emitting laser with a saturable absorber (SA). They have been also observed using photorefractive materials [80,81].

The present contribution aims to shed some light for a better understanding of the mechanisms underlying the formation of rogue waves in optics and photonics, along with an analogy in hydrodynamics when possible. After an introduction, we present the advances in conservative systems in the first part, such as fiber optics. Following this, we turn our attention to dissipative systems such as optical Kerr and semiconductor cavities, in which we discuss how to control 1D and 2D rogue waves by injection or via delayed feedback. In addition to presenting the state of the art, recent progress, new ideas, and novel techniques, we also present experimental evidence of temporal and spatial rogue waves in advanced conservative and dissipative optical systems. Rogue waves in the above-mentioned dissipative systems are discussed in the second part of this article, including experimental evidence of temporal rogue waves in all fiber cavities, and spatial ones in broad-area lasers such as VCSELs.

2. ANALYTICAL TREATMENT OF ROGUE WAVES IN NONLINEAR DISPERSIVE MEDIA

One of the famous equations that describes many physical problems in dispersive media is the NLSE. This equation has become famous because it provides, in its linear form, a basic description of a wave function in quantum mechanics. Nevertheless, its main characteristic is the generic description of the evolution (propagation) of the slowly varying envelope of dispersive waves; approximation widely used in the majority of physical systems including quantum mechanical ones.

In this section, we are mainly interested in the two fields of optics and hydrodynamics where, for more than a decade, a sustained research activity on the formation and dynamics of ORWs have played an important role thanks to innovative developments in theory and experience. Although hydrodynamics (surface waves) and optics (optical fiber systems) correspond to different fields with regards to the physics of the underlying the observed phenomena, it is possible, in the leading slowly varying envelope approximation, to model the wave propagation in both media by NLSE. A decisive issue in this regard is the considerable progress made by Solli *et al.* [7] by observing an optical counterpart of oceanic rogue waves in a photonic crystal fiber, producing a phenomenon named the ORW owing to its similarity to the oceanic rogue wave. The authors of Refs. [7,82,83] have shown that the ORWs appear as solutions of the generalized nonlinear Schödinger equation (GNLSE), which is often used to describe the nonlinear dynamics of water waves as well as light propagation in photonic crystal fibers.

Here we focus on the derivation of the NLSE problem because it is much more generic than its solutions. We use a multiple time and space scales analysis and assume that the envelope of the wave packet that propagates in Kerr media is a slowly varying

function of time and space. We begin by discussing the linear regime and the role of MI. However, in the nonlinear regime, analytic results for the NLSE require strenuous efforts, difficult and tiring and far beyond the scope of this tutorial. Different analytical approaches from the literature for solving the NLSE can be found in the book by Akhmediev and Ankiewicz [84]. In this context, we present the exact analytical solutions admitted by all the "rogue wave communities" as the most important prototypes of rogue waves, in both optics and hydrodynamics. Following this, we provide analogies between optics and hydrodynamics quantitatively.

2.1. The NLSE

In this subsection, we review the derivation of the NLSE. This equation describes how a pulse with a slowly varying envelope propagates in a Kerr medium. To simplify the analysis, we focus on a medium devoid of magnetization, current density, and charge density. When an intense optical field propagates in a Kerr medium, it is likely to modify the properties of this medium, for instance by distorting the electron balance of its electron clouds. The susceptibility of the material then becomes dependent on the field. Therefore, the response of the medium to an electrical excitation is no longer linear, and the polarization has an additional nonlinear contribution. The classical formalism expresses the vector polarization as $\mathbf{P} = \mathbf{P}^l + \mathbf{P}^{nl}$ where $\mathbf{P}^l$ and $\mathbf{P}^{nl}$ denote the linear and the third-order nonlinear polarizations, respectively. We assume that the second-order nonlinear polarization is absent because the Kerr media possesses an inversion symmetry. This means that the Kerr material is cubic and centrosymmetric. This property allows both anisotropy and second-order nonlinearities to be avoided. This nonlinear response leads to frequency upconversion or downconversion such as second-harmonic generation or optical parametric oscillators, both are noncentrosymmetric media. From the macroscopic Maxwell equations together with the above-mentioned approximations, the pulse propagation equation reads

$$\mathcal{L}\mathbf{E}(\mathbf{r},t) = \nabla^2\mathbf{E} - \nabla(\nabla\cdot\mathbf{E}) - \frac{1}{c^2}\partial_t^2(\mathbf{E}+\mathbf{P}^l) = \mu\partial_t^2\mathbf{P}^{nl}, \tag{1}$$

with $\mathcal{L}$ is an integrodifferential operator acting on the electric field $\mathbf{E}$. In general, the response of the medium to an electrical excitation is not necessarily instantaneous. As a consequence, the polarization does not only depend on the electric field value at the current moment but also on its values at some time in the past. In this case, the two contributions to the vector polarization read

$$\mathbf{P}^l = \int_{-\infty}^{t} \chi^{(1)}(t-t_1)\mathbf{E}(\mathbf{r},t_1)\,dt_1, \tag{2}$$

$$\mathbf{P}^{nl} = \int_{-\infty}^{t} \chi^{(3)}(t-t_1,t-t_2,t-t_3)\mathbf{E}(\mathbf{r},t_1)\mathbf{E}(\mathbf{r},t_2)\mathbf{E}(\mathbf{r},t_3)\,dt_1\,dt_2\,dt_3. \tag{3}$$

Second-order susceptibility $\chi^{(2)}$ vanishes for a Kerr medium such as silica glass owing to its inversion symmetry. Therefore, the lowest-order nonlinear effects in Kerr media originate from the third-order susceptibility $\chi^{(3)}$. This section aims to present the derivation of the NLSE. The analysis presented is classical in the field of nonlinear optics [85]. Our objective is to determine a slow time and slow space of the propagation equation (1) through a perturbation expansion in powers of a small parameter ζ. This analysis rests on the fact that the third-order polarization is a small correction to the linear equation. This approximation is justified because $\chi^{(3)}$ is small. This applies that the right-hand side of the propagation equation (1) is of order ζ^2. We next expand the electric field in a power series of ζ as

$$\mathbf{E} = \mathbf{E}_0 + \zeta\mathbf{E}_1 + \zeta^2\mathbf{E}_2 + \cdots. \tag{4}$$

The unperturbed wave packet $\mathbf{E}_0$ is assumed to be linearly polarized in a plane orthogonal to the propagation direction

$$\mathbf{E}_0(\mathbf{r},t) = \mathbf{e}A(\mathbf{r},t)\exp\left[i(kz-\omega t)\right] + c.c., \tag{5}$$

where $c.c.$ denotes the complex conjugate and $\mathbf{e}$ is a unitary vector in the transverse plane (x,y). The envelope of the field $A = A(\mathbf{r},t)$ varies slowly in the z direction and in time t. The optical frequency ω and the wavenumber k are related by the dispersion relation $\omega = vk$ with v the effective velocity of light in the Kerr medium. Multiple space–time scale analysis requires the definition of slow coordinates $(X,Y,T) = (\zeta x, \zeta y, \zeta t)$, $Z_1 = \zeta z$, and $Z_2 = \zeta^2 z$. The derivatives of the slowly varying envelope with respect to these slow coordinates are

$$\partial_{x,y,t}A = \zeta\partial_{X,Y,T}A \quad \text{and} \quad \partial_Z A = \zeta\partial_{Z_1}A + \zeta^2\partial_{Z_2}A. \tag{6}$$

Finally, we expand the integrodifferential operator $\mathcal{L}$ defined by Eq. (1) as

$$\mathcal{L} = \mathcal{L}_0 + \zeta\mathcal{L}_1 + \zeta^2\mathcal{L}_2 + \cdots. \tag{7}$$

By replacing this expansion, and inserting Eqs. (4) and (7) into the propagation equation (1), we obtain

$$\left(\mathcal{L}_0 + \zeta\mathcal{L}_1 + \zeta^2\mathcal{L}_2\right)\left(\mathbf{E}_0 + \zeta\mathbf{E}_1 + \zeta^2\mathbf{E}_2\right) = \mu\partial_t^2\mathbf{P}^{nl}. \tag{8}$$

Equating the coefficients of equal orders in ζ, we obtain a sequence of equations

$$\mathcal{L}_0\mathbf{E}_0 = \mathbf{0}, \tag{9}$$

$$\mathcal{L}_0\mathbf{E}_1 = -\mathcal{L}_1\mathbf{E}_0, \tag{10}$$

$$\mathcal{L}_0\mathbf{E}_2 = -\mathcal{L}_2\mathbf{E}_0 - \mathcal{L}_1\mathbf{E}_1 + \mu\partial_t^2\mathbf{P}^{nl}. \tag{11}$$

2.1a. Order ζ^0

By replacing the unperturbed wave packet $\mathbf{E}_0$ in Eq. (9), we obtain

$$\mathcal{L}_0\mathbf{E}_0 = \left[-k^2 + k^2(\omega)\right]\mathbf{E}_0 = \mathbf{0}. \tag{12}$$

This relation is satisfied only if $k = \pm k(\omega)$. The wavenumber k of the wave packet obeys the linear dispersion relation $k = \pm\omega n(\omega)/c$. This means that the solution (5) is indeed a solution to the trivial problem (9). At this order, the amplitude A remains undetermined. This is because the amplitude $A = A(X,Y,Z_1,Z_2,T)$ depends on the slow time–space scale T,X,Y,Z_1,Z_2, which does not appear explicitly in the trivial problem (9). We now proceed to higher order in the perturbation expansion orders ζ^1 and ζ^2.

2.1b. Order ζ^1

Equation (10) can be rewritten as

$$\mathcal{L}_1\mathbf{E}_0 = 2i\mathbf{e}k\exp\left[i(kz-\omega t)\right]\left(\partial_{Z_1} + k'\partial_T\right)A + c.c. \tag{13}$$

The vector $\mathcal{L}_0\mathbf{E}_1$ lies in the transverse plane perpendicular to the optical axis. The solution at this order satisfies

$$\left(\partial_{Z_1} + k'\partial_T\right)A = 0. \tag{14}$$

2.1c. Order ζ^2

The nonlinear polarization contribution appears only at this order

$$\mathbf{P}^{nl} = \epsilon\mathbf{e}\exp\left[i(kz-\omega t)\right]\left(3\chi^{(3,1)}|A|^2 + \chi^{(3,3)}A^2\exp\left[2i(kz-\omega t)\right]\right)A + c.c., \tag{15}$$

where the Fourier transforms of the third-order susceptibility are $\chi^{(3,1)} = \chi(\omega,\omega,-\omega) = \chi(\omega,-\omega,\omega) = \chi(\omega,\omega,-\omega)$ and $\chi^{(3,3)} = \chi(\omega,\omega,\omega)$. By substituting Eq. (15) into Eq. (11), and after some calculations, we obtain

$$\mathcal{L}_2\mathbf{E}_0 = \mathbf{e}\exp\left[i(kz-\omega t)\right]\left(\partial_X^2+\partial_Y^2+2ik\partial_{Z_2}-kk''\partial_T^2\right)A + c.c.. \tag{16}$$

In many applications the field is considered linearly polarized along some fixed direction. Indeed the variable E is the component of the electric field polarized along the x direction. Taking into account Eqs. (14)–(16), Eq. (11) becomes

$$\begin{aligned}\mathcal{L}_0\mathbf{E}_2 = \quad -\mathbf{e}\exp\left[i(kz-\omega t)\right]&\left(\partial_X^2+\partial_Y^2+2ik\partial_{Z_2}-k\beta_2\partial_T^2+\frac{3\omega^2}{c^2}\chi^{(3,1)}|A|^2\right)A\\ &-\frac{9\omega^2}{c^2}\chi^{(3,3)}A^3\exp\left[3i(kz-\omega t)\right]+c.c..\end{aligned} \tag{17}$$

In addition, we limit our description to a weak dispersive medium where the last term of this equation can be neglected. The solution of the inhomogeneous problem (17) at order ζ^2 yields

$$\partial_{Z_2}A = \frac{i}{2k}\left(\partial_X^2+\partial_Y^2\right)A - \frac{i\beta_2}{2}\partial_T^2A - \left(\partial_{Z_1}+k'\partial_T\right)A + \frac{3ik}{2}\chi^{(3,1)}|A|^2A. \tag{18}$$

The first term of the right-hand side of this equation accounts for diffraction, the second term is group velocity dispersion where $k'' = \beta_2$ is the second-order dispersion, and $k' = 1/v_g$ is the inverse of the group velocity v_g of the wave packet. The last term describes material nonlinearity.

2.1d. The NLSE

By multiplying Eq. (14) by ζ, and Eq. (18) by ζ^2, then the sum of these two equations together with the use of the relation (6) yields

$$\partial_z E = \frac{i}{2k}\left(\partial_x^2+\partial_y^2\right)E - \frac{i\beta_2}{2}\partial_t^2E - k'\partial_tE + \frac{ikn_2}{n}\chi^{(3,1)}|E|^2E, \tag{19}$$

where $E = \zeta A + \cdots$. The nonlinear refractive index n_2 is linked to the third-order susceptibility by the relation $n_2 = 3n\chi^{(3,1)}/2$ where n is the linear refractive index.

By using the Leibniz transformation (retarded time)

$$\tau = t - k'z,$$

Eq. (19) reads

$$\partial_z E = \frac{ik}{2}\nabla_\perp^2E - \frac{i\beta_2}{2}\partial_\tau^2 + i\gamma|E|^2E. \tag{20}$$

Here $\nabla_\perp^2 = \partial_{xx}+\partial_{yy}$ is the Laplace operator acting on the transverse plane (x,y) and the nonlinear coefficient $\gamma = kn_2/n$. The complex order parameter $E = E(x,y,\tau,t)$ describes the propagation along the fiber axis (z) of the slowly varying wave envelope in 3D configuration (transverse plane coordinates (x, y) and chromatic dispersion (τ coordinate)). Note that the NLSE admits solutions only in a 1D setting due to beam collapse [59]; namely, solutions in the form of bright and dark solitons, the propagation of which has been experimentally observed in fiber optics [86,87].

With the following change of variables and parameters: $(x,y)\to(x,y)/\sqrt{k}$, $\tau\to\tau/\sqrt{|\beta_2|}$, $E = (n/kn_2)^{1/2}F$, Eq. (20) yields the dimensionless NLSE

$$\partial_z F = \frac{i}{2}(\nabla_\perp^2 \pm \partial_\tau^2)F + i|F|^2F. \tag{21}$$

The NLSE is a dynamical system that describes how the envelope of the pulse propagates in a Kerr medium. It has been proved that NLSE is exactly integrable and their most important solutions can be found analytically.

2.2. Linear Regime: MI for Initiating Rogue Waves Formation

We restrict ourselves to a strictly 1D setting, by neglecting the diffraction phenomena when using a guided waves structure in the plane (x, y). Nonlinear systems are well known to manifest a large spectrum of dynamical behavior ranging from regular to chaotic regimes. Both regimes exhibit complex spatiotemporal solutions that have been subject to intensive research [88–90]. The key physical phenomenon characteristic of nonlinear systems is instability, which is one of the main and important aspects that encompasses all domains of nonlinear science. It is out of the scope of this tutorial to report on all types of instabilities appearing in nonlinear systems. However, among the different types of instabilities, MI, is one of the most famous because it naturally appears in diverse physical areas, including hydrodynamics, plasma physics, and optics among others. The first studies of MI date back to the early 1960s in such different fields as hydrodynamics [91], nonlinear optics [92], and plasma physics [93]. MI originates from the perturbation of an intense continuous or quasi-continuous field by a weak signal that is then amplified exponentially [91]. In this linear stage of evolution, amplification of modes leads to an increase in the amplitude (or intensity) followed by the nonlinear regime where the system experiences the Kerr effect that becomes dominant. Different bifurcations (or every scenario) arise from this dynamics, which constitutes the origin of the fascinating regularity and complexity behaviors and related states observed in almost all nonlinear systems, irrespective of the domain of nonlinear science. These states may range from solitons (the most well-known regular nonlinear solution) to highly developed turbulence. Of course, consecutive sequences of bifurcations allow transitions between an impressive number of solutions and their dynamical complexity. Fortunately, strong mathematical methods and tools exist to help find analytically some (important) solutions, though this depends on the nonlinear system at hand. Indeed, Hamiltonian systems (or conservative nonlinear systems) are, in general, more tractable analytically than dissipative systems where there is, intrinsically (because of dissipation), a lack of conservative quantities such as energy. Still, in these systems, perturbative methods are highly useful to obtain many relevant results. In general, for strongly nonlinear dissipative systems, mathematics often finds its limit (except in special cases), but the advent of efficient and powerful computers provides a precious approach to deeply understand highly complex dynamics such as spatiotemporal chaos.

Let us return to the process of MI we are interested in. It is present in many fields of physics and has been studied extensively in optical fibers because it provides a convenient and valuable way for experimental generation and observation of a train of ultrashort pulses. Before going further in the analysis, it is worthwhile to recall linear stability analysis in the ubiquitous case of free light propagation in nonlinear optical fiber systems. Light propagation in a mono-mode nonlinear optical fiber is well described by the NLSE for the slowly varying complex amplitude $E(z, \tau)$ of the electric field as shown in the Sec. 2.1 (see Eq. (20)). Let us rewrite the NLSE in the following 1D form $\partial_z E = -i\frac{1}{2}\partial_t^2 F + i|E|^2 E$, where the complex function $E = E(z, t)$ describes the time evolution of slowly varying wave envelope along the propagation direction. This equation has the following nonlinear stationary (i.e., τ-independent) solution:

$$E_{st}(z) = E_0 \exp(i\gamma P_0 z), \tag{22}$$

where $P_0 = |E_0|^2$ is the continuous-wave (CW) intensity at the entrance of the fiber. We now perform a linearization of Eq. (20) around the nonlinear stationary solution $E_{st}(z)$ with respect to a small perturbation $a(z, \tau)$ such that $|a(z, \tau)| \ll |E_0|$. Namely, we look for a solution of Eq. (20) in the form

$$E(z, \tau) = [E_0 + a(z, \tau)] \exp(i\gamma P_0 z). \tag{23}$$

Substituting Eq. (23) into Eq. (20) with $\nabla_\perp^2 = 0$ and keeping only linear terms in $a(z,\tau)$ and $a^*(z,\tau)$, we obtain the following linearized equation:

$$\partial_z a = -i\frac{\beta_2}{2}\partial_\tau^2 a + i\gamma P_0(a + a^*), \tag{24}$$

where a^* stands for the complex conjugate of a. The linearized equation (24) can be solved for perturbations in the form of $a(z,\tau) = \exp[i(Kz - \Omega\tau)]$ where K and Ω are the wavenumber and the frequency of the perturbation, respectively. Non-trivial solutions $a(z,\tau)$ exist only when K and Ω satisfy the following dispersion relation:

$$K = \pm\frac{1}{2}|\beta_2\Omega|\sqrt{\Omega^2 + s\frac{4P_0\gamma}{|\beta_2|}}, \tag{25}$$

where we have set $s = \pm 1$ depending on the sign of β_2. For normal (anomalous) dispersion $\beta_2 > 0$ ($\beta_2 < 0$) and $s = 1$ ($s = -1$).

The dispersion relation (25) shows an important feature, namely, the instability critically depends on the sign of β_2. When $\beta_2 > 0$ ($s = 1$), the term under the square root is positive and the wavenumber K is real for all Ω, meaning that the nonlinear stationary solution is stable in the regime of normal dispersion. However, the same nonlinear stationary solution is inherently unstable to plane wave perturbations in the anomalous regime ($\beta_2 < 0$) because the wavenumber K becomes a complex number with a non-vanishing imaginary part giving rise to an exponential growth of the perturbation as can be seen from Eq. (25). Indeed the term under the square root can be negative for a band of frequencies that can be calculated from the dispersion relation (25) by determining all frequencies Ω with $\Im(K)[\Omega] > 0$. The frequencies of marginal (or neutral) stable modes, often called critical modes, are defined as Ω_c where $\Im(K)[\Omega_c] = 0$, which gives

$$\Omega_c = \pm\sqrt{\frac{4P_0\gamma}{|\beta_2|}}. \tag{26}$$

These modes are called marginal (neutral) because they are neither amplified nor attenuated and define the limits of the frequency instability range.

The gain spectrum of MI is obtained from the dispersion relation (25) by setting $s = -1$, and the gain

$$g(\Omega) = 2\Im(K) = |\beta_2\Omega|\sqrt{\Omega_c^2 - \Omega^2}, \tag{27}$$

where factor 2 is introduced for a power gain and we have set Ω_c to its expression defined in (26). The gain is displayed in Fig. 2(a) in the plane (Ω, g), for three increasing values of the input power P_0. The two instability lobes appearing in Fig. 2(a) stem from the parity symmetry of the gain on the frequency and correspond to the spectral sidebands generated by the instability, which are easily accessible to the experiments. The gain exists only in the range $[-\Omega_c, +\Omega_c]$ and reaches its maximum g_{Max} at

$$\Omega_{Max} = \pm\sqrt{\frac{2\gamma P_0}{|\beta_2|}} = \pm\frac{\Omega_c}{\sqrt{2}}, \tag{28}$$

where the maximum gain value is

$$g_{Max} = g(\Omega_{Max}) = \frac{1}{2}|\beta_2|\Omega_c^2 = 2\gamma P_0. \tag{29}$$

Note that, as can be expected, the frequency instability domains (the two lobes) increase in size and height with increasing input power. A numerical check of the linear stability

Figure 2

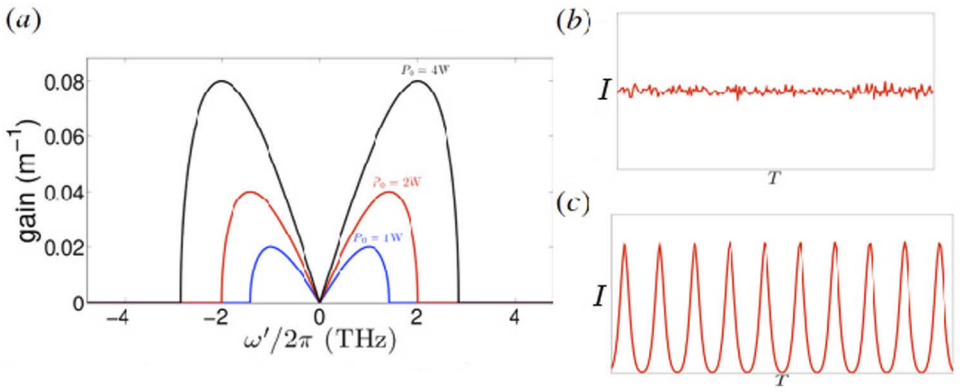

Numerical simulations: (a) spectrum gain (27), for three values of injected power, showing the sidebands MI; (b) temporal intensity injected as initial condition composed of continuous waves with a noisy source; (c) a pulse train resulting from the spontaneous amplitude modulations induced by MI.

Figure 3

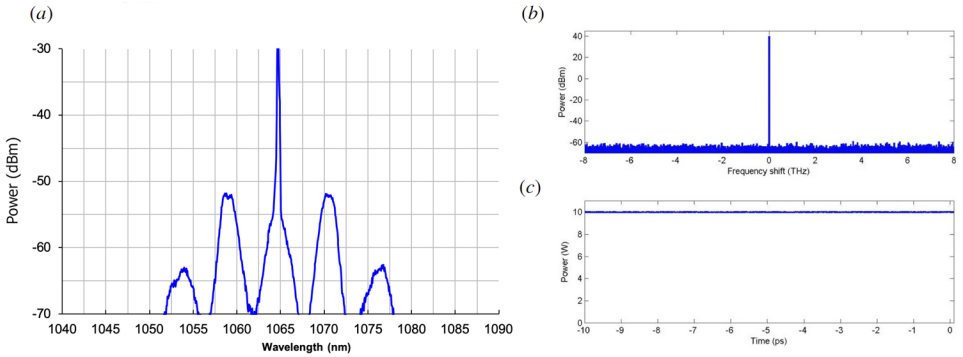

(a) Experimental frequency spectrum showing the sidebands instabilities. (b) Monochromatic CW plane wave injected at the entrance of the nonlinear optical fiber. (c) Corresponding constant amplitude CW plane wave.

analysis is depicted in Fig. 2(b) and 2(c) where we have initialized the propagation in the fiber by injecting an external CW surrounded with a noisy source [Fig. 2(b)]. The constant amplitude of the CW initial condition experiences the instability by showing modulations at the maximum frequency Ω_{Max} in its amplitude at the early stage of the linear instability. It is these spontaneous temporal modulations in the amplitude of the CW operation that justify the term of MI. As the electric field propagates in the fiber, the nonlinear terms (Kerr effect) are excited and become dominant transforming the modulations in the CW into a pulse train as can be seen in Fig. 2(c). The experimental signature of MI is shown in the spectrum displayed in Fig. 3, where two symmetric frequency sidebands are generated by MI [Fig. 3(a)] when the optical nonlinear fiber is injected with a CW as plotted in Fig. 3(b) and 3(c).

More generally, the process of MI is present in many fields of physics and has been studied extensively in optical fibers because it provides a convenient and precious way for experimental generation and observation of a train of ultrashort pulses. In optics, the first experimental observation of MI was reported in Refs. [94,95] where an intense quasicontinuous field injected in optical fiber was converted into a train of ultrashort

pulses [96] or fiber optical parametric amplifiers (FOPAs) [97,98]. This groundbreaking experiment gave rise to the rapid development of parametric amplification and ultrashort pulse generation that have become some of the most important branches of research in nonlinear fiber optics. In hydrodynamics, MI was shown to be one of the fundamental mechanisms responsible for the formation of the so-called rogue waves [99]. Very recently, optical equivalents of the oceanic rogue waves have been discovered in optical fibers [7] and are called ORWs. In this context, the GNLSE was shown to be successful in describing the formation of rogue waves both in the ocean and in fibers.

Nowadays, even after many years, the study of MI in hydrodynamics and optics remains an attractive research activity. For instance, in optics, MI is the key ingredient for the understanding of SC generation [100] and ORW formation [7,52,101]: both physically originate from MI. From a fundamental point of view, MI results from the balance between nonlinear and linear effects experienced by a field during the propagation in dispersive nonlinear media. In the most usual case in optics, the linear phase mismatch depends only on the group-velocity dispersion of the optical fiber [94,95,97,98]. The contribution of other linear terms, such as the group-velocity difference between polarization modes [102] or transverse ones [103], must be accounted for in birefringent or multimode fibers, respectively. In the anomalous dispersion regime, the broadest frequency shifts are obtained by pumping the fiber as close as possible to the zero-dispersion wavelength as in FOPAs, or in the context of SC/rogue wave generation for instance [7]. As a consequence, even higher-order dispersion terms must be included in the linear phase-mismatch relation [104,105]. This explains the MI observed in the normal dispersion region of an optical fiber [103,104]. In all these studies, the theoretical background is based on the standard linear stability analysis, which shows that the gain curve only depends on even-dispersion terms. This has been experimentally confirmed in the context of FOPAs, for instance, in which excellent agreement between theory and experiment is achieved when a CW seeds the process [98].

Many authors have reported the important impact of higher-order dispersive terms in the GNLSE on the main characteristics of rogue waves [99,106,107] and also on their non-Gaussian statistics [52]. In particular, it was demonstrated that the third-order dispersion is already sufficient to explain the ORW formation and, most importantly, their probability density function [101]. A striking feature when dealing with purely NLSE remains in the transition from linear to nonlinear regimes that can be accounted for in an elegant and instructive way by invoking MI. For instance, Akhmediev Breather which is one of the main prototypes of rogue waves can be obtained as a nonlinear stage of unstable linear plane waves.

2.3. Nonlinear Regime: Akhmediev Breather, Peregrine Soliton, and Bright Soliton As Prototypes of Rogue Waves

Let us consider the dimensionless NLSE (21) in a 1D system where diffraction is neglected by setting $\nabla_\perp^2 = 0$, and we assume that the sign of the second derivative with respect to the retarded time τ is negative (anomalous dispersion regime). The NLSE is a dynamical system with an infinite number of degrees of freedom and corresponds to an infinite-dimensional Hamiltonian system. As it is an integrable system, it has an infinite number of conserved quantities. The lowest-order integrals are the energy (or the number of particles)

$$Q = \int_{-\infty}^{+\infty} |F|^2 \, d\tau, \tag{30}$$

the momentum

$$M = i \int_{-\infty}^{+\infty} (F_\tau F^* - F_\tau^* F) \, d\tau, \tag{31}$$

and the Hamiltonian

$$H = \frac{1}{2}\int_{-\infty}^{+\infty} (|F_\tau|^2 - |F_\tau|^4)\, d\tau. \tag{32}$$

The seminal work [108] discusses the first few of the higher-order conserved quantities. The NLSE can be written in terms of the Hamiltonian as

$$\frac{\partial F}{\partial \tau} = i\frac{\delta H}{\delta F^*}, \tag{33}$$

where the right-hand side denotes a functional derivative.

It is far beyond the scope of this contribution to present the analytical derivation of nonlinear solutions of the NLSE (21). This is because mathematics is not simple to handle (see the mathematical aspects of optical solitons [109–111]). In particular, let us mention the inverse scattering method that constitutes a powerful tool in the soliton theory which has been applied to the Korteweg–de Vries equation, a nonlinear partial differential equation that appears in hydrodynamics. However, its applicability to the NLSE is an arduous mathematical problem. In this section, we only use the results obtained by the analytical derivation of nonlinear solutions of the NLSE (21) presented by Akhmediev and Ankiewicz [84]. In this book, a method leading to the derivation of solutions associated with not only soliton but also periodic solutions, and higher-order solitons is described. The 1D solutions of the NLSE reads [84]

$$F(\tau, t) = \left(1 + \frac{2(1-2a)\cosh(bt) + ib\sinh(bt)}{\sqrt{2a}\cos(2\sqrt{1-2a}\tau) - \cosh(bt)}\right)\exp(it) \tag{34}$$

with $b = 2[2a(1-2a)]^{1/2}$. For a more detailed discussion see the excellent book [84]. Figure 4 shows three examples of well-known fundamental solutions of the NLSE, which are the Akhmediev breather, Peregrine soliton, and Kuznetsov–Ma soliton. These are the exact solutions of the NLSE. They are of great importance as analytical solutions corresponding to simple prototypes of rogue waves observed in nature. They are localized in space and periodic in time (Akhmediev breather), localized in time and periodic in space [Kuznetsov–Ma (KM) soliton], and localized in both time and space (Peregrine soliton). In addition to these properties of localization, they are set on a finite background contrarily to fundamental solitons that are set on a zero background. More importantly, because almost all-optical devices (optical cavities and fiber systems) are subject to pumping fields in the form of quasi-plane waves, these solutions become unavoidable and popular because they approach naturally, in the linear limit, the unstable plane waves. Their formation, dynamics, and collisions are ubiquitous in the nonlinear regime of these systems, including spatiotemporal chaos and turbulent regimes. More precisely, in these systems, the MI governs the growth of periodic perturbations on CW background. In particular, in optics, MI arises from noise seeded in the laser pumps, which governs the growth and decay of perturbations giving rise to LSs. Possible noise sources include quantum noise, amplified spontaneous emission, or indeed could be technical laser noise. Some of these solutions (or their approximations) have been compared with structures in hydrodynamics, and the phenomenon has been referred to as the Benjamin–Feir instability, which was discovered in the 1960s after vain attempts to make a perfectly regular series of waves in a wave tank [91,112]. The Benjamin–Feir instability involves the transfer of dissipation of large-scale structures to small-scale eddies via vortex interactions. In water wave tank experiments, an initially regular series of waves always became irregular, with some waves higher than others.

Let us now return to Fig. 4 and give more insight into the three displayed solutions. They correspond to a particular value of a in the family of one-parameter solutions

Figure 4

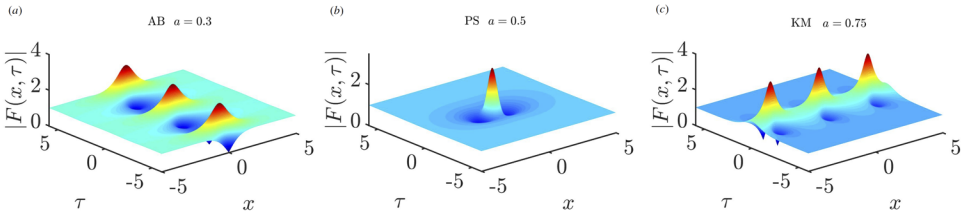

Three-types of breathers obtained using analytical formulas Eq. (34): (a) Akhmediev breather; (b) Peregrine soliton; (c) KM (parameters provided in the inset).

Figure 5

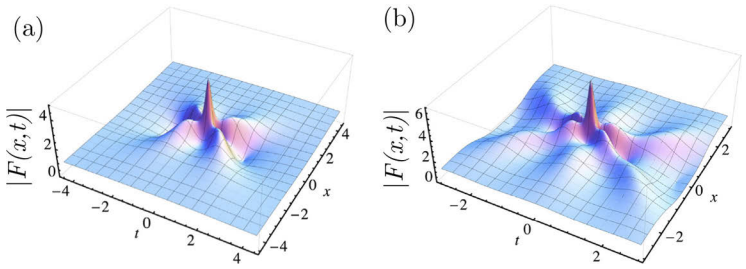

Examples of higher-order rogue wave solution of NLSE. (a) Solution of the second order. Figure 4 reprinted with permission from Akmediev *et al.*, Phys. Lett. A **373**, 675–678 (2009) [47]. Copyright 2009 by the American Physical Society. (b) Third-order rogue wave solution. Reprinted with permission from Akhmediev , Front. Phys. **8**, 631 (2021) [44]. Copyright 2021 by Frontiers Media S.A.

of Eq. (34). Solutions over the range $0<a<0.5$ are the Akhmediev breather, with MI instability growth rate being maximal at $a = 0.25$. Increasing a further gives the Peregrine soliton in the limit $a \to 0.5$. When $a>0.5$ the solution exhibits localization in time τ, but becomes periodic along the spatial direction. Such a soliton is referred to as the KM soliton which is shown in Fig. 4 for $a = 0.75$. Note that, higher-order rogue waves can also be analytically obtained from the NLSE and they are not discussed here (see a recent overview on this issue in Ref. [44]). Typical higher-order rogue waves are displayed in Fig. 5. These analytical solutions have motivated researchers to gain insights into the formation of rogue waves in nonlinear dispersive systems which have been verified experimentally in a 1D setting, both in optics and in hydrodynamics [52–56,113]. In this regard, fiber optics provides an excellent experimental platform as dispersion and nonlinearity effects could be controlled to yield a propagation regime where the NLSE is valid. This is done by injecting a multi-frequency field into a nonlinear fiber, using a method developed for coherent pulse generation in telecommunication [96,114]. Before embarking upon discussing possible mechanisms which lead to rogue waves, we establish similarities between optical and hydrodynamical systems in a quantitative way.

2.4. Similarities between Ocean Waves and ORWs

Establishing similarities between optics and photonics with fluid mechanics has remained an open challenge ever since the derivation of the Lorentz model by Haken [115]. The Lorentz model was originally derived to describe the Bénard convection. Starting from the Maxwell–Bloch equation which describes a single-mode laser, Haken derived for the first time a one-to-one analogy between optics and fluid mechanics

[116]. In this analogy, the transport processes such as dispersion, diffraction, or diffusion are neglected. This implies that the field envelope is assumed to be homogeneous along with transverse and longitudinal coordinates. When transverse and dispersive effects cannot be neglected, for instance, in broad-area optical devices several order parameter equations have been proposed in the literature such as the well-known laser Bernoulli [117], Kuramoto–Sivashinsky [118], and Ginzburg–Landau equations [119,120].

In laser physics, the Kuramoto–Sivashinsky equation has been derived close to the lasing threshold [118]. This equation holds in the limit of small atomic detuning, with the resulting dynamics governed by the phase of the optical signal. While in fluid mechanics, this phase equation has been used to model diffusive instabilities inherent in a laminar flame front [121,122]. In the same vein, the complex Ginzburg–Landau equation has been derived for laser systems [119,120], which also describes a large class of fluid mechanics phenomena. This includes superconductivity, superfluidity, and also extends to other systems such as liquid crystals, Bose–Einstein condensation [123,124], and even to string theory [125]. The Swift–Hohenberg equation, on the other hand, has been used to describe dynamics in laser systems (complex equation), and also in passive systems such as driven optical cavities (real equation) [126–128]. In particular, it has to be noted that the real Swift–Hohenberg equation has been first derived for studying convective patterns generated by the Bénard–Marangoni instability [129].

We discuss the link between optics and hydrodynamics in a quantitative way using the NLSE. For the ease of readability, we rewrite Eq. (33) in a 1D setting:

$$\partial_t F = \frac{i}{2}\partial^2_{\tau\tau} F + i\eta |F|^2 F. \tag{35}$$

In optics, the variable F represents an envelope of modulated electromagnetic carrier waves along with the fiber. This quantity in optics is obtained by normalizing the envelope amplitude by the square root of the power (P). The variable t is the dimensionless time, which is equivalent to z, the longitudinal coordinate along the fiber, and L is the cavity length. As remarked earlier, the parameter η is either 1, which is the self-focusing case, or -1 for the defocusing type of nonlinearity. The parameter L in optics is given by $1/(\gamma P)$ where γ is the nonlinearity parameter which ranges from 1 to 100 (W km^{-1}). Typical rogue wave characteristics in fiber optics can lead to peak power intensities in the range 0.1–10 kW. These extreme events have a very short time duration of the order 1–10 ps. The variable τ represents the retarded time, i.e., the time in the reference frame moving with the group velocity of light normalized by the nonlinear length L as $\tau = (|\beta_2|L)^{1/2}$. Here β_2 is the coefficient of the second-order chromatic dispersion. In fiber optics $\beta_2<0$, with absolute values lying in the range of 0.1–20 ps^2 km^{-1}, whereas in hydrodynamics the nonlinear length L is governed by the wavenumber and the mean velocity of the water surface given by $L = 1/(k^3U^2)$. The wavenumber k is determined by the frequencies present in the system arising naturally, or indeed could be chosen under laboratory settings by sending directional waves triggered using wavemakers. For instance, in 1D settings experiments which were carried out in water wave tanks for k in the range [1–16] m^{-1} [130], with frequencies lying in the range 0.2–6.3 rad s^{-1}. The linear dispersion relation linking these frequencies with the wavenumbers is given by $\omega^2 = gk$ for deep water waves, which still holds for the water of intermediate-depth [131]. The variable τ which governs the time scale of the system depends on the nonlinear length L as $\tau = (2\pi L/g)^{1/2}$ where g is the acceleration due to gravity.

Rogue waves have been attributed to mechanisms that generate large envelope amplitudes F modeled by the NLSE, which takes into account group velocity dispersion and

nonlinearity. When these two effects act together, this leads to the nonlinear focusing scenario corresponding to $\eta = 1$. In this regard, the origin of the nonlinearity in optics and hydrodynamics are both governed by a nonlinear dispersion relation [99,113,132]. It is important to note that optical waves with higher amplitudes of F propagate at reduced velocities whereas in hydrodynamical systems such as in water wave tanks, waves with higher amplitudes, propagate at increased velocity. In optical systems, nonlinearity and dispersion are either self-focusing or defocusing unlike in hydrodynamics where directional focusing of waves or random superposition of independent wave train may lead to the generation of extreme events which are not limited to the self-focusing case as in optics. The time-lens measurement technique has been used to qualitatively compare the experimental results generated from the MI of a CW in a single-mode fiber with the theoretical one obtained from the NLSE [17,37].

We remind the reader that the analogy between optical and hydrodynamical systems is strictly limited to the 1D setting. This is mainly due to the fact that the NLSE supports solutions only in the 1D setting because in two or more dimensions, this model does not support solutions due to collapse which is mathematically demonstrated by Ref. [108]. In the following section, we discuss some possible mechanisms in conservative systems which could explain rogue waves in optical systems (1D setting), and in controlled circular laboratory water wave tanks (2D settings). In this regard, the analytical solutions of breathers via collisions is of particular interest as it is considered to be one of the main mechanisms which generate rogue waves in these nonlinear dispersive systems. This follows in the subsequent subsection where the collision of these breathers is discussed following which we present the scenario from a recent study made in circular wave tanks where the Draupner wave is recreated experimentally.

3. COLLISION AND WAVE BREAKING

3.1. Rogue Wave Observation in Water Wave Tanks

In this section, we summarize the first experimental observations of the Peregrine soliton in a water wave tank [54]. The evolution of the surface gravity waves in the water wave tank is described by the NLSE, which is known to be valid for capturing weakly nonlinear evolution of narrowband processes. The formation of rogue waves in oceans have been attributed to the underlying breather-type solutions of the governing NLSE, such as the Akhmediev breather, Peregrine soliton, and KM soliton [23,48,133,134]. While modeling deep water waves using the NLSE, the Peregrine soliton is considered as an ideal candidate as it is localized both in space and time, and as such, it describes unique wave events. It is to be noted that the Peregrine solution is a limiting case of an Akhmediev breather when the period of modulations is taken to be infinite.

To the best of the authors' knowledge, the first observation of an isolated rogue wave in a water wave tank was shown in Ref. [54]. Specifically, Chabchoub *et al.* observed a Peregrine-type breather solution experimentally in a water wave tank by providing a direct analytical comparison with the solutions of the NLSE. The experiments were performed in a water wave tank of dimensions 15 m × 1.6 m × 1.5 m with 1 m water depth. The schematic of the experimental setup is shown in Fig. 6(a). A flap-paddle activated by a hydraulic cylinder is used at one end of the tunnel to generate water wave dynamics in the tank which produces a periodic wave with about 1 cm amplitude. The dynamics on the water surface is quantified by measuring the surface elevation across the test section. The deep water waves are described by the NLSE as shown in Refs. [54,108].

For comparing experimental data with the analytical solution of the NLSE, the Peregrine breather solution has to be written in dimensional units (see [54]). In their

Figure 6

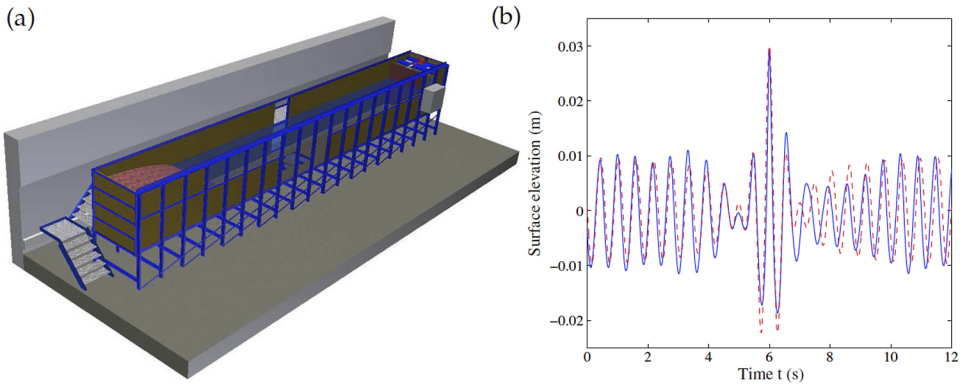

(a) Schematic setup of the water wave tank used in Ref. [54]. (b) Comparison of the experimentally measured surface height at the position of maximum amplitude corresponding to a rogue wave (shown in blue) with the theoretical Peregrine solution (shown in red). Figure 5 reprinted with permission from Chabchoub *et al.*, Phys. Rev. Lett. **106**, 204502 (2011) [54]. Copyright 2011 by the American Physical Society.

study, a_0 is the dimensional far-field amplitude selected to be 0.01 m. The wavelength of the carrier wave is set to be $\lambda = 0.54$ m, corresponding to a wavenumber of about $k = 11.63\ \mathrm{m}^{-1}$ with an angular frequency $\omega = 10.7\ \mathrm{s}^{-1}$. As remarked in Ref. [54] it has to be ensured that the wavelength of the carrier wave should be large enough to ignore surface tension effects, while at the same time still small enough to have sufficient tank length to develop the wave evolution described by the Peregrine solution. By measuring the surface elevation of the water wave across the tank at different streamwise locations allows for a direct comparison with this analytical Peregrine solution. Further details on the experimental procedure can be found in Ref. [54].

Figure 6(b) shows the surface-height measurement at a position close to the maximum envelope amplitude across the water wave tank. It can be seen that while the amplitude of the carrier wave is around 1 cm, the maximum surface height of the breather is almost exactly three times reaching a value of 3 cm. This indicates the formation of a rogue wave with amplitudes greater than twice the SWH, confirming the existence of rogue waves. The periodic wave shown in Fig. 6(b) reveals a deep trough next to the breather's maximum either side of the wave crest. In addition, the return from the state of the extreme wave back to the state of a periodic wave in the experiment is almost symmetric in time, as expected from the underlying theory. Indeed, carefully controlled experimental procedures such as that presented in Ref. [54] allows for a controlled observation of rogue waves in water wave tanks. In addition, they also reveal the role of breather-type solutions of the NLSE in the formation of rogue waves in oceans, where detailed experimental measurements are typically incomplete and rare. We now present another interesting study where the observation of super rogue waves, which are higher-order breathers in water waves, are experimentally shown [130].

3.2. Higher-Order Breather Solutions in Water Waves

The Peregrine soliton discussed in the previous section is characterized by an amplification factor of three. By considering a higher-order rational solution, localized in both space and time, allows one to boost the peak amplitude of the carrier wave on the water surface by a factor of five. These solutions are detailed in Ref. [130]. In order to excite super rogue waves in water tanks, as in the earlier study, one has to fix the

initial amplitude of the carrier wave a_0 and the wavenumber k. In doing so, one fixes the steepness of the carrier wave which is given by $\epsilon = a_0 k$.

Figure 7(a) shows the evolution of the temporal profile of the surface elevation along the downstream direction from the paddle (location of the wavemaker) as a function of time. The amplification of the water surface as the wave propagates along the test section can be clearly seen with significant amplification occurring at a distance of nine units from the flap-paddle. The high-order wave packet generated by the wavemaker's paddle evolves to a super rogue wave as it propagates along the water wave tank. This is further quantified in Fig. 7(b) which compares the theoretical prediction at the position of maximal amplitude with the experimentally measured surface height elevation. An amplification factor of five has been observed indicating the formation of higher-order super rogue waves. Even higher amplifications were obtained for higher values of the steepness of the carrier wave.

The role of MI in governing the growth of small-amplitude pulses leading to higher amplitudes resulting in ocean waves was first discussed by Peregrine [51]. The presence of multiple frequencies in optical and hydrodynamical systems renders explicit modeling rather complicated. However, the problem can be simplified and effectively reduced to the interaction of two independent frequencies within the positive-gain band. For instance, the collision of Akhmediev breathers have been observed experimentally in nonlinear fiber optics [58], confirming the fact that coherent structures may emerge locally in a turbulent environment when the phase difference between the colliding structures is optimal. The collision of Peregrine solitons has been derived analytically [56,135]. The phase difference between the interacting solitons plays a significant role in deciding the initial conditions required for the formation of rogue waves. These solitons are localized along two directions which are well separated. Such collisions can happen in nonlinear systems frequently leading to the generation of high-intensity pulses of small widths. These bounded states of solitons are unstable to variations of the relative phase difference between them. However, no stable bounded states of two solitons in 1D homogeneous media have been reported in the literature. This is due to the fact that these solitons do not have an oscillatory tail that connects the LS with the homogeneous background rendering bounded states impossible.

3.3. 2D Settings

In 2D settings spatiotemporal rogue events have been experimentally observed in the context of optical multiple filamentation in Ref. [136]. In this study the transient appearance of bright spots in the beam profile of optical filaments formed in xenon were investigated experimentally. In this regard, optical filaments are dynamic light structures with an intense core, which propagate over extended distances, which is significantly larger than the usual diffraction length in the given medium. This effect allows the maintenance of a narrow beam size without any external guidance which is governed by two counteracting nonlinear optical mechanisms which are self-focusing and plasma defocusing. There exists a critical power $P_c \approx 0.15\lambda^2/n_0 n_2$ above which the breakup of a spatially homogeneous beam profile into one or several highly localized strings, where λ is the wavelength and n_0 and n_2 are the linear and the nonlinear index of refraction, respectively. The experimentally observed filamentation was numerically investigated using simulations of the NLSE. A snapshot of the formation of multiple parallel optical filaments is shown in Fig. 8. The formation of extreme events was quantified using probability distribution functions to quantify the heavy-tail character which represents the presence of extreme events in such optical cavities. Rogue events that exceed the SWH by a factor of 10 were reported. Of particular interest, mergers between filament strings were identified as a possible microscopic driver mechanism

Figure 7

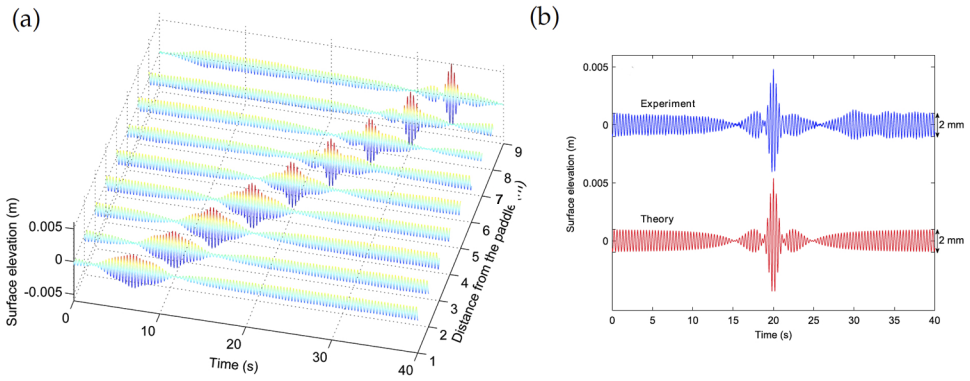

(a) Evolution of the temporal profile of the water-surface elevation along the wave tank demonstrating a super rogue wave formation further downstream from the paddle. (b) Experimental and theoretical confirmation of higher-order rogue waves showing the measured wave profile at the expected position of maximal carrier amplification. Here the background amplitude $a_0 = 0.001$ m, with a steepness of $\epsilon = 0.03$. Figure 6(a) reprinted with permission from Chabchoub *et al.*, Phys. Rev. X, **2**, 011015 (2012) [130]. Copyright 2012 by the American Physical Society.

Figure 8

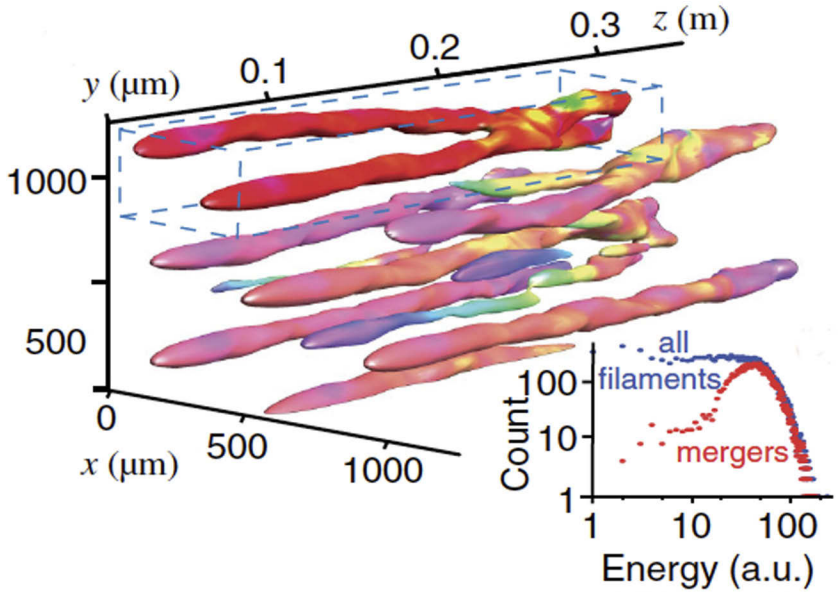

Multiple parallel filament strings along the longitudinal direction z obtained from numerical simulations of the NLSE with the color coding showing the relative phase differences between the optical filaments. Figure 2 reprinted with permission from Birkholz *et al.*, Phys. Rev. Lett., **111**, 243903 (2013) [136]. Copyright 2013 by the American Physical Society.

for the observed rogue events. As the system is 2D as in the ocean surface, such filamentation techniques allows for an excellent experimental platform for studying the phenomenon of rogue waves.

We now turn to an example from hydrodynamical settings wherein significant advances have been made in the past two decades in the context of extreme events, using

Table 1. Summary of the Draupner Wave Reconstruction from Ref. [137] [a]

$\Delta\theta$	h_d(m)	h_u(m)	a(m)	$k_d d$	$k_u d$
0°	24.2	23.5	16.6	1.68	1.85
60°	23.9	23.9	18.0	1.76	1.85
120°	25.4	24.5	17.9	1.76	1.89
Draupner	25.0	25.6	18.5	1.74	1.91

[a]At different crossing angles, $\Delta\theta$, quantified using the down- and up-wave heights h_d and h_u, the total crest height above still water a, and steepness $kh/2$ to scale the waves. The values of the wavenumber k were calculated using the linear dispersion relationship $\omega^2 = gk\tanh(kd)$. The values corresponding to the iconic Draupner wave measured on the North Sea are also indicated. Reprinted with permission from McAllister *et al.*, J. Fluid Mech. **860**, 767–786 (2019) [137]. Copyright 2019 Cambridge University Press.

statistical, numerical, and experimental tools [131,133,137–139]. The Draupner wave was recently recreated in controlled laboratory settings by McAllister *et al.* [137] to gain an understanding of the role of the type of wave breaking for crossing and non-crossing waves. The conditions at the Draupner platform based on hindcasting studies have indicated the presence of wind fields at different angles [137,140]. More pertinently, the question of interest raised by McAllister *et al.* [137] were on the directional conditions of the waves whose interactions lead to large crest amplitudes, without crest-amplitude-limiting breaking, as the crest amplitude from a single wave train is limited due to breaking. Their study showed that the breaking mechanism can be fundamentally altered, with the crest amplitude not being limited due to breaking, but rather resulting in upward jet-like behavior.

As a brief summary, McAllister *et al.* [137] performed experiments in a circular wave tank surrounded by 168 wavemakers, which allows for the creation of waves traveling in all directions. For instance, by sending out waves at different frequencies toward the center of the circular tank that travel at different speeds, they were able to create a "spike" wave which arises due to the constructive interference with the tank. It is to be noted that previous numerical studies could reproduce the Draupner wave only by the crossing of two wave groups, due to the interaction between the wave trains at a specific angle [131,141]. Based on this, McAllister *et al.* [137] created two different wave groups traveling toward the center of the tank, and varied the angle between them. They found out that a "freak wave" or a "rogue wave" formed only when the difference in angle between the two wave groups was around $\Delta\theta \approx 135°$.

Figure 9 shows a summary of the observations from Ref. [137] for different values of $\Delta\theta$, the angle between the wave groups. They observed that the breaking process when the angle between the wave groups was large changes significantly. For $\Delta\theta = 0°$, one can see that the wave energy is traveling unidirectionally, similar to what can be observed at a beach, with the waves breaking in a "plunging"-type manner, thereby limiting the maximum crest amplitude. When the angle between the wave groups was changed to $\Delta\theta = 120°$, a "spouting"-type wave breaking can be observed in the form of upward projected jets. This type of wave breaking does not limit the wave height under the crossing-sea conditions, and in fact enhances the wave height, which could explain the Draupner wave observed in the North Sea. A summary of the Draupner wave features are provided in Table 1. The study clearly shows that the wave breaking plays a key role in the formation of extreme waves, which are, in turn, governed by the crossing angles between the traveling wave groups.

4. DIFFRACTIVE AND DISPERSIVE OPTICAL RESONATORS

The above theory of rogue waves in the context of optical systems based on the NLSE holds only in the 1D setting. However, beam collapse prevents the NLSE to have bounded solutions in more than one dimension which renders the formation of high-dimensional rogue waves impossible. There exist several mechanisms leading to the

Figure 9

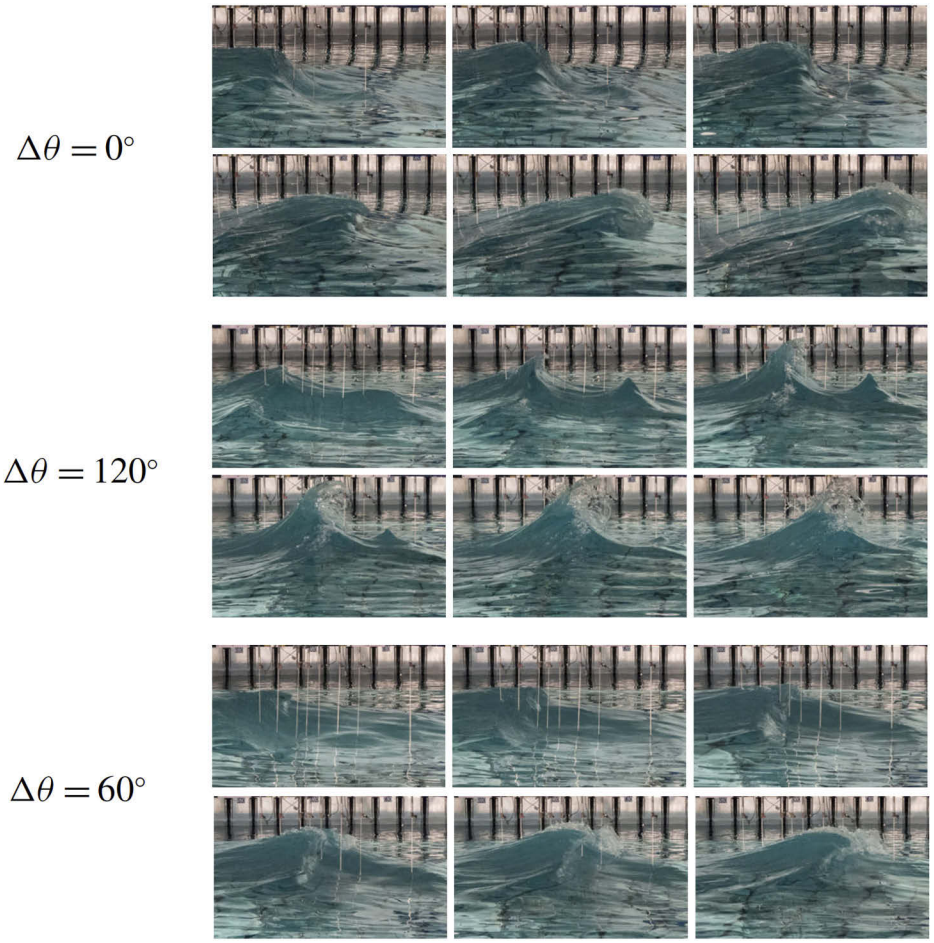

A summary of the observations from [137] where $\Delta\theta$ is the angle between the two wave groups. The still images of the free surface were taken at intervals of 100 ms (0.6 s at field scale), with the time sequence increasing from left toward right. Reprinted with permission from McAllister *et al.*, J. Fluid Mech. **860**, 767–786 (2019) [137]. Copyright 2019 Cambridge University Press.

stabilization of 2D solutions such as SAs, non-local coupling, or optical cavities. Due to this reason, we focus on optical cavities filled with a nonlinear material by using the mean-field approach, which was first used to describe Kerr media and semiconductor materials: the LLE. This approach includes pumping and dissipation, in addition to nonlinearity, dispersion, and/or diffraction [60]. Furthermore, the LLE is by now recognized as a very accurate model to capture the physics of Kerr optical frequency comb generation using integrated ring resonators [142], and in whispering gallery mode cavities [143]. In what follows, we focus on dissipative rogue wave formation in nonlinear optical cavities. For this purpose, two dissipative systems are considered: the driven Kerr optical cavities subjected to an optical injection, and the broad-area surface-emitting lasers with a SA.

4.1. The Lugiato–Lefever Model

In free propagation, the evolution of the envelope of the electric field inside the Kerr material can be described by the standard NLSE Eq. (35). In what follows, we consider a Fabry–Perot cavity filled a Kerr medium and driven coherently by an injected beam with an instantaneous Kerr media (see Fig. 10).

Figure 10

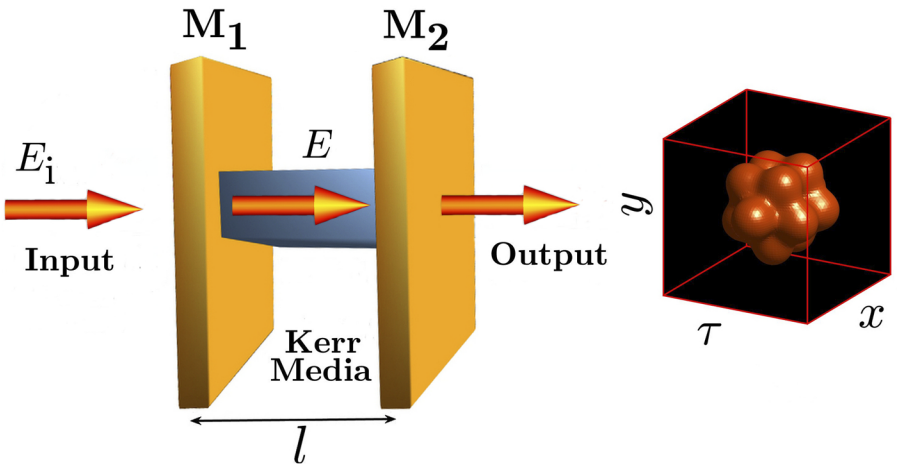

Schematic setup of an optical cavity filled with a Kerr medium. The cavity is driven by an external field E_i. The mirrors $M_{1,2}$ are identical and their reflection and transmission coefficients are denoted by ρ and θ, respectively. Reprinted with permission from Ref. [62].

The cavity is driven by a coherent plane wave wherein the intracavity field undergoes a coherent superposition with the injected field at the input of the mirror. This process corresponds to the following cavity boundary conditions

$$F^{p+1}(0,x,y,z) = \rho F^{p}(l,x,y,z)\exp(i\phi_0) + \theta F_i, \tag{36}$$

where ρ and θ are the reflection and transmission coefficients at the input and the output mirrors. The above equation provides a relation between the intracavity field envelope F^{p+1} at the input of the cavity after the $p+1$ round trip and the field $F^{p}(l,x,y,z)$ at the output after p round trips, where l is the cavity length. The phase shift ϕ_0 accounts for the linear phase accumulated by the intracavity field during one round trip time; t_r. The evolution of the intracavity field is, thus, slow at the time scale of the order t_r.

The NLSE (35) supplemented by the cavity boundary conditions (36) constitutes an infinite-dimensional map. In the mean-field approach based on a good cavity limit and high Fresnel number, this infinite-dimensional map can be reduced to a single partial differential equation referred to as the LLE [60]. To perform this reduction, we consider cavities with high finesse. In this case, the transmission coefficient θ is much smaller than unity ($\rho \approx 1-\theta^2/2$). In this limit, the temporal evolution of the field within the cavity is slow compared with the round trip time t_r. Therefore, this temporal evolution can be considered as continuous by replacing the map index p by a slow time scale t for the modeling of the field envelope evolution at the input of the cavity, i.e., the point $z=0$. This can be realized by defining the continuous variable $E(t,x,y,\tau)$ as the intracavity field envelope at $z=0$ as

$$F(t=pt_r,x,y,\tau) = F^{p}(z=0,x,y,\tau), \tag{37}$$

where p is a positive integer number. The time t describes the slow evolution of the intracavity field from one round trip to another, while the structure of the intracavity field changes at the fast time scale τ. The slow time derivative can be defined as

$$\partial_t F(t=pt_r,x,y,\tau) = \frac{F^{p+1}(z=0,x,y,\tau) - F^{p}(z=0,x,y,\tau)}{t_r}. \tag{38}$$

When the cavity possesses a high finesse, the cavity resonances are narrow, and the injected field is coupled to the cavity only if the system is close to resonance.

This means that intracavity field does not vanish when the system operates close to resonance where the phase shift ϕ_0 is close to 2π. This implies that both the linear cavity detuning $\delta_0 = 2\pi m - \phi_0$ with m is an integer and the nonlinear cavity phase shift lF^2 must be much smaller than unity. In addition, we assume that the cavity length is much shorter than the characteristic dispersion and diffraction lengths of the intracavity field. With these approximations together with the fact that we focus on the high-finesse cavities, we can rewrite Eq. (36) as

$$F^{p+1}(0,\mathbf{r}) = \theta F_i + \left(1 - \frac{\theta^2}{2} - i\phi_0\right) F^p(l,\mathbf{r}), \tag{39}$$

with $F^{p+1}(0,\mathbf{r}) = F^{p+1}(0,x,y,\tau)$ and $F^p(L,\mathbf{r}) = F^{p+1}(0,x,y,\tau)$. By averaging the right-hand side of the NLSE (35) over one cavity length, we obtain

$$F^p(z=l,\mathbf{r}) - F^p(z=0,\mathbf{r}) = \frac{il}{2}\nabla^2 F^p(z=0,\mathbf{r}) + il|F^p(z=0,\mathbf{r})|^2 F^p(z=0,\mathbf{r}). \tag{40}$$

By combining Eqs. (39) and (40) and by taking into account Eqs. (37) and (38) together with the above-mentioned approximations consisting of assuming that θ, ϕ_0, $l|F^2|$, and l are small quantities, the 3D LLE reads [144,145]

$$\begin{aligned} t_r \frac{\partial F}{\partial t} = & \sqrt{\theta} F_i - \left(\kappa + i\phi - i\gamma l|F|^2\right)F \\ & + i\left(\frac{l}{2q}\nabla_\perp^2 + \frac{\beta_2 l}{2}\frac{\partial^2}{\partial\tau^2}\right)F. \end{aligned} \tag{41}$$

Here $E = E(x,y,\tau,t)$ is the normalized slowly varying envelope of the intracavity field and F_i is the input field. The time t corresponds to the slow-time evolution of F over successive round trips, whereas τ accounts for the fast time in a reference frame traveling at the group velocity of light in the Kerr medium. The cavity round trip time is denoted by t_r. The 2D diffraction is described by the Laplace operator $\nabla_\perp^2 = \partial_{xx} + \partial_{yy}$ acting on the transverse plane (x,y). The diffraction coefficient is inversely proportional to the wavenumber modulus in the cavity material $q = \omega_0 nl/c = 2\pi n/\lambda_0$ where ω_0 is the injected field frequency, λ_0 is the wavelength in vacuum, n is the linear refractive index, and c is the speed of the light. The second derivative with respect to τ describes the group velocity dispersion. The chromatic dispersion coefficient β_2 is considered to be positive assuming that the Kerr cavity operates in anomalous dispersion regime. The nonlinear coefficient $\gamma = 2\pi n_2/\lambda_0$ is the nonlinear coefficient with n_2 is the nonlinear refractive index of the Kerr material considered. The transmission coefficient θ is supposed to be much smaller than unity. The length of the cavity is denoted by l and $\phi_0 = 2\pi l/\lambda_0$ is the linear phase shift accumulated by the intracavity field over the length l. To simplify further and to reduce the number of parameters describing the time evolution of the intracavity field, we introduce the following changes:

$$\begin{aligned} (x,y) \to & \sqrt{\frac{l}{2q\kappa}}(x,y), \quad (t,\tau) \to \left(\frac{t_r}{\kappa}t, \sqrt{\frac{\beta_2 l}{2\kappa}}\tau\right), \\ F_i \to & \quad \kappa\sqrt{\frac{\kappa}{\gamma\theta l}}E_i, \quad \text{and} \quad E \to \sqrt{\frac{\kappa}{\gamma l}}E. \end{aligned} \tag{42}$$

Under these changes, the generalized LLE (41) takes its dimensionless form

$$\frac{\partial E}{\partial t} = E_i - (1+i\delta)E + i\left(\nabla_\perp^2 + \frac{\partial^2}{\partial\tau^2}\right)E + i|E|^2 E, \tag{43}$$

where $\delta = \phi_0/\kappa$ is the cavity detuning parameter. The LLE is a driven damped NLSE. It was first derived to describe the plasma driven by a radio-frequency field [146,147] and the condensate in the presence of an applied ac field [148].

Kerr resonators constitute a basic configuration in nonlinear optics and photonics which allows for the generation of 1D and 2D spatial rogue waves described by the LLE. The latter was first derived to describe the dynamics in passive resonators [60], which was later on extended to fiber optics [149], left-handed materials [150], whispering gallery mode cavities [144], integrated ring resonators [69], and chains of coupled silver nanoparticles embedded in glass [151]. A discrete version of the LLE has been established to model coupled-waveguide resonators [152–155], or extended Josephson junction [156]. The LLE constitutes a paradigm for the study and for the understanding of various dynamical properties of laser fields confined in nonlinear optical resonators such as hard-mode symmetry-breaking instability and self-organization either in time and/or space (see a recent overview [157]). The mean-field approach has been compared with the propagation model supplemented by cavity boundary conditions in Refs. [158,159].

The model, Eq. (43), supports stationary localized [61,160] and self-pulsating localized [161] structures. In the conservative limit, where injection and dissipation are both small, LSs have analytical solutions [88,162–164]. LSs can exhibit regular time oscillations leading to complex behavior (see also the recent review on the link between the LLE and the driven damped sine-Gordon and the Lugiato–Lefever model [165]). It is also worth mentioning several interesting works on their bifurcation structures which belong to the class of homoclinic snaking type of instability [166–168]. Their relative stability analysis as well as their snaking bifurcation diagram have been reported [169]. When polarization degree of freedom is taken into account within Kerr resonators, new MIs appear [170–172] and vector LSs are predicted [173–176]. However, when the Kerr resonator is operating in a dispersion regime, another class of LSs resulting from interactions may be generated in scalar [177–182] and vectorial cases [183,184]. The stabilization mechanism of these localized states is attributed to a front locking mechanism in the bistable regime [185,186]. Their bifurcation diagram exhibits a heteroclinic collapsed snaking type of bifurcation.

4.2. Linear Stability Analysis

In the absence of diffraction and dispersion, the homogeneous steady-state solutions of Eq. (43) satisfying $\partial_t E = 0$ and $\nabla^2 E = 0$ are

$$I_i = I_s \left[1 + (\delta - I_s)^2\right], \tag{44}$$

with $I_s = |E_s|^2$ and $I_i = E_i^2$ are the intracavity field intensity and the injected field intensity, respectively. For $\delta<\sqrt{3}$ ($\delta>\sqrt{3}$) the transmitted intensity as a function of the input intensity I_i is monostable (bistable). At the onset of optical bistability, there exist a second-order critical point where the output versus input characteristics has an infinite slope. The critical detuning at the onset of optical bistability is $\delta = \sqrt{3}$.

When diffraction and dispersion are taken into account, spatial and/or temporal fluctuations can destabilize the system and allow for the formation of dissipative structures. The spontaneous transition from a homogeneous steady state to a periodic structure is a general feature of many far from equilibrium systems, and has motivated many studies since the pioneering work of Turing [187], followed by the physical interpretation by Prigogine [188,189]. It concerns almost all fields of natural science such as biology, chemistry, ecology, physics, fluid mechanics, optics, and photonics (see the reviews on this issue [189–197]).

The linear stability analysis of the homogeneous steady states can be performed by linearizing Eq. (43) and its complex conjugate around E_s and E_s^* as

$$[E(t,x,y,\tau),E^*(t,x,y,\tau)] = (E_s,E_s^*) + \left[\delta E(t,x,y,\tau),\delta E^*(t,x,y,\tau)\right]\exp(i\mathbf{k}.\mathbf{r}+\lambda t), \tag{45}$$

with $\mathbf{r}=(x,y,\tau)$ and $\mathbf{k}=(k_x,k_y,k_\tau)$. By replacing the perturbation Eq. (45) in Eq. (43) and its complex conjugate, and linearizing, we obtain the characteristic equation

$$\lambda^2 + 2\lambda + \partial_{I_s} I_i + \left[k^2 - 2(2I_s-\delta)\right]k^2 = 0, \tag{46}$$

where $\partial_{I_s} I_i = 1+(I_s-\delta)(I_s-\delta)$ is the slope of the homogeneous steady-state curve. At the turning point or a limit point the slope vanishes, i.e., $\partial_{I_s} I_i = 0$. The coordinate of the turning points are $I_l^{\pm} = [2\delta \pm (\delta^2-3)^{1/2}]/3$. The corresponding injected field intensities are $I_l^{\pm} = I_l^{\pm}[1+(\delta - I_l^{\pm})^2]$. The critical point associated with the bistability is reached when these two turning points coincide, i.e., $I_l^- = {}_l^+$.

In the presence of small fluctuations depending on the space (x,y) or the retarded time τ, the homogeneous steady state undergoes a symmetry-breaking instability when the eigenvalue λ vanishes for a finite wavenumber. Above this instability point, there exist a finite band of unstable Fourier modes $k_<k<k_+$, with

$$k_\pm^2 = 2I_s - \delta \pm \sqrt{I_s-1}, \tag{47}$$

which are linearly unstable and trigger the spontaneous evolution of the intracavity field toward a stationary, periodic solution that occupies the whole space available in the (x,y,τ) Euclidean space. The threshold associated with the symmetry-breaking instability is obtained when $k_- = k_+$. The critical intracavity field intensity is $I_m = |E_m|^2 = 1$ and the corresponding critical injected field intensity at the onset of the instability is $I_{im} = E_{im}^2$. At this bifurcation point, the critical wavelength of the pattern which emerges from the symmetry-breaking instability or MI is $\Lambda_c = 2\pi/\sqrt{2-\delta}$. When $\delta = 2$, the critical wavelength becomes infinite, i.e., zero wavenumber. For this particular value of the detuning parameter, the MI coincides with the lower turning point ($I_{im} = I_l^-$) of the homogeneous steady states. This symmetry-breaking bifurcation is known as the Turing instability [187] and is often called MI in the context of optics and photonics. The resulting patterns emerging from that bifurcation are called dissipative structures which are characterized by an intrinsic wavelength that is determined only by dynamical parameters and by physical boundaries or other external effects [188,198]. Self-organization and symmetry-breaking phase transition or instability leading to the spontaneous formation of spatially periodic patterns such as rolls or hexagons have been observed in almost all driven away from equilibrium systems. Generally speaking, the mechanism responsible for the stabilization of these patterns rests on the balance between two opposite processes: (i) diffraction (and/or diffusion or thermal diffusivity) that tends to restore spatial uniformity, and nonlinearity which is typically generated by light–matter interactions which are responsible for the amplification of spatial inhomogeneities, (ii) pumping or injection which compensates losses or dissipation. The balance between these two opposite effects can stabilize spatial structures. The physical interpretation and the possibility to have spatial oscillations in far from equilibrium systems have been proved by Prigogine and Lefever [188,198]. They have shown that the transition from uniform state to a spatial order is not in contradiction with the second principle of thermodynamics extended to out of equilibrium systems.

Note that in hydrodynamics, and in particular in the Bénard cells experiments [199], discovered in 1900, the emerging dissipative structures wavelength is not intrinsic but rather extrinsic. This famous experiment consists of a fluid between two horizontal

conducting plates in the field of gravity and heated from below. The fluid will reach the state of thermodynamic equilibrium, in which there is no bulk motion and both temperature and density are constant. In this case fluctuations such as local increase of temperature will be damped out. This is a conduction regime so that the fluid remains at rest. However, if we increase further the bottom plate temperature, and above some threshold, the fluid starts to exhibit a bulk movement leading to spatial order in the form of well-structured convection cells. These cells that emerge in the convective regime generate an extrinsic dissipative structures. This is because their wavelengths are determined by external factors such as the boundaries and the thickness of the fluid layer considered [198].

4.3. Optical Crystals

The LLE supports periodic dissipative structures that emerge spontaneously from MI. When using guided wave structures, the intracavity field is spatially stabilized in the transverse plane-(x, y), and therefore in this case diffraction can be neglected. In a 1D setting, periodic structures have been observed using all-fiber resonators [200]. When, however, diffraction cannot be neglected when using broad-area devices, the periodic patterns such as rolls or hexagons exist as shown in Refs. [61,201]. Analytical analysis based on a pattern selection process and a relative stability analysis have proved that only hexagonal structures of the $H0$ are stable over other possible periodic transverse structures [202]. When diffraction and dispersion have a comparable influence on the system, 3D dissipative structures are formed. These structures consist of self-organized light-bullets traveling in the cavity and have been reported in nonlinear Kerr cavities [145], and optical parametric oscillators [145,203].

At that bifurcation point, the homogeneous steady-state solution of the LLE (44) becomes unstable with respect to modes satisfying the relation, $k_x^2 + k_y^2 + k_\tau^2 = 2 - \delta$. Beyond this critical point, there exists a finite band of unstable Fourier modes lying on a sphere with the radius $k_c = \sqrt{2 - \delta}$. These modes are arbitrarily directed in the Fourier space (k_x, k_y, k_τ) because the system is isotropic. Although a large number of unstable modes may be excited along arbitrary directions, a periodic optical crystal is selected and emerges due to the nonlinear interaction. In the linear regime, crystals, or 3D periodic patterns, can be approximated by a linear superposition of n pairs of opposite wave vectors k_j lying on the critical sphere of radius k_c as

$$E(\mathbf{r}, \mathbf{t}) = \mathbf{E_s} + \mathbf{e} \sum_{\mathbf{j=1}}^{\mathbf{n}} \mathbf{A_j} \exp(\imath \mathbf{r}.\mathbf{k_j}) + \mathbf{c}.\mathbf{c}., \tag{48}$$

where $\mathbf{e}$ the eigenvector of the corresponding Jacobian matrix associated with the zero eigenvalue. The lamellae and rhombic structures are characterized by $n = 1$ and $n = 2$, respectively, and the 3D hexagons or hexagonally packed cylinders (hpc) correspond to $n = 3$ with $\sum_{j=1}^{3} \mathbf{k_j} = \mathbf{0}$. The face-centered-cubic (fcc) lattice and the quasiperiodic crystals are obtained for $n = 4$ and $n = 5$, respectively. The body-centered-cubic (bcc) lattice corresponds to $n = 6$. The bcc optical crystals are characterized by six pairs of wave vectors whose coordinates are $k_c(\pm 1, \pm 1, 0)/\sqrt{2}, k_c(\pm 1, 0, \pm 1)/\sqrt{2}$, and $k_c(0, \pm 1, \pm 1)/\sqrt{2}$. These wave vectors form a regular octahedron of eight faces in the form of equilateral triangles.

In a weakly nonlinear regime, normal form analysis in the neighborhood of the 3D MI allows the determination of all the above-mentioned 3D periodic solutions. A relative stability analysis has proved that only the bcc crystals are stable over other possible periodic structures [145]. The results of these analyses are summarized in the bifurcation diagram displayed in Fig. 11(a) taken from Ref. [204]. We plot the amplitude of lamellae, hpc, and bcc lattice as a function of the injected beam with

respect to the relative distance from the MI critical threshold. The bcc/hpc and the hpc/lamellae transitions are both excluded for the 3D LLE. Note that in two dimensions, the well-known hexagon/stripe transition studied in 2D transverse systems is also excluded [202]. As mentioned in an earlier report [145] on 3D crystals, the results were obtained in a perturbative way and they need further support from numerical simulations. More recently, numerical simulations have been performed for both optical crystals and 3D confinement of light in Kerr resonators [62]. The delay in simulating 3D LLE is originated from the fact that the 3D pattern contains a strongly nonlinear term. When performing discretization, this leads to large systems of strongly nonlinear stiff ordinary differential equations [205,206]. The finite-difference methods can lead to non-physical solutions [205]. The spatial discretization of the LLE is done using a Fourier spectral method with periodic boundary conditions [206–208], and the time-stepping is carried out with a fourth-order exponential time differencing Runge–Kutta method [206–208]. All the numerical simulations are carried out on a periodic domain of size 80 units in each direction resolved using 128 grid points, with a time step of 0.01. The initial condition consists of a 3D structure with bcc symmetry. The maximum intensity of the intracavity field associated with the bcc structures is plotted together with their 3D Fourier transform in Fig. 11(b).

4.4. Complexity in Kerr Resonators: Spatiotemporal Chaos

The stationary periodic solutions of the LLE (44) lose their stability when increasing the injected field E_i. Two routes to spatiotemporal regimes of chaos have been identified: period-doubling and extended quasiperiodicity. In the large-intensity regime, complex spatiotemporal dynamics have been reported in driven Kerr cavities [209–212]. Indeed, transitions from either stationary periodic or localized states to the spatiotemporal complex type of behavior are shown in Fig. 12. This figure is obtained by numerical integration of Eq. (43) using periodic boundary conditions. The integration scheme is based on a Runge–Kutta method combined with a pseudo-spectral algorithm. Fig. 12(a) shows a space–time map showing the evolution of the intracavity intensity when changing the injected field amplitude with a step of 0.02 at each 200 time units. The initial condition consists of a stationary localized solution with large intensity.

When further increasing the intensity of the injected field, the localized states become unstable with respect to the 3D pattern forming process at the critical value $I = I_{im}$. For $I_i > I_{im}$, periodic structures emerge. This is because, above the critical value of the intracavity field, the background state or the lower homogeneous steady state is unstable resulting in the breakup of LSs giving rise to periodic structures. When increasing further the injected field intensity, these periodic solutions undergo a Hopf bifurcation leading to the time oscillations of high-intensity peaks of the intracavity field intensity as shown in Fig. 12(c1). The corresponding power spectrum indicates that, indeed, the patterns exhibit harmonic oscillations with the frequency f_1 as shown in Fig. 12(c2). When increasing further the injected field amplitude, E_i, the time oscillatory pattern exhibits a Torus bifurcation with two frequencies f_1 and f_2 as shown in Figs. 12(d1) and 12(d2). For large values of the injection, the system develops an extended quasiperiodic route to chaos as shown in Figs. 12(e1) and 12(e2). This complex behavior is illustrated by Fig. 12(a). When starting with an initial condition obtained for large intensity (E_i) which constitutes an irregular pattern, by slowly reducing the injected field amplitude with a step of 0.02 at each 200 time unit, the intracavity field undergoes interesting dynamics. The intracavity field exhibits a complex behavior and by reducing further the injection, a transition toward a stationary periodic pattern takes place. Such transitions are illustrated in the space–time map of Fig. 12(b).

Figure 11

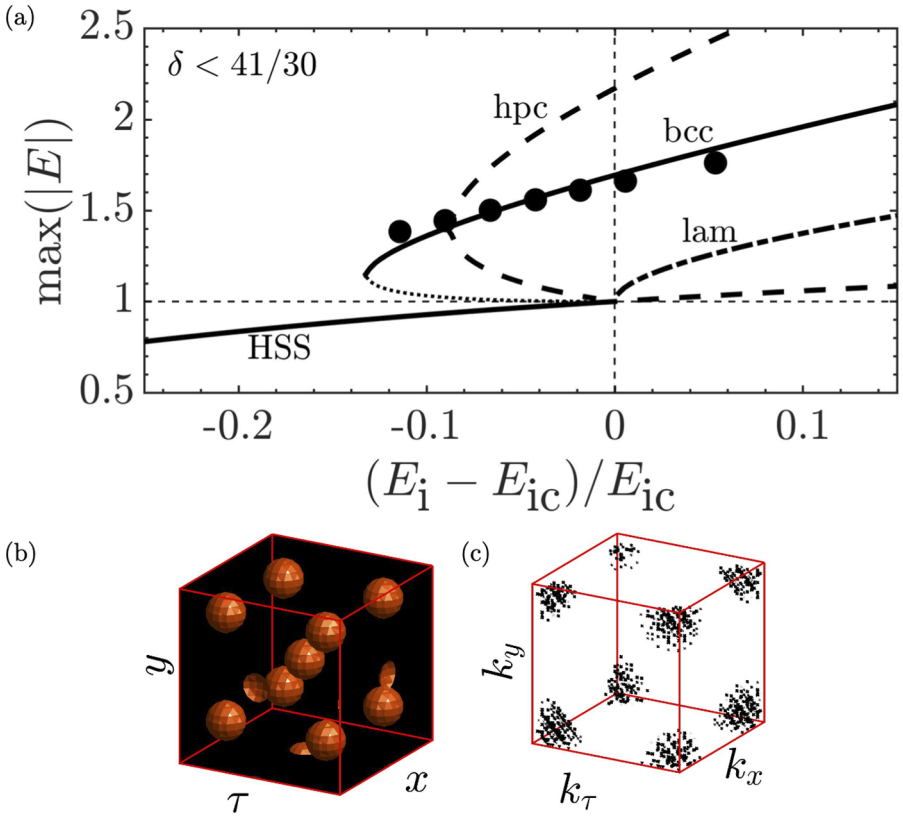

(a) 3D bifurcation diagram of optical crystals obtained for a fixed cavity detuning parameter ($\delta = 0.7$) versus the relative distance from the MI critical point $(E_i - E_{ic})/E_{ic}$. The homogeneous steady state (HSS) is plotted together with optical crystals. The full and the broken curve indicate stable and unstable states, respectively. Lamellae and hpc are denoted by lam and hpc, respectively. The black circles indicate the corresponding intensity off bcc crystals obtained by numerical simulations: (b) the bcc optical crystal in real space and (c) its Fourier transform in (k_x, k_y, k_τ) space obtained for $\delta = 0.7$ and $E_i = 0.098$. Reprinted from Chaos, Solitons Fractals **152**, Tlidi *et al.*, "Optical crystals and light-bullets in Kerr resonators," 111364, copyright 2021, with permission from Elsevier [204].

A number of tools have been developed to characterize and to classify the complexity of the observed patterns such as power spectra, filtering spatiotemporal diagrams, embedding dimensions, or using a time series analysis. Details of these tools can be found in Refs. [209–212]. An interesting question is how to characterize the complexity of the observed intracavity field structure, and how to distinguish between various complex behaviors such as spatiotemporal chaos, low-dimensional chaos, and turbulence. The only reliable tool for the characterization of these complexities is the Lyapunov spectrum. Classification of these complex regimes based on the Lyapunov spectrum is shown in Refs. [213–216]. Lyapunov exponents measure the sensitivity of the system to initial conditions. If the Lyapunov spectrum possesses a continuous set of positive eigenvalues, the complex behavior belongs to the class of spatiotemporal chaos. In the case of low-dimensional chaos, the Lyapunov spectrum possesses rather a discrete set of positive eigenvalues. Finally, turbulence or weak turbulence in system dynamics are characterized by a power-law cascade, such as the celebrated Kolmogorov scaling law [216].

Figure 12

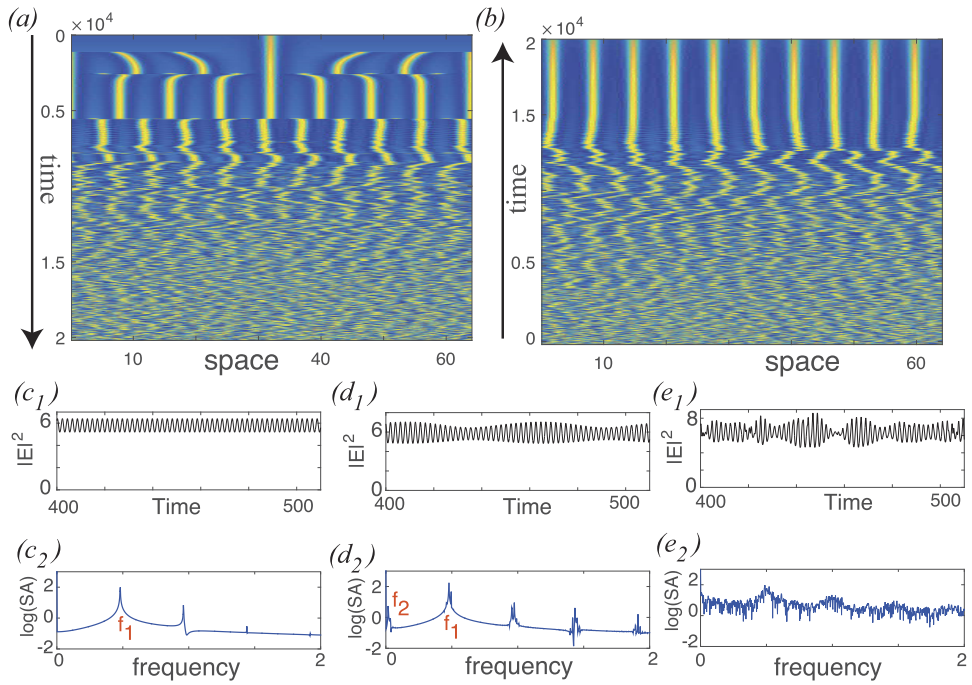

Space–time maps obtained from numerical simulation of Eq. (43) showing the evolution of the intracavity field intensity. (a) Along the z direction E_i is increased from 1.3 to 3.3. (b) Here E_i is decreased from 3.3 to 1.3. (c1), (d1), and (e1) Time traces for an isolated peak in the intracavity structure for $E_i = 1.85$, 1.9, and 2.1, respectively. (c2), (d2), and (e2) Corresponding power spectra. Reprinted by permission from Macmillan Publishers Ltd: Panajotov *et al.*, Eur. Phys. J. D **71**, 176 (2017) [213]. Copyright 2017.

Numerical simulations of Eq. (43) indicate that the complexity in the intracavity field structure belong to spatiotemporal chaos type of behavior [165,213,217]. Indeed, the Lyapunov spectrum formed by a continuous set of positive exponents are plotted in Fig. 13. These exponents are denoted by λ_i, where $i = 0, 1, \ldots, N$ with N being the grid number. For $p>q$, $\lambda_p \leq \lambda_q$. The optical cavity, which is composed of N cells, exhibits a complex behavior seeded by a random initial condition as shown in the space–time map of Fig. 13(a). The corresponding Lyapunov spectrum is plotted in Fig. 13(b), which constitutes the only reliable tool to characterize the spatiotemporal chaotic regime. In addition, we compute the Yorke–Kaplan dimension (D_{YK}) introduced by Ott [218]

$$D_{KY} \equiv p + \frac{\sum_{i=0}^{p} \lambda_i}{\lambda_{p+1}}, \tag{49}$$

where p is the largest integer exponent satisfying the condition $\sum_{i=0}^{p} \lambda_i > 0$. The Yorke–Kaplan dimension D_{YK} scales with the size of the system as shown in Fig. 13(b). It is an extensive quantity, which increases linearly with the size of the system [215]. The Yorke–Kaplan dimension provides a measure of the strange attractor complexity. An attractor is called strange if it has a non-integer dimension. In spatially extended systems although the phase space is an infinite-dimensional function space, the universal attractor has a finite fractal dimension [219]. In addition, chaotic fluctuations possess a finite correction length and computing correlations of such chaotic fluctuations is not an easy task and requires the use of a parallel computer [220–222].

Figure 13

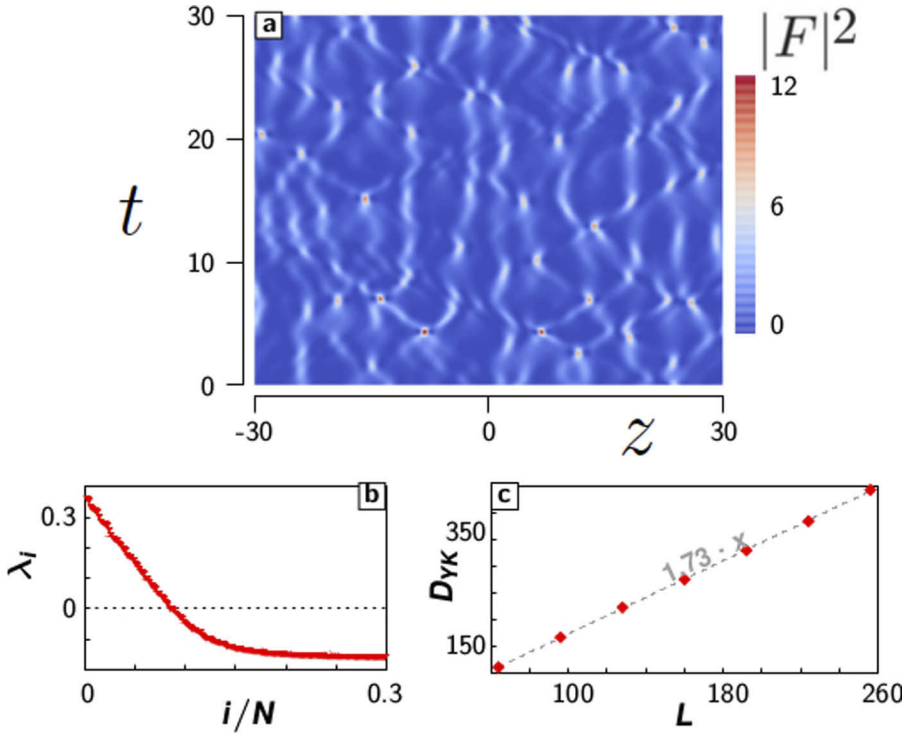

Characterization of spatiotemporal chaos in the LLE with losses α which are not normalized to unity using numerical simulations [213]: (a) space–time map; (b) Lyapunov spectrum; (c) the Yorke–Kaplan dimension as a function of the system size. The linear growth of D_{YK} dimension is fitted by a slope of 1.73 as shown by a dashed gray line. Parameter settings: $\alpha = 0.16$, $\Delta = 1$, and $E_i = 0.16$. Reprinted with permission from [217]. Copyright 2017 Optical Society of America.

4.5. Dissipative Rogue Waves in Kerr Resonators

In addition to the above-mentioned complex behavior in the form of spatiotemporal chaos, theoretical and experimental studies have shown the possibility to generate rogue waves in all-fiber resonators. Their formation is attributed in most cases to the MI. In these dissipative systems, small-amplitude pulses may grow to large amplitudes if their frequencies fall in the band of unstable modes with a positive gain. Evidence of rogue waves formation in the framework of LLE has recently been provided in the 1D setting in the absence of delayed feedback [213,223,224] and in the presence of time-delayed feedback [23,26,75].

Recently, experimental observations of rogue waves in a coherently driven all-fiber cavity have motivated further interest in the field of optics and photonics [224]. A schematic setup is shown in Fig. 14(a). In this experiment, an all-fiber ring cavity of length 26.5 mm long is used to generate ORWs. The temporal and spectral characteristics of the intracavity field are measured using an intensity autocorrelator with a resolution of 10 fs at a resolution of 2.5 GHz for the optical spectrum analyzer. The light field circulating in the fiber ring cavity indicated by the yellow box of Fig. 14(a) suffers dispersion and nonlinearity. The nonlinear resonator depicted in Fig. 14(a) constitutes an ideal testbed for the experimental study of rogue wave formation in systems subject to a permanent pumping of energy. In addition, when taking into account injection and dissipation, this part of the setup can be described by the temporal and spatial LLE (43). We refer the reader to Ref. [224] for a detailed description of the experimental arrangement. Numerical simulations of this equation indicate that when

Figure 14

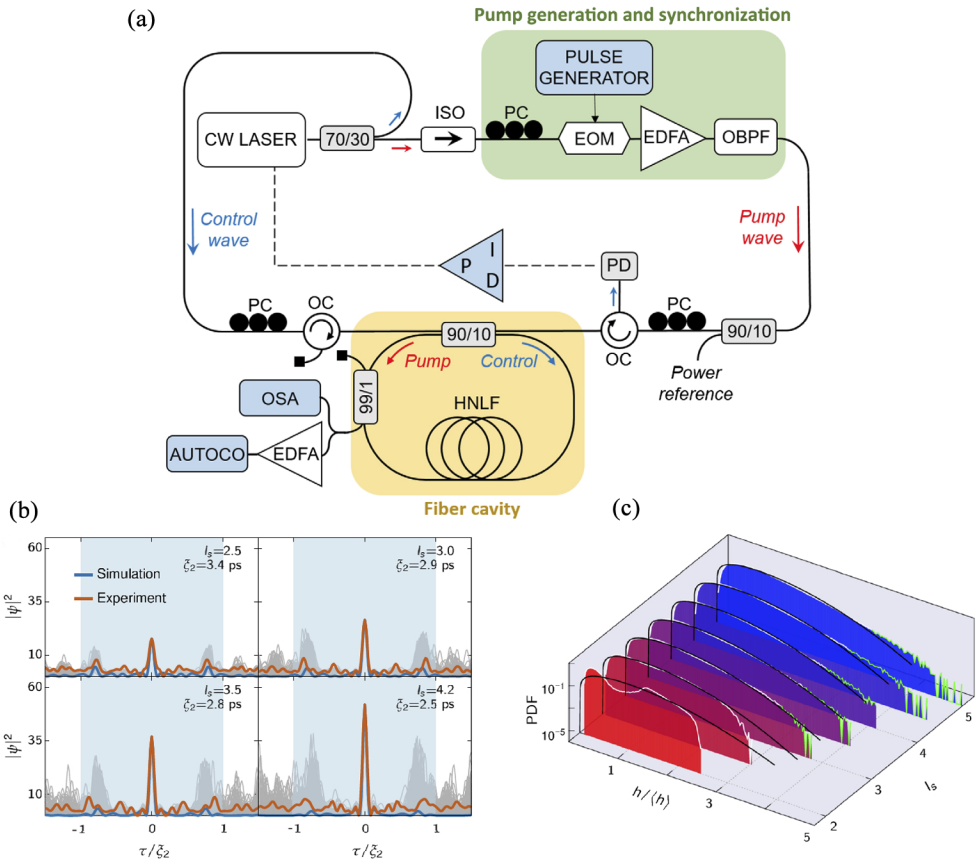

(a) Schematic sketch of an optical fiber cavity modeled by the LLE. (b) Intensities of the optical pulses from experimental observations and numerical simulations showing rogue events. (c) Logarithmic scaled probability density functions of spatiotemporal pulses as a function of the injected power showing the long tail distribution. Reprinted under a Creative Commons 4.0 license [224].

increasing the pump power E_i, the temporal profile of the intracavity field exhibits complex behavior. In particular, the optical pulses exhibit "spiking" and "bursting" types of behavior. This feature is shown in Fig. 14(b) taken from Ref. [224]. From this figure, we can see that the highest peak intensity pulses are surrounded by smaller ones located at a position ζ_2 which is often called the correlation length. Mathematically, this length is defined as the exponential decay of the equal time two-point correlation:

$$C(\delta_z) = \langle \big(F(\delta_z + z') - \langle F\rangle\big)[F(z') - \langle F\rangle]\rangle, \tag{50}$$

where the brackets $\langle . \rangle$ denote averaging along the longitudinal coordinate z. The probability density distribution of the associated peak heights as a function of the injected power E_i is shown in Fig. 14(c). The temporal profiles of the intensity that burst in a spatiotemporal complex regime are accurately estimated using the correlation function as can be seen in Fig. 14(b). These extreme events are quantified by the corresponding probability distribution function shown in Fig. 14(c). The green line indicates peaks that are twice as large as the background intensity, and the black lines denote the Rayleigh distribution with a unity mean value.

Figure 15

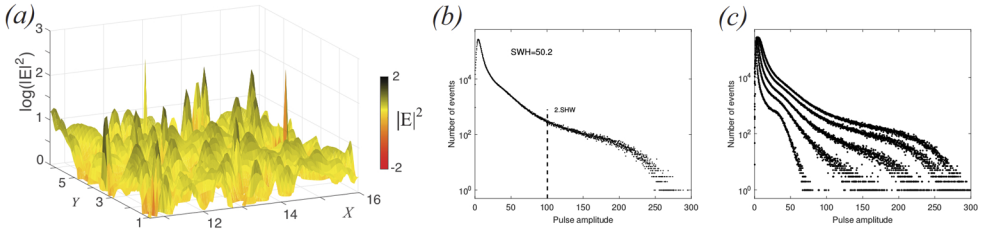

2D dissipative rogue event in Kerr resonators. (a) Intensity profile of the intracavity field in logarithmic scale. (b) Probability distribution function (PDF) of the pulse amplitudes indicating extreme events with pulse amplitude larger than twice the SWH. Parameter settings: $E_i = 5, \theta = 2$. (c) As in (b) with the injected field E_i varied between 1.5 and 7. Reprinted by permission from Macmillan Publishers Ltd: Panajotov *et al.*, Eur. Phys. J. D **71**, 176 (2017) [213]. Copyright 2017.

In 2D settings, stationary 2D LSs become unstable when increasing the intensity of the injected field. In this regime, the system can exhibit spatiotemporal chaos via period-doubling or quasiperiodicity. This transition is similar to that discussed in the 1D setting in Sec. 4.4. Such high-intensity regimes are characterized by the appearance of rogue waves. An example of such behavior in 2D settings is shown in Fig. 15(a) where an extreme event is captured. A statistical analysis documenting the number of events as a function of pulse amplitude is shown in Fig. 15(b). There exists a considerable number of events with spatiotemporal maxima of intracavity intensity more than twice the SWH, and even events with amplitude as high as six times the SWH appear. The non-Gaussian statistics of the wave intensity, with a long tail of the probability distribution, reveal the typical signature of rogue wave formation. Figure 15(c) shows the variation in the number of events when the injected field F_i is further increased.

Large-intensity pulses generated in Fig. 15 belong to the class of rogue waves or extreme events. We would like to emphasize that rogue waves are only formed in the LLE model when the spatiotemporal chaos is well developed, i.e., when the neighboring pulses in the oscillating pattern are interacting strongly. For example, Fig. 15 displays the statistics of pulse heights in the quasiperiodic and chaotic regimes discussed in the previous section for the 1D LLE model. Even when the peak amplitude of the pulses display chaotic dynamics, as in the case of $E_i = 2.1$ [Fig. 15(c)], no rogue waves are formed in the system. This is reflected in the tail of the pulse height distribution which stays below the threshold of twice the SWH. Note that the first experimental evidence of 2D rogue waves in nonlinear optics has been realized using a nonlinear optical cavity, formed by a unidirectional ring oscillator with a liquid crystal light valve [225,226].

5. DISSIPATIVE ROGUE WAVES IN CAVITY SEMICONDUCTOR

We consider the mean-field model describing the space–time evolution of broad-area VCSEL with saturable absorption [227]. We first describe experimental evidence of extreme events in 1D setting without injected field and delayed feedback. Then we investigate the control of rogue waves in two dimensions by taking into account the combined influence of optical injection and delay feedback. The advantage of implementing delayed feedback in optical resonators is that it allows for the reduction of the threshold associated with MI, self-pulsating cavity solitons, and rogue wave generation.

5.1. Model Equations for Cavity Semiconductors

The modeling of temporal–spatial dynamics in semiconductor broad-area lasers is complicated, requiring extensive knowledge of semiconductor physics, laser dynamics, and numerical methods. Many of these techniques have been already developed and used in both small and broad-area VCSEL nonlinear dynamics. In particular, the complicated microscopic physics of semiconductor materials imposes to include all the physically relevant variables, including those having a slow dynamic such as the crystal or carriers lifetime. Therefore, the radiation–matter interaction dynamics cannot be described only by the electric field alone as in the case of the Kerr media. To simplify further, we assume that only the coupling of the electric field with the excitonic resonance is considered in that model. This means that the continuous absorption band that alters the high-frequency side of the excitonic line in the absorption spectrum of the semiconductor material is neglected.

To model the cavity semiconductor, we use the slowly varying approximation and we assume a paraxial approximation of the coupled Maxwell–Bloch equations. We assume the validity of the mean-field approximation which requires high-finesse cavity or high-Q-factor resonators such that the semiconductor cavity operates on a single longitudinal mode. We neglect the field polarization degrees of freedom by assuming that the coupled Maxwell–Bloch equations are scalar. To control the 2D rogue waves by time-delayed optical feedback, we modify the model from Ref. [227] by adding delayed optical feedback from a distant mirror in a self-imaging configuration, i.e., light diffraction in the external cavity is compensated for [228,229]:

$$\partial_t E = \left[(1-i\alpha)N + (1-i\beta)n - 1 + i\nabla_\perp^2\right]E + \eta e^{i\phi}E(t-\tau), \tag{51}$$

$$\partial_t N = \gamma_1\left[\mu - N\left(1+|E|^2\right)\right], \tag{52}$$

$$\partial_t n = -\gamma_2\left[\gamma + n\left(1+s|E|^2\right)\right], \tag{53}$$

where E is the slowly varying electric field envelope, N (n) is related to the carrier density, α (β) is the linewidth enhancement factor, and γ_1 (γ_2) is the ratio of photon lifetime to the carrier lifetime in the active layer (SA) (normalization is the same as in Ref. [227]). Here μ is the normalized injection current in the active material, γ measures absorption in the passive material, and $s = a_2\gamma_1/(a_1\gamma_2)$ is the saturation parameter with $a_{1(2)}$ the differential gain of the active (absorptive) material. The diffraction is described by the Laplace operator $\nabla_\perp^2$ acting on the transverse plane (x, y) and carrier diffusion is neglected. Time and space are scaled to the photon lifetime τ_p and diffraction length, respectively.

We are interested in investigating the effect of the time delayed feedback control (TDFC) schemes on the space–time dynamics of the cavity semiconductor. TDFC is based on the use of the difference between systems variables at the current moment of time and their values at some time in the past. The delay feedback is modeled by adding an external mirror located at a distance L_{ext} from the output facet of the VCSEL. The diffraction in the external cavity is fully compensated, and the feedback field is sufficiently attenuated so that it can be modeled by a single delay term with a spatially homogeneous coefficient $\eta e^{i\phi}E(t-\tau)$. The modeling of the delayed feedback has been introduced in an earlier report by Rosanov [230] in solid-state lasers and Lang–Kobayashi in semiconductor lasers [231]. The delay feedback is characterized by the time delay τ, the feedback strength η, and phase ϕ.

In a 2D setting, despite significant theoretical advances made in cavity semiconductor devices regarding the formation of rogue waves, there are still some important remaining issues, such as their experimental evidence are still lagging. To some extent,

this is because only recently wide-aperture VCSEL technology has attained maturity [232,233]. The first experimental demonstration of LSs in optically pumped semiconductor microresonators was carried out in 2001 [234] and in electrically pumped VCSELs in 2004 [235]. Their properties were studied in 2004 [236]. The possibility to obtain LSs above the lasing threshold was demonstrated in 2006 [237]. Experimental observation of LSs in medium-size VCSELs has been reported [238] as well as their polarization properties [239]. Alternatively, LSs can be realized without holding beam in a laser containing a SA or subject to frequency-selective feedback. The SA scheme was considered theoretically as early as 1992 [240] and realized experimentally in 1997 [241]. Only recently such LSs have been experimentally demonstrated in broad-area VCSELs in Ref. [242], and Ref. [243] for SA systems and frequency selective feedback. However, the monolithic semiconductor laser–SA system has only been realized by optical pumping [244]. When the interaction of several field components of different frequencies or polarizations is considered, vector LSs are predicted theoretically for a dichroic Kerr cavity [245]. Due to the surface emission, the weak cavity anisotropies, and the spin-flip mechanism, VCSELs emit linearly polarized light that may switch between two orthogonal directions [245]. A single orthogonally polarized LS with 44 μm diameter has been demonstrated experimentally [246]. Control of LSs by periodic forcing in space or time ("rocking") was suggested in Refs. [247–249]. The inclusion of delayed feedback in the modeling of VCSELs with saturable absorption has been investigated recently. It has been shown that the delay-induced motion of dissipative solitons can be predicted to appear in nonlinear [250], and laser [251] systems. Recent studies on VCSELs [252–254] showed that the phase of the delayed feedback and the carrier decay rate strongly affect the parameter region where LSs experience a drift.

5.2. Experimental Evidence of Dissipative Rogue Waves in a Cavity Semiconductor

The observation of rogue wave formation in Kerr optical fiber has spurred interest in other laser configurations such as semiconductor resonators. In particular, spatiotemporal chaos and extreme events have been demonstrated in an extended planar microcavity laser with a SA [24]. In small-area semiconductor lasers, where the diffraction is neglected, there exist narrow parameter regions where the laser intensity exhibits high-intensity pulses in the time domain [255–257]. When the delay feedback is taken into account temporal rogue waves have also been generated in a semiconductor laser with a short external cavity [258].

In what follows, we consider a 1D problem where the diffraction term is given in Eqs. (51)–(53). In addition, we do not consider the delayed feedback and optical injection. The above-mentioned experimental observations of extreme events were conducted in a microcavity laser which possesses a VCSEL with intracavity SA [24,259]. It consists of two multilayer mirrors for optimized optical pumping and an active zone with two InGaAs quantum wells for the gain section and one InGaAs quantum well for the SA section. The cavity has a large Fresnel number and is pumped along a rectangular aperture. The dynamics are recorded at the same time at two different spatial points. The spatial coupling mediated by diffraction together with light–matter interaction, and dissipation are at the origin of spatiotemporal complexity observed in this system [24,260]. In particular, the transition from regular self-pulsating pulses to a very irregular one has been observed [24]. It has been shown that this simple device undergoes spatiotemporal chaos. This behavior is similar to that observed in Kerr resonators (see Sec. 4.4).

The recorded time traces allow one to obtain a histogram of the intensity heights. This statistical analysis together with the estimation of the SWH that is larger than two, indeed indicates the evidence of extreme events as shown in Fig. 16. This figure shows

Figure 16

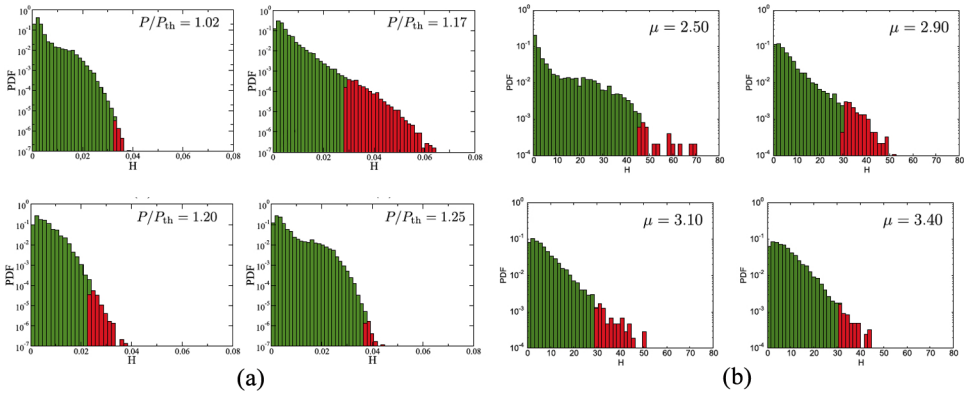

Histogram of the intensity heights as a function of the pump intensity obtained (a) from experimental data and (b) from numerical simulation obtained for the parameters $\alpha_1 =$, $\beta = 0$, $\gamma_1 = \gamma_2 = 0.005$, $\gamma = 0.5$, $s = 10$, and $\eta = 0$. Figures 2 and 3 reprinted with permission from Selmi *et al.*, Phys. Rev. Lett. **116**, 013901 (2016) [24]. Copyright 2016 by the American Physical Society.

histograms of the intensity heights as a function of the injected field intensity obtained experimentally and numerically. Numerical simulations are performed by neglecting the diffusion of the carriers, the optical injection field, and delayed feedback. Time has been rescaled to the field lifetime in the cavity, which is calculated to be of the order of 8.0 ps. Thanks to this short time scale, large recordings and accurate statistics can easily be extracted from the output of this simple device. Space is rescaled to the diffraction length which is of the order 7.4 μm. The numerical simulations of the model given in Eqs. (51)–(53) have been realized by using periodic boundary conditions. In the experiments, as the normalized pump power P/P_0 is increased, the histograms of the intensity heights develop long tails.

6. CONTROL OF ROGUE WAVES BY DELAYED FEEDBACK

Delayed feedback can be used to control the formation of 2D rogue waves in the Kerr cavity [23,26,213]. In this section, we consider the formation of rogue waves in a broad-area surface-emitting laser with a SA and with the delay feedback [see Fig. 17(a)]. It has been shown that when applying time-delayed feedback a single 2D dissipative soliton exhibits a period-doubling bifurcation to spatially localized chaos [228]. In 2D settings, it has been numerically predicted that a broad-area surface-emitting laser with a SA is capable of generating 2D spatial rogue waves either by strong pumping [25] or by optical feedback [26,213]. Note that, in small-area VCSELs, optical feedback induces rogue waves as in small-area semiconductor lasers in the short-cavity configuration. In this case, the round trip time in the external cavity is shorter than the laser relaxation oscillation period.

We consider the parameter range where the VCSEL with saturable absorption exhibits a bistable behavior between the zero homogeneous solution ($E = 0$, $N = \mu$, $n = -\gamma$) and the lasing solution ($E = \sqrt{I}e^{iwt}$, $N = \mu/(1 + I)$, $n = -\gamma/(1 + sI)$). In addition, we set parameters such that the upper lasing solutions exhibit a subcritical MI allowing for the formation of stable dissipative solitons [228]. By increasing the strength of the delay feedback, the output undergoes a period-doubling bifurcation to spatially localized chaos [228].

Figure 17

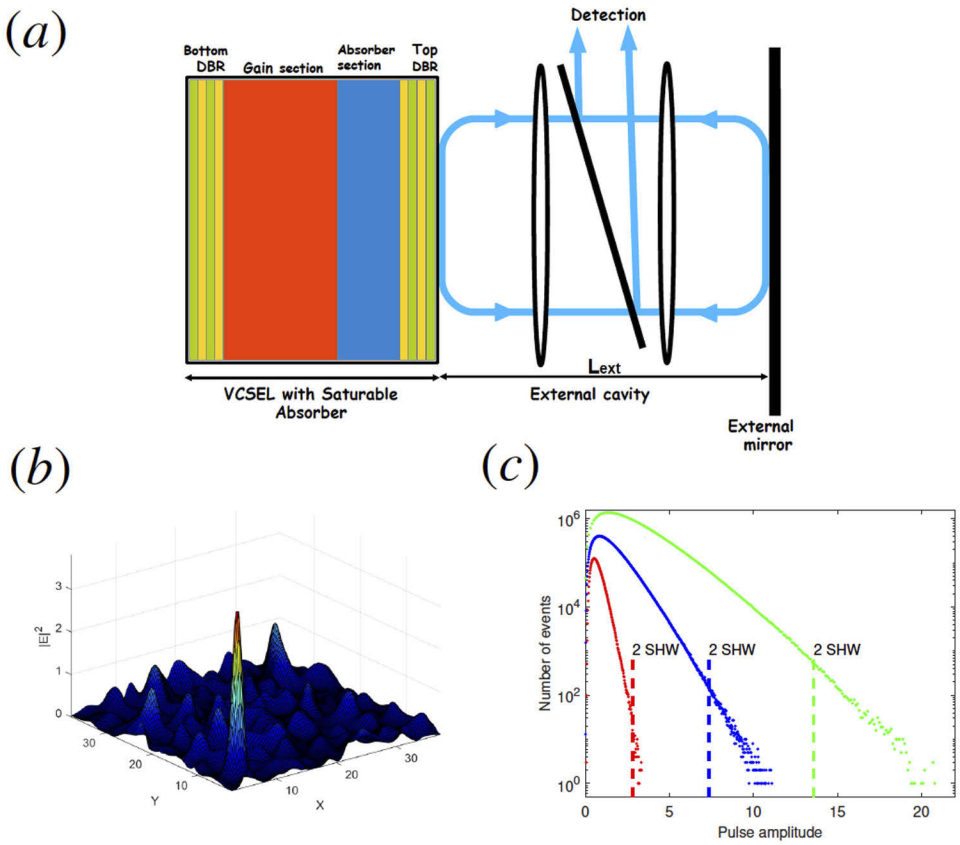

Broad-area surface-emitting laser with a SA and optical delayed feedback. (a) A schematic sketch of the VCSEL with delayed feedback. (b) 2D rogue waves in the transverse plane (x, y). (c) Statistical distributions of pulse height as a function of the delay feedback strength. We vary the strength of the delayed feedback η. The red curve is obtained for $\eta = 0.1$, blue for $\eta = 0.3$, and green for $\eta = 0.5$. (b) and (c) Reprinted with permission from Panajotov *et al.*, Chaos **30**, 053103 (2020). [43]. Copyright 2020, AIP Publishing LLC.

Figure 17(b) shows an example of complex 2D spatiotemporal type of behavior obtained by numerical integration of Eqs. (51)–(53) with periodic boundary conditions. The parameter settings are $\alpha = 2$, $\beta = 0$, $b_1 = 0.04$, $b_2 = 0.02$, $\gamma = 0.5$, $s = 10$, $\mu = 0.3$, and optical feedback with a time-delay of $\tau = 100$ and phase $\phi = 0$. The time-delayed feedback parameters are: $\tau = 50$, $\eta = 0.1$, and $\phi = 0$. Statistical distributions of pulse height in Fig. 17(c) show a non-Gaussian statistics with a long tail or L-shape indicating the occurrence of extreme or rare events in 2D settings. To control rogue waves, we fix all the parameters and we vary the strength of the delay feedback. When increasing the feedback strength, the histogram evolves toward an L-shape distribution with a long tail.

7. 3D ROGUE WAVES

7.1. Acoustic Rogue Waves

In this section, we summarize recent studies on 3D rogue waves. The first experimental observation of rogue waves in 3D settings has been reported in Ref. [261] where the authors showed the existence of acoustic rogue waves in dusty plasmas [261,262]. Specifically, they addressed the problem of rogue wave formation as a result of wave–particle interactions by correlating rogue wave event and low-amplitude

Figure 18

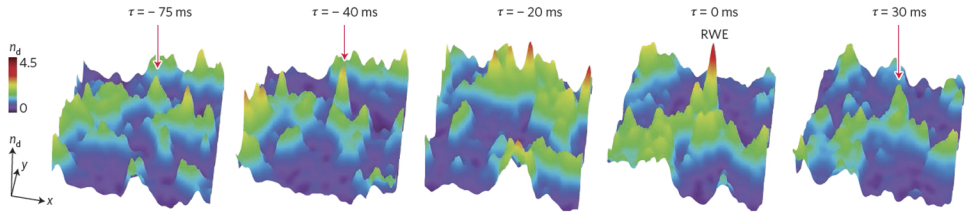

3D rogue waves. The spatial distribution of the normalized dust intensity at various time instants along a horizontal slice in the *xy* plane with the dust acoustic wave propagating in the vertical *z* direction. The peak wave amplitude is indicated by red arrows clearly depicting that the individual wavefronts travel at different speeds thereby causing an irregular spacing where maximum amplitudes are observed. The rogue wave event arises due to particle focusing near regions which are the low-amplitude holes, which triggers the rapid growth of the wave amplitude and the emergence of a rogue wave in a very short period of time, of the order of 10 ms. Reprinted by permission from Macmillan Publishers Ltd: Williams, Nat. Phys. **12**, 529–530 (2016) [262]. Copyright 2016.

hole filaments with their surrounding 3D waveforms and particle motion. Their study focuses on dust acoustic waves which are fundamental nonlinear acoustic-type density waves governed by modulation-type nonlinear dynamical equations. They are associated with the low-frequency longitudinal oscillation of negatively charged dust particles in gaseous plasmas.

A dusty plasma consists of ions, electrons, and neutral particles with the addition of small particulate matter, which is the "dust" [262]. The dust can be any type of small particulate matter which is present in the plasma medium (carbon, pollen, or manufacture spheres of silica). In the study described in Ref. [261], polystyrene particles of 5 μm were used. The dust in the plasma environment interacts with the surroundings, and thereby acquiring a net charge of its own, thereby resulting in a more complex system. The size of the dust present in the plasma environment plays a pivotal role as it determines the net charge acquired by the dust. The interaction between the dust and plasma surroundings can be tuned by adjusting the background properties of the plasma. In the study described in Ref. [261], they could track this interaction by performing a direct video imaging of large-area dust density evolution, and by tracking individual particle motion. This allows one to construct an Eulerian–Lagrangian picture, thereby enabling a direct experimental observation of 3D rogue wave event, which are both localized in space and time.

In the experiment of Ref. [261] the dust acoustic wave mode was created by passing a sinusoidally varying current through a gas at low pressure. An ion-streaming instability results in the downward propagation of a naturally occurring dust acoustic wave, which appears as a modulation in the background dust intensity. This is illustrated in Fig. 18. The interaction of the dust particles with the background plasma results in regions where particles accumulate, and regions where there is particle depletion as it propagates [262]. The 3D perspective of this phenomenon is shown in Fig. 19(a) in the *xt* and *yt* planes. The rogue wave event, which is localized in both space and time, is indicated by an arrow. The low amplitude holes (defects) are indicated using crosses, the trajectories of which are shown in Fig. 19(b). It is interesting to note that the rogue wave events are surrounded by low amplitude filament holes, which indicates the role of dust particle interaction with the background plasma in the formation of dust acoustic rogue waves.

Figure 19

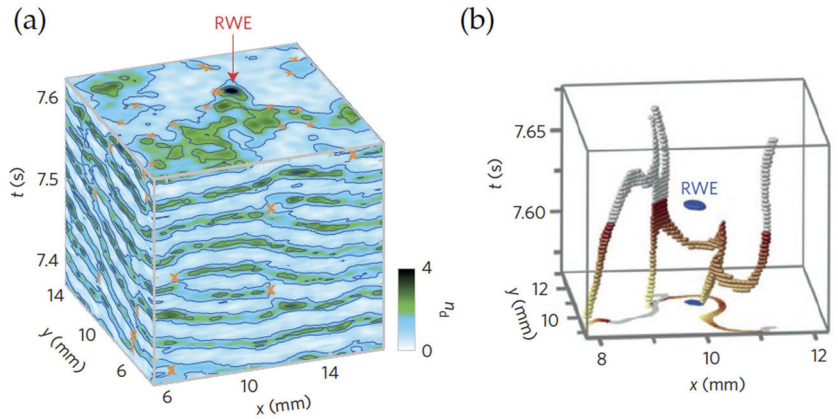

(a) Distribution of the normalized dust intensity in the *xt* and *yt* planes showing the typical undulated waveform. The arrows indicate the position of a rogue wave event (RWE), which is localized on the top *xy* plane. The locations of the low-amplitude holes are indicated by crosses, which are regions where wave amplitudes are null and phases are undefined. (b) Irregular hole filaments surrounding rogue wave event in the *xyt* space, with their projections on the floor. Reprinted by permission from Macmillan Publishers Ltd: Tsai *et al.*, Nat. Phys. **12**, 573–577 (2016) [261]. Copyright 2016.

7.2. 3D ORWs

In nonlinear optics and photonics, most of the study of rogue waves is limited to 1D or 2D settings. Experimental evidence of 3D structures in Kerr media is still missing in the literature. However, 2D [72] and 3D rogue waves have been observed in optical systems devoid of any nonlinearity [263]. They appear in the speckle distribution of a spatially modulated optical beam that generates inhomogeneity in the system. They have been also observed in microwave experiments where the transport of waves is realized through an arrangement of randomly distributed scatterers [264]. This work applies the microwave techniques to obtain information on the transport of waves in a 2D disordered media. Large deviations from Rayleigh's law for the distribution of the wave height are observed at lower frequency. In spatial locations, the system developed so-called "hot spots" whose intensity is much higher than expected in a random wave field.

The scarcity of 3D study in nonlinear Kerr media is because in the course of propagation, a single or more light-bullets suffers beam collapse in the case of the NLSE when the dimensionality of the system is larger than one [59]. To avoid beam collapse, a saturable nonlinearity [265] or an optical cavity [144,266,267] are used to stabilize the light-bullet. When taking into account 2D diffraction and 1D dispersion, 3D dissipative structures can be formed in an optical cavity. They consist of self-organized light-bullets traveling within the cavity at the group velocity of the light [62]. Note, however, that stable light-bullets were first predicted in a frequency conversion material [268–273] because quadratic nonlinearity does not provoke collapse in two and more dimensions [274]. In contrast to conservative a Kerr medium where the emergence of light-bullets suffers beam collapse, here the balance between pumping and dissipation allows for their stabilization [62,145]. They have been predicted in cavity nonlinear optics such as optical parametric oscillators [266,275], type II second-harmonic generation [203,276], and wide aperture lasers with a SA [277,278], semiconductor [279,280], in an inhomogeneous array of carbon nanotubes [281], or twisted waveguide arrays [282]. Furthermore, 3D structures in nonlinear resonators have also been predicted from models going beyond the mean-field approximation

[283,284]. The formation of light-bullets in nonlinear optics is a well-documented issue (see overviews in Refs. [41,285–287]).

Finally, we discuss recent developments in the formation of light-bullets and 3D rogue waves in Kerr cavities. We have shown in Sec. 4.3 that close to the 3D MI, the output field presents a 3D periodic distribution of light-bullets with a well-defined frequency (in the temporal regime) or wavelength in the spatial domain. The weakly nonlinear analysis allows for the construction of different branches of 3D structures. This analysis is valid in the range of the detuning parameter where $\delta<41/33$. In the strongly nonlinear regime where the MI appears subcritical, i.e., $\delta>41/30$, there exists a so-called pinning zone of parameters in which stable light-bullets can be generated. In this regime, spatial and temporal confinement of light is possible [62]. A single, as well as bounded light-bullets, are generated numerically as shown in Fig. 20(a)–20(f). They are stationary solutions of the 3D LLE (43) in the reference frame moving with the group velocity of the light within the cavity. The number and the positions of light-bullets in the Euclidian space (x, y, τ) depend on the seeded initial condition. As the amplitudes of light-bullets having different numbers of peaks are close to one another it is convenient to plot the dimensionless "L_2 norm,"

$$\mathcal{N} = \int |E - E_s|^2 \, dx \, dy \, d\tau,$$

as a function of the strength of the injected field amplitude. The results are shown in the 3D bifurcation diagram of Fig. 20(g). Plotting $\mathcal{N}$ instead of the intracavity field intensity allows for better visualization of the clustering property of light-bullets. In the pinning range of parameter settings denoted by P where light-bullets are stable, the system undergoes a high degree of multistability: in addition to the bcc crystal, and the homogeneous background which are both stable, an additional stationary close-packed light-bullets can be generated. We plot only clusters involving up to six light-bullets as shown in Fig. 20(a)–20(f). The cross section of the single light-bullet along the transverse plane is shown in Fig. 20(i). This figure shows a damping and decaying oscillatory tail of the light-bullet. This is an important property of dissipative solitons setting a non-zero background. Finally, under a radial approximation where the Laplace operator can be reduced to $\nabla_\perp^2 + \partial^2/\partial\tau^2 = \partial^2/\partial r^2 + (2/r)\partial/\partial r$ where $r = (x^2 + y^2 + \tau^2)^{1/2}$. The stationary solution of a single light-bullet is plotted together with that obtained by direct numerical simulations of the 3D LLE (43) and the comparison shows a good agreement.

The 3D bifurcation diagram of Fig. 20(g) suggests that light-bullets formation belong to the class of the well-known homoclinic snaking type of bifurcation [288–292]. The bifurcation diagram is established by continuation methods and its consists of two snaking curves; one describes LSs with an odd number of peaks and the other corresponds to an even number of peaks. As one moves further along the snaking curve, the LS becomes better localized and acquires stability at the turning point where the slope becomes infinite. Afterward, the LS begins to grow in spatial extent by adding extra peaks symmetrically at either side. This growth is associated with back and forth oscillations across the pinning interval where the system develops multistability [see region C in Fig. 20(g)]. This type of bifurcation is well understood in the 1D setting (see overviews of this issue in Refs. [293–296]).

When increasing the strength of the injected beam further, we observe the transition from stationary light-bullets to complex 3D structures. In this large-intensity regime, the cavity field presents an emission of extreme waves. Indeed, statistical analysis of pulse height distribution of this spatiotemporal complex regime in the 3D LLE is summarized in Fig. 21. The long-tailed statistical contribution is a signature of the

Figure 20

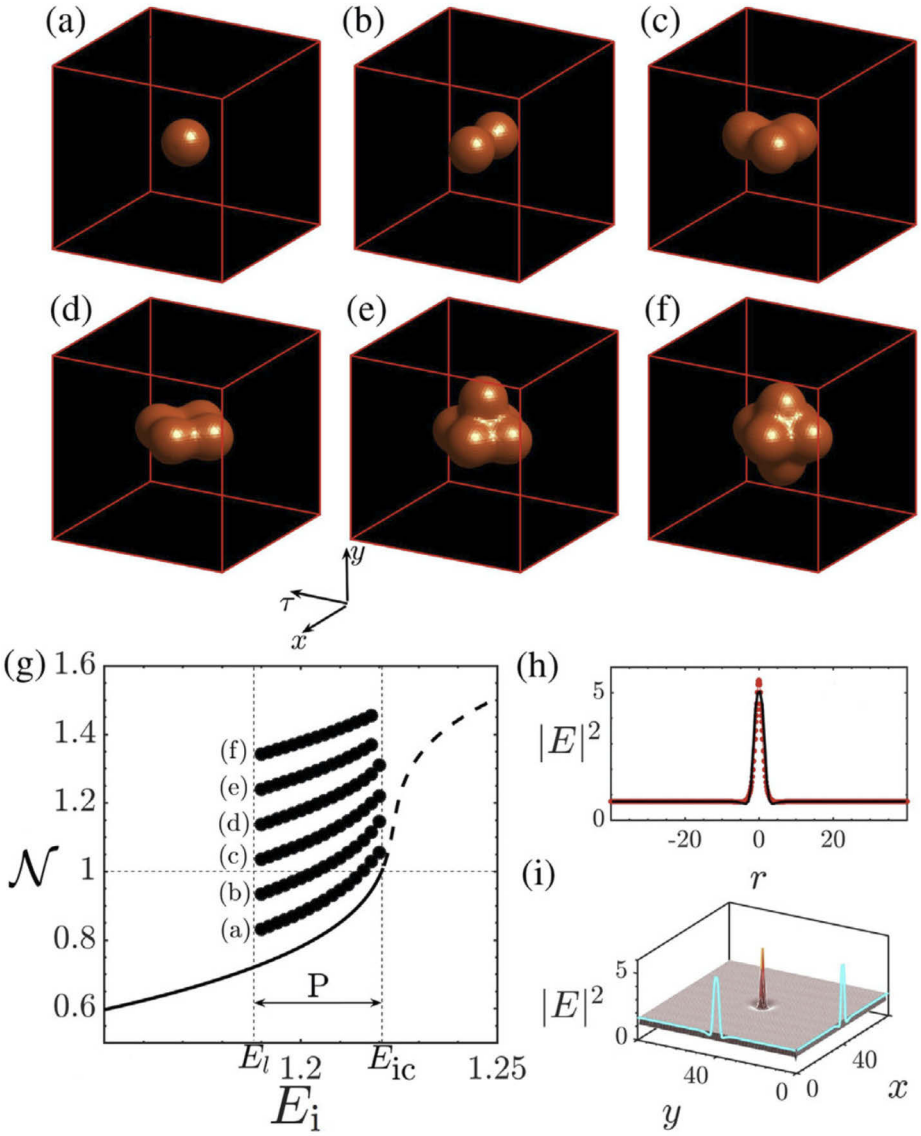

(a)–(f) 3D isosurface of dissipative light-bullets and clusters of them in a Kerr resonator involving up to six 3D peaks. (g) 3D bifurcation diagram obtained for $\delta = 1.7$. (h) Comparison between the LB obtained by a spherical symmetry (red dotted line) and the cross section along 1D direction represented by a continuous black line. (i) Cross section along the transverse plane of the single LB. Parameters are $\delta = 1.7$ and $E_i = 1.21$. Figure 2 reprinted with permission from Gopalakrishnan *et al.*, Phys. Rev. Lett. **126**, 153902 (2021) [62]. Copyright 2021 by the American Physical Society.

presence of rogue waves. Waves with pulse heights more than twice the SWH appear in the output of the Kerr cavity.

Finally, we discuss some possible experimental parameter values relevant to the generation of light-bullet and transition to rogue waves formation. We suggest using chalcogenide glass, which is characterized by a very strong Kerr effect and a very fast response to an electrical excitation. Typical physical parameters values are as follows. The nonlinear refractive index n_2 coefficient is as high as $n_2 \approx 2.3 \times 10^{-17}\,\mathrm{m^2\ W^{-1}}$. This results in a nonlinearity coefficient of $\gamma \approx 0.144\ \mathrm{W^{-1}\ km^{-1}}$ for an effective (illuminated) area of $A_{\mathrm{eff}} = 25 \times 10^4\ \mu\mathrm{m}^2$. The length of the cavity is $l = 1000\ \mu\mathrm{m}$

Figure 21

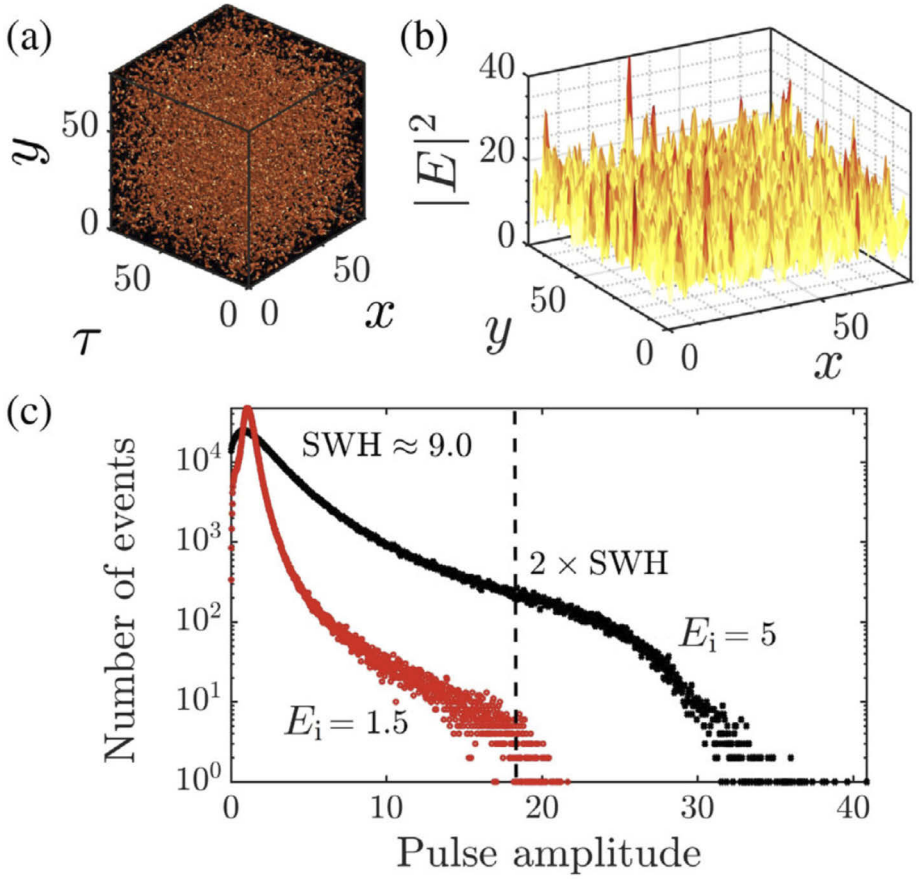

3D rogue waves in Kerr cavity. (a) Isosurface of 3D rogue waves obtained for $\delta = 1.7$ and $E_i = 5$. (b) The cross section along the transverse (x, y). (c) The number of events as a function of the intensity of the pulses in semi-logarithmic scale for two different values of E_i. The dashed line indicates events of amplitudes at twice the SWH. Figure 2 reprinted with permission from Gopalakrishnan *et al.*, Phys. Rev. Lett. **126**, 153902 (2021) [62]. Copyright 2021 by the American Physical Society.

and the reflectivity of the mirrors $1 - \theta = 0.95$, so that the optical losses are determined by the mirror transmission as the intrinsic material absorption loss can be as small as 40 dB/km. The wavelength $\lambda_0 = 4\,\mu$m is chosen close to the zero dispersion wavelength. The choice of these physical parameters are from Refs. [297,298]. The response to an excitation by an optical injection E_i, which is the amplitude of the driving field incident on the cavity input mirror M_1 with an intensity transmission coefficient θ, is $P_\mathrm{in} = |E_\mathrm{i}|^2$, which is the driving power. The intracavity power is $P = |E|^2$. These two powers are linked through the homogeneous steady states $P_\mathrm{in} = P[1 + (\delta - P)^2]$ With the above-mentioned realistic physical parameters and the dimensionless parameters for which the light-bullet exists $E_\mathrm{i} = 1.21$ and $\delta = 1.7$, the intensity of the injected field should be of the order of 10 MW cm^{-2}. This is reasonable because it is well below the damage threshold of chalcogenide, which can be as high as 1 GW cm^{-2}. The link relation between the physical parameters and the dimensionless parameters are given by the relation (42). The physical model corresponds to Eq. (41) and the adimensional model is Eq. (43). In these settings, we expect that the spatial width in (x, y) plane will be $\approx 270\ \mu$m and the temporal width of the LB will be ≈ 0.08 ps for a value of $\beta_2 \approx 20\,\mathrm{ps}^2\ \mathrm{km}^{-1}$ and about 1 ps for a value of $\beta_2 \approx 3000\,\mathrm{ps}^2\ \mathrm{km}^{-1}$.

8. CONCLUDING REMARKS

The bridge between photonics and the field of extreme events and the generation of ORWs has been established in 2007 by Solli and collaborators. They experimentally observed soliton-like pulses with ultrahigh intensities named ORWs along fibers operating in the SC generation regime. The main characteristic of these pulses is that they undergo a strong localization either in time and/or in space, and their formation is ruled by a long-tailed statistical distribution. Since this pioneering work, evidence of rogue events has been shown, thanks to several investigations in different optical systems: Kerr media, semiconductors, photorefractives, liquid crystals, and xenon gas to name a few. We have discussed some similarities between nonlinear optics and photonics regarding the formation of rogue waves.

Their dynamics are characterized by a complex irregularity due to the sensitivity to the initial conditions (chaotic or turbulent nature). These characteristics render these waves unpredictable. However, they are generated in almost all systems either linear or not, stochastic or deterministic. In spite of the accumulation of important theoretical tools describing rogue waves, still a contentious debate remains about their dynamical origin. Statistically, there is a consensus: a wave that is twice the SWH of the surrounding area can be considered as a rogue wave. However, from a dynamical system theory point of view, there remains no consensus about their origin. Recently, important progress has been realized toward a unified concept and framework for describing the formation of rogue waves not only in oceanography and hydrodynamics, but also in various fields such as optics, laser physics, and biology [299,300]. This new approach is grounded on a mathematical concept called instantons well known in quantum chromodynamics [301,302].

In the first part, we reviewed in a detailed way the derivation of the NLSE describing the propagation of wave packets in a homogeneous, cubic, centrosymmetric with Kerr material. We have used a multiple time and space scales analysis allowing one to derive this fundamental equation assuming the envelope of the wave packet to be a slowly varying function of time and space. We have discussed the most important property of this fundamental equation, namely the integrability and it is considered as the simplest model to describe light propagation in a Kerr medium such as optical fibers.

In this framework, we provided a simple theoretical description of rogue waves in terms of breathers as solutions of the NLSE, and their interaction. We have limited the discussion to the first-order basic breathers such as Akhmediev breathers, Peregrine, and Ma solitons. This allows one to understand the formation of rogue waves in the framework of conservative system where most of the theory has been developed. In addition, we have highlighted similarities between oceanic rogue waves and ORWs in a strictly 1D setting. However, we have pointed out that the analogy in 2D settings between optical and hydrodynamical systems is far from being established. In addition, we did not cover the formation of rogue waves from higher-order solutions and their interactions as soliton collision, soliton explosion, and random lasers.

In the second part, we have presented dissipative rogue waves in nonlinear optical cavities. Two systems have been considered: (i) temporal optical pulses occurring in microresonators with application to frequency comb generation; and (ii) semiconductors in relation with processing and encoding information in all-optical devices. We have shown that in all these dissipative systems rogue events are possible in 1D and 2D settings. To control such rogue events, we have discussed the role of pumping, the strength of injected field, and delayed feedback. It has been shown that delayed feedback can effectively decrease the number of rogue events in these optical cavities.

Finally, we have addressed the formation of dissipative 3D light-bullets and their transition to 3D rogue waves in Kerr optical cavities. The multiplicity of these light-bullets solutions of the LLE are strongly reminiscent of homoclinic snaking. Whether the 3D light-bullets exhibit a homoclinic snaking type of bifurcation or not remains an open question that worth to be investigating in the future. Experimentally, in nonlinear optics and photonics devices, most of the studies are limited to 1D or 2D settings. Although experimental evidence of 3D rogue waves has been realized in inhomogeneous and linear media, still there is no experimental evidence of 3D rogue waves in nonlinear media. In particular, in Kerr media, 3D studies are scarce. In this context, we have shown numerical evidence of 3D rogue waves in optical Kerr cavities and we have provided realistic parameters toward an experimental realization of light-bullets and rogue waves in Kerr optical resonators. The subject of rogue waves has evolved so much in recent years that it currently touches all branches of nonlinear science and even beyond (finance research, for instance). We are convinced that its progress will continue in the future, so fascinating and interdisciplinary this theme is.

FUNDING

Fonds De La Recherche Scientifique - FNRS; Centre National de la Recherche Scientifique — CNRS.

ACKNOWLEDGMENTS

We are grateful to S. S. Gopalakrishnan for helpful interactions on the collision and wave breaking in hydrodynamics and for editing the manuscript. We are grateful to M. G. Clerc, B. Kostet, and Y. Soupart for fruitful discussion. M. Tlidi is a Research Director at the Fonds National de la Recherche Scientifique (Belgium). Majid Taki is a full Professor at the University of Lille and member of the Centre National de la Recherche Scientifique (CNRS).

DISCLOSURES

The authors declare no conflicts of interest.

DATA AVAILABILITY

No data were generated or analyzed in the presented research.

REFERENCES

1. S. Haver, "A possible freak wave event measured at the Draupner Jacket January 1 1995," in *Rogue Waves* (World Scientific, 2004), Vol. 2004, pp. 1–8.
2. S. Haver and D. Karunakaran, "Probabilistic description of crest heights of ocean waves," Deuts. Hydrog. Zeit. (1998), doi:http://doi.org/10.1007/s10236-015-0827-9.
3. L. Draper, "Freak ocean waves," Weather **21**, 2–4 (1966).
4. C. Kharif, E. Pelinovsky, and A. Slunyaev, *Rogue Waves in the Ocean* (Springer Science & Business Media, 2008).
5. V. Ruban, Y. Kodama, M. Ruderman, J. Dudley, R. Grimshaw, P. McClintock, M. Onorato, C. Kharif, E. Pelinovsky, T. Soomere, G. Lindgren, N. Akhmediev, A. Slunyaev, D. Solli, C. Ropers, B. Jalali, F. Dias, and A. Osborne, "Rogue waves—towards a unifying concept?: Discussions and debates," Eur. Phys. J.: Spec. Top. **185**, 5–15 (2010).
6. S. Chen, F. Baronio, J. M. Soto-Crespo, P. Grelu, and D. Mihalache, "Versatile rogue waves in scalar, vector, and multidimensional nonlinear systems," J. Phys. A **50**, 463001 (2017).

7. D. R. Solli, C. Ropers, P. Koonath, and B. Jalali, "Optical rogue waves," Nature **450**, 1054–1057 (2007).
8. A. Klein, T. Yaron, E. Preter, H. Duadi, and M. Fridman, "Temporal depth imaging," Optica **4**, 502–506 (2017).
9. B. H. Kolner and M. Nazarathy, "Temporal imaging with a time lens," Opt. Lett. **14**, 630–632 (1989).
10. A. F. Runge, C. Aguergaray, N. G. Broderick, and M. Erkintalo, "Raman rogue waves in a partially mode-locked fiber laser," Opt. Lett. **39**, 319–322 (2014).
11. M. Liu, A.-P. Luo, W.-C. Xu, and Z.-C. Luo, "Dissipative rogue waves induced by soliton explosions in an ultrafast fiber laser," Opt. Lett. **41**, 3912–3915 (2016).
12. D. Solli, C. Ropers, and B. Jalali, "Active control of rogue waves for stimulated supercontinuum generation," Phys. Rev. Lett. **101**, 233902 (2008).
13. M. G. Kovalsky, A. A. Hnilo, and J. R. Tredicce, "Extreme events in the Ti:sapphire laser," Opt. Lett. **36**, 4449–4451 (2011).
14. J. Soto-Crespo, P. Grelu, and N. Akhmediev, "Dissipative rogue waves: extreme pulses generated by passively mode-locked lasers," Phys. Rev. E **84**, 016604 (2011).
15. C. Lecaplain and P. Grelu, "Rogue waves among noiselike-pulse laser emission: an experimental investigation," Phys. Rev. A **90**, 013805 (2014).
16. P. Suret, R. El Koussaifi, A. Tikan, C. Evain, S. Randoux, C. Szwaj, and S. Bielawski, "Single-shot observation of optical rogue waves in integrable turbulence using time microscopy," Nat. Commun. **7**, 13136–13138 (2016).
17. M. Närhi, B. Wetzel, C. Billet, S. Toenger, T. Sylvestre, J.-M. Merolla, R. Morandotti, F. Dias, G. Genty, and J. M. Dudley, "Real-time measurements of spontaneous breathers and rogue wave events in optical fibre modulation instability," Nat. Commun. **7**, 13675–13679 (2016).
18. B. Jalali, D. Solli, K. Goda, K. Tsia, and C. Ropers, "Real-time measurements, rare events and photon economics," Eur. Phys. J.: Spec. Top. **185**, 145–157 (2010).
19. K. Goda and B. Jalali, "Dispersive Fourier transformation for fast continuous single-shot measurements," Nat. Photonics **7**, 102–112 (2013).
20. C. Lei, B. Guo, Z. Cheng, and K. Goda, "Optical time-stretch imaging: principles and applications," Appl. Phys. Rev. **3**, 011102 (2016).
21. A. Mahjoubfar, D. V. Churkin, S. Barland, N. Broderick, S. K. Turitsyn, and B. Jalali, "Time stretch and its applications," Nat. Photonics **11**, 341–351 (2017).
22. C. Lecaplain, P. Grelu, J. Soto-Crespo, and N. Akhmediev, "Dissipative rogue waves generated by chaotic pulse bunching in a mode-locked laser," Phys. Rev. Lett. **108**, 233901 (2012).
23. N. Akhmediev, B. Kibler, F. Baronio, M. Belić, W.-P. Zhong, Y. Zhang, W. Chang, J. M. Soto-Crespo, P. Vouzas, P. Grelu, C. Lecaplain, K. Hammani, S. Rica, A. Picozzi, M. Tlidi, K. Panajotov, A. Mussot, A. Bendahmane, P. Szriftgiser, G. Genty, J. Dudley, A. Kudlinski, A. Demircan, U. Morgner, S. Amiraranashvili, C. Bree, G. Steinmeyer, C. Masoller, N. G. R. Broderick, A. F. J. Runge, M. Erkintalo, S. Residori, U. Bortolozzo, F. T. Arecchi, S. Wabnitz, C. G. Tiofack, S. Coulibaly, and M. Taki, "Roadmap on optical rogue waves and extreme events," J. Opt. **18**, 063001 (2016).
24. F. Selmi, S. Coulibaly, Z. Loghmari, I. Sagnes, G. Beaudoin, M. G. Clerc, and S. Barbay, "Spatiotemporal chaos induces extreme events in an extended microcavity laser," Phys. Rev. Lett. **116**, 013901 (2016).
25. C. Rimoldi, S. Barland, F. Prati, and G. Tissoni, "Spatiotemporal extreme events in a laser with a saturable absorber," Phys. Rev. A **95**, 023841 (2017).
26. M. Tlidi and K. Panajotov, "Two-dimensional dissipative rogue waves due to time-delayed feedback in cavity nonlinear optics," Chaos **27**, 013119 (2017).

27. H. Bailung, S. Sharma, and Y. Nakamura, "Observation of peregrine solitons in a multicomponent plasma with negative ions," Phys. Rev. Lett. **107**, 255005 (2011).
28. W. Moslem, P. Shukla, and B. Eliasson, "Surface plasma rogue waves," EPL **96**, 25002 (2011).
29. M. Tlidi, Y. Gandica, G. Sonnino, E. Averlant, and K. Panajotov, "Self-replicating spots in the Brusselator model and extreme events in the one-dimensional case with delay," Entropy **18**, 64 (2016).
30. H. N. Chan and K. W. Chow, "Numerical investigation of the dynamics of 'hot spots' as models of dissipative rogue waves," Appl. Sci. **8**, 1223 (2018).
31. S. Manzetti, "Mathematical modeling of rogue waves: a survey of recent and emerging mathematical methods and solutions," Axioms **7**, 42 (2018).
32. Y. Zhen-Ya, "Financial rogue waves," Commun. Theor. Phys. **54**, 947–949 (2010).
33. Z. Yan, "Vector financial rogue waves," Phys. Lett. A **375**, 4274–4279 (2011).
34. C. J. Gibson, A. M. Yao, and G.-L. Oppo, "Optical rogue waves in vortex turbulence," Phys. Rev. Lett. **116**, 043903 (2016).
35. J. Laurie, U. Bortolozzo, S. Nazarenko, and S. Residori, "One-dimensional optical wave turbulence: experiment and theory," Phys. Rep. **514**, 121–175 (2012).
36. M. Onorato, S. Residori, U. Bortolozzo, A. Montina, and F. Arecchi, "Rogue waves and their generating mechanisms in different physical contexts," Phys. Rep. **528**, 47–89 (2013).
37. J. M. Dudley, F. Dias, M. Erkintalo, and G. Genty, "Instabilities, breathers and rogue waves in optics," Nat. Photonics **8**, 755–764 (2014).
38. S. Wabnitz, *Nonlinear Guided Wave Optics; a Testbed for Extreme Waves* (IOP Publishing, 2017).
39. D. Mihalache, "Multidimensional localized structures in optical and matter-wave media: a topical survey of recent literature," Rom. Rep. Phys. **69**, 403 (2017).
40. J. M. Dudley, G. Genty, A. Mussot, A. Chabchoub, and F. Dias, "Rogue waves and analogies in optics and oceanography," Nat. Rev. Phys. **1**, 675–689 (2019).
41. B. A. Malomed and D. Mihalache, "Nonlinear waves in optical and matter-wave media: a topical survey of recent theoretical and experimental results," Rom. J. Phys. **64**, 106 (2019).
42. F. Copie, S. Randoux, and P. Suret, "The physics of the one-dimensional nonlinear Schrödinger equation in fiber optics: rogue waves, modulation instability and self-focusing phenomena," Rev. Phys. **5**, 100037 (2020).
43. K. Panajotov, M. Tlidi, Y. Song, and H. Zhang, "Control of dissipative rogue waves in nonlinear cavity optics: optical injection and time-delayed feedback," Chaos **30**, 053103 (2020).
44. N. Akhmediev, "Waves that appear from nowhere: complex rogue wave structures and their elementary particles," Front. Phys. **8**, 631 (2021).
45. P. Ryczkowski, M. Närhi, C. Billet, J.-M. Merolla, G. Genty, and J. M. Dudley, "Real-time full-field characterization of transient dissipative soliton dynamics in a mode-locked laser," Nat. Photonics **12**, 221–227 (2018).
46. A. Tikan, S. Bielawski, C. Szwaj, S. Randoux, and P. Suret, "Single-shot measurement of phase and amplitude by using a heterodyne time-lens system and ultrafast digital time-holography," Nat. Photonics **12**, 228–234 (2018).
47. N. Akhmediev, A. Ankiewicz, and M. Taki, "Waves that appear from nowhere and disappear without a trace," Phys. Lett. A **373**, 675–678 (2009).
48. A. Osborne, *Nonlinear Ocean Waves and the Inverse Scattering Transform*, Vol. **97** of the International Geophysics Series (Academic, 2010).
49. K. B. Dysthe and K. Trulsen, "Note on breather type solutions of the NLS as models for freak-waves," Phys. Scr. **T82**, 48 (1999).

50. V. I. Shrira and V. V. Geogjaev, "What makes the Peregrine soliton so special as a prototype of freak waves?" J. Eng. Math. **67**, 11–22 (2010).
51. D. H. Peregrine, "Water waves, nonlinear Schrödinger equations and their solutions," The ANZIAM J. **25**, 16–43 (1983).
52. A. Mussot, A. Kudlinski, M. Kolobov, E. Louvergneaux, M. Douay, and M. Taki, "Observation of extreme temporal events in CW-pumped supercontinuum," Opt. Express **17**, 17010–17015 (2009).
53. B. Kibler, J. Fatome, G. Finot, C. Millot, F. Dias, G. Genty, N. Akhmediev, and J. M. Dudley, "The Peregrine soliton in nonlinear fibre optics," Nat. Phys. **6**, 790–795 (2010).
54. A. Chabchoub, N. Hoffmann, and N. Akhmediev, "Rogue wave observation in a water wave tank," Phys. Rev. Lett. **106**, 204502 (2011).
55. A. Chabchoub, N. Akhmediev, and N. Hoffmann, "Experimental study of spatiotemporally localized surface gravity water waves," Phys. Rev. E **86**, 016311 (2012).
56. A. Chabchoub, B. Kibler, J. M. Dudley, and N. Akhmediev, "Hydrodynamics of periodic breathers," Philos. Trans. R. Soc., A **372**, 20140005 (2014).
57. N. Akhmediev, J. M. Soto-Crespo, and A. Ankiewicz, "Extreme waves that appear from nowhere: on the nature of rogue waves," Phys. Lett. A **373**, 2137–2145 (2009).
58. B. Frisquet, B. Kibler, and G. Millot, "Collision of Akhmediev breathers in nonlinear fiber optics," Phys. Rev. X **3**, 041032 (2013).
59. Y. Silberberg, "Collapse of optical pulses," Opt. Lett. **15**, 1282–1284 (1990).
60. L. A. Lugiato and R. Lefever, "Spatial dissipative structures in passive optical systems," Phys. Rev. Lett. **58**, 2209–2211 (1987).
61. A. J. Scroggie, W. J. Firth, G. S. McDonald, M. Tlidi, R. Lefever, and L. A. Lugiato, "Pattern formation in a passive Kerr cavity," Chaos, Solitons Fractals **4**, 1323–1354 (1994).
62. S. S. Gopalakrishnan, K. Panajotov, M. Taki, and M. Tlidi, "Dissipative light bullets in Kerr cavities: multistability, clustering, and rogue waves," Phys. Rev. Lett. **126**, 153902 (2021).
63. F. Leo, S. Coen, P. Kockaert, S.-P. Gorza, P. Emplit, and M. Haelterman, "Temporal cavity solitons in one-dimensional Kerr media as bits in an all-optical buffer," Nat. Photonics **4**, 471–476 (2010).
64. V. Odent, M. Taki, and E. Louvergneaux, "Experimental evidence of dissipative spatial solitons in an optical passive Kerr cavity," New J. Phys. **13**, 113026 (2011).
65. S. Coen, H. G. Randle, T. Sylvestre, and M. Erkintalo, "Modeling of octave-spanning Kerr frequency combs using a generalized mean-field Lugiato–Lefever model," Opt. Lett. **38**, 37–39 (2013).
66. L. Lugiato, F. Prati, M. Gorodetsky, and T. Kippenberg, "From the Lugiato–Lefever equation to microresonator-based soliton Kerr frequency combs," Philos. Trans. R. Soc., A **376**, 20180113 (2018).
67. M. Tlidi, M. Clerc, and K. Panajotov, "Dissipative structures in matter out of equilibrium, from chemistry, photonics and biology, the legacy of Ilya Prigogine (part 1)," (2018).
68. M. Tlidi, M. Clerc, and K. Panajotov, "Dissipative structures in matter out of equilibrium, from chemistry, photonics and biology, the legacy of Ilya Prigogine (part 2)," (2018).
69. T. J. Kippenberg, R. Holzwarth, and S. A. Diddams, "Microresonator-based optical frequency combs," Science **332**, 555–559 (2011).
70. F. Ferdous, H. Miao, D. E. Leaird, K. Srinivasan, J. Wang, L. Chen, L. T. Varghese, and A. M. Weiner, "Spectral line-by-line pulse shaping of on-chip microresonator frequency combs," Nat. Photonics **5**, 770–776 (2011).

71. T. W. Hänsch, "Nobel lecture: passion for precision," Rev. Mod. Phys. **78**, 1297–1309 (2006).
72. F. Arecchi, U. Bortolozzo, A. Montina, and S. Residori, "Granularity and inhomogeneity are the joint generators of optical rogue waves," Phys. Rev. Lett. **106**, 153901 (2011).
73. G.-L. Oppo, A. M. Yao, and D. Cuozzo, "Self-organization, pattern formation, cavity solitons, and rogue waves in singly resonant optical parametric oscillators," Phys. Rev. A **88**, 043813 (2013).
74. C. Liu, R. E. Van Der Wel, N. Rotenberg, L. Kuipers, T. F. Krauss, A. Di Falco, and A. Fratalocchi, "Triggering extreme events at the nanoscale in photonic seas," Nat. Phys. **11**, 358–363 (2015).
75. M. Tlidi, K. Panajotov, M. Ferré, and M. G. Clerc, "Drifting cavity solitons and dissipative rogue waves induced by time-delayed feedback in Kerr optical frequency comb and in all fiber cavities," Chaos **27**, 114312 (2017).
76. H. Soda, K.-i. Iga, C. Kitahara, and Y. Suematsu, "GaInAsP/InP surface emitting injection lasers," Jpn. J. Appl. Phys. **18**, 2329–2330 (1979).
77. T. Ackemann, W. J. Firth, and G.-L. Oppo, "Fundamentals and applications of spatial dissipative solitons in photonic devices," in *Advances in Atomic, Molecular, and Optical Physics*, Vol. 57, P. R. B. E. Arimondo and C. C. Lin, eds. (Academic, 2009), Chap. 6, p. 323.
78. S. Barbay, R. Kuszelewicz, and J. R. Tredicce, "Cavity solitons in VCSEL devices," Adv. Opt. Technol. **2011**, 1–23 (2011).
79. M. Tlidi, K. Staliunas, K. Panajotov, A. G. Vladimirov, and M. G. Clerc, "Localized structures in dissipative media: from optics to plant ecology," Philos. Trans. R. Soc., A **372**, 20140101 (2014).
80. N. Marsal, V. Caullet, D. Wolfersberger, and M. Sciamanna, "Spatial rogue waves in a photorefractive pattern-forming system," Opt. Lett. **39**, 3690–3693 (2014).
81. D. Pierangeli, F. Di Mei, C. Conti, A. J. Agranat, and E. DelRe, "Spatial rogue waves in photorefractive ferroelectrics," Phys. Rev. Lett. **115**, 093901 (2015).
82. J. M. Dudley, G. Genty, and B. J. Eggleton, "Harnessing and control of optical rogue waves in supercontinuum generation," Opt. Express **16**, 3644–3651 (2008).
83. K. Hammani, C. Finot, J. M. Dudley, and G. Millot, "Optical rogue-wave-like extreme value fluctuations in fiber Raman amplifiers," Opt. Express **16**, 16467–16474 (2008).
84. N. N. Akhmediev and A. Ankiewicz, *Solitons: Nonlinear Pulses and Beams* (Chapman & Hall, 1997).
85. A. C. Newell and J. V. Moloney, *Nonlinear Optics* (Addison-Wesley Publishing Company, New York, 1992).
86. L. F. Mollenauer, R. H. Stolen, and J. P. Gordon, "Experimental observation of picosecond pulse narrowing and solitons in optical fibers," Phys. Rev. Lett. **45**, 1095–1098 (1980).
87. P. Emplit, J.-P. Hamaide, F. Reynaud, C. Froehly, and A. Barthelemy, "Picosecond steps and dark pulses through nonlinear single mode fibers," Opt. Commun. **62**, 374–379 (1987).
88. M. Taki, K. Spatschek, J. Fernandez, R. Grauer, and G. Reinisch, "Breather dynamics in the nonlinear Schrödinger regime of perturbed sine-Gordon systems," Phys. D **40**, 65–82 (1989).
89. Y. Kivshar, "Bending light at will," Nat. Phys. **2**, 729–730 (2006).
90. N. Savage, "Supercontinuum sources," Nat. Photonics **3**, 114–115 (2009).
91. T. B. Benjamin, "Instability of periodic wavetrains in nonlinear dispersive systems," Proc. R. Soc. A **299**, 59–76 (1967).
92. V. Bespalov and V. Talanov, "Filamentary structure of light beams in nonlinear liquids," JETP Lett. **3**, 307 (1966).

93. T. Taniuti and H. Washimi, "Self-trapping and instability of hydromagnetic waves along the magnetic field in a cold plasma," Phys. Rev. Lett. **21**, 209–212 (1968).
94. K. Tai, A. Hasegawa, and A. Tomita, "Observation of modulational instability in optical fibers," Phys. Rev. Lett. **56**, 135–138 (1986).
95. G. P. Agrawal, "Nonlinear fiber optics," in *Nonlinear Science at the Dawn of the 21st Century* (Springer, 2000), pp. 195–211.
96. E. Greer, D. Patrick, P. Wigley, and J. Taylor, "Generation of 2 THz repetition rate pulse trains through induced modulational instability," Electron. Lett. **25**, 1246–1248 (1989).
97. R. Stolen and J. Bjorkholm, "Parametric amplification and frequency conversion in optical fibers," IEEE J. Quantum Electron. **18**, 1062–1072 (1982).
98. M. Marhic, N. Kagi, T.-K. Chiang, and L. Kazovsky, "Broadband fiber optical parametric amplifiers," Opt. Lett. **21**, 573–575 (1996).
99. C. Kharif and E. Pelinovsky, "Physical mechanisms of the rogue wave phenomenon," Eur. J. Mech. - B/Fluids **22**, 603–634 (2003).
100. J. M. Dudley, G. Genty, and S. Coen, "Supercontinuum generation in photonic crystal fiber," Rev. Mod. Phys. **78**, 1135–1184 (2006).
101. M. Taki, A. Mussot, A. Kudlinski, E. Louvergneaux, M. Kolobov, and M. Douay, "Third-order dispersion for generating optical rogue solitons," Phys. Lett. A **374**, 691–695 (2010).
102. J. E. Rothenberg, "Modulational instability for normal dispersion," Phys. Rev. A **42**, 682–685 (1990).
103. G. Millot, S. Pitois, P. T. Dinda, and M. Haelterman, "Observation of modulational instability induced by velocity-matched cross-phase modulation in a normally dispersive bimodal fiber," Opt. Lett. **22**, 1686–1688 (1997).
104. J. D. Harvey, R. Leonhardt, S. Coen, G. K. Wong, J. Knight, W. J. Wadsworth, and P. S. J. Russell, "Scalar modulation instability in the normal dispersion regime by use of a photonic crystal fiber," Opt. Lett. **28**, 2225–2227 (2003).
105. S. B. Cavalcanti, J. C. Cressoni, H. R. da Cruz, and A. S. Gouveia-Neto, "Modulation instability in the region of minimum group-velocity dispersion of single-mode optical fibers via an extended nonlinear Schrödinger equation," Phys. Rev. A **43**, 6162–6165 (1991).
106. A. Slunyaev, "A high-order nonlinear envelope equation for gravity waves in finite-depth water," J. Exp. Theor. Phys. **101**, 926–941 (2005).
107. A. Ankiewicz, N. Devine, and N. Akhmediev, "Are rogue waves robust against perturbations?" Phys. Lett. A **373**, 3997–4000 (2009).
108. V. Zakharov and A. Shabat, "Exact theory of two-dimensional self-focusing and one-dimensional self-modulation of waves in nonlinear media," J. Exp. Theor. Phys. **34**, 62 (1972).
109. G. L. Lamb Jr, *Elements of Soliton Theory* (Wiley, New York, 1980).
110. A. C. Newell, *Solitons in Mathematics and Physics* (SIAM, 1985).
111. M. J. Ablowitz and P. A. Clarkson, *Solitons, Nonlinear Evolution Equations and Inverse Scattering* (Cambridge University Press, 1991), Vol. 149.
112. M.-Y. Su, "Three-dimensional deep-water waves. Part 1. Experimental measurement of skew and symmetric wave patterns," J. Fluid Mech. **124**, 73–108 (1982).
113. B. Kibler, A. Chabchoub, A. Gelash, N. Akhmediev, and V. Zakharov, "Superregular breathers in optics and hydrodynamics: omnipresent modulation instability beyond simple periodicity," Phys. Rev. X **5**, 041026 (2015).
114. K. Tai, A. Tomita, J. Jewell, and A. Hasegawa, "Generation of subpicosecond solitonlike optical pulses at 0.3 THz repetition rate by induced modulational instability," Appl. Phys. Lett. **49**, 236–238 (1986).

115. E. N. Lorenz, "Deterministic nonperiodic flow," J. Atmos. Sci. **20**, 130–141 (1963).
116. H. Haken, "Analogy between higher instabilities in fluids and lasers," Phys. Lett. A **53**, 77–78 (1975).
117. M. Brambilla, L. A. Lugiato, V. Penna, F. Prati, C. Tamm, and C. O. Weiss, "Transverse laser patterns. II. Variational principle for pattern selection, spatial multistability, and laser hydrodynamics," Phys. Rev. A **43**, 5114–5120 (1991).
118. R. Lefever, L. A. Lugiato, W. Kaige, N. B. Abraham, and P. Mandel, "Phase dynamics of transverse diffraction patterns in the laser," Phys. Lett. A **135**, 254–258 (1989).
119. K. Staliunas, "Dynamics of optical vortices in a laser beam," Opt. Commun. **90**, 123–127 (1992).
120. P. Mandel, M. Georgiou, and T. Erneux, "Transverse effects in coherently driven nonlinear cavities," Phys. Rev. A **47**, 4277–4286 (1993).
121. Y. Kuramoto, "Diffusion-induced chaos in reaction systems," Prog. Theor. Phys. Suppl. **64**, 346–367 (1978).
122. G. Sivashinsky, "Nonlinear analysis of hydrodynamic instability in laminar flames. Derivation of basic equations," Acta Astronaut. **4**, 1177–1206 (1977).
123. Y. V. Bludov, V. Konotop, and N. Akhmediev, "Matter rogue waves," Phys. Rev. A **80**, 033610 (2009).
124. Y. V. Bludov, V. Konotop, and N. Akhmediev, "Vector rogue waves in binary mixtures of Bose–Einstein condensates," Eur. Phys. J.: Spec. Top. **185**, 169–180 (2010).
125. I. S. Aranson and L. Kramer, "The world of the complex Ginzburg–Landau equation," Rev. Mod. Phys. **74**, 99–143 (2002).
126. K. Staliunas, "Laser Ginzburg–Landau equation and laser hydrodynamics," Phys. Rev. A **48**, 1573–1581 (1993).
127. M. Tlidi, M. Georgiou, and P. Mandel, "Transverse patterns in nascent optical bistability," Phys. Rev. A **48**, 4605–4609 (1993).
128. J. Lega, J. V. Moloney, and A. C. Newell, "Swift–Hohenberg equation for lasers," Phys. Rev. Lett. **73**, 2978–2981 (1994).
129. J. Swift and P. C. Hohenberg, "Hydrodynamic fluctuations at the convective instability," Phys. Rev. A **15**, 319–328 (1977).
130. A. Chabchoub, N. Hoffmann, M. Onorato, and N. Akhmediev, "Super rogue waves: observation of a higher-order breather in water waves," Phys. Rev. X **2**, 011015 (2012).
131. M. L. McAllister, T. A. A. Adcock, P. H. Taylor, and T. S. van den Bremer, "The set-down and set-up of directionally spread and crossing surface gravity wave groups," J. Fluid Mech. **835**, 131–169 (2018).
132. A. R. Osborne, "Nonlinear ocean wave and the inverse scattering transform," in *Scattering* (Elsevier, 2002), pp. 637–666.
133. K. Dysthe, H. E. Krogstad, and P. Muller, "Oceanic rogue waves," Annu. Rev. Fluid Mech. **40**, 287–310 (2008).
134. D. Mihalache, "Linear and nonlinear light bullets: recent theoretical and experimental studies," Rom. J. Phys. **57**, 352–371 (2012).
135. S. Chen, Y. Ye, J. M. Soto-Crespo, P. Grelu, and F. Baronio, "Peregrine solitons beyond the threefold limit and their two-soliton interactions," Phys. Rev. Lett. **121**, 104101 (2018).
136. S. Birkholz, E. T. J. Nibbering, C. Brée, S. Skupin, A. Demircan, G. Genty, and G. Steinmeyer, "Spatiotemporal rogue events in optical multiple filamentation," Phys. Rev. Lett. **111**, 243903 (2013).

137. M. L. McAllister, S. Draycott, T. A. A. Adcock, P. H. Taylor, and T. S. van den Bremer, "Laboratory recreation of the Draupner wave and the role of breaking in crossing seas," J. Fluid Mech. **860**, 767–786 (2019).
138. D. H. Peregrine, "Water-wave impact on walls," Annu. Rev. Fluid Mech. **35**, 23–43 (2003).
139. T. P. Sapsis, "Statistics of extreme events," Annu. Rev. Fluid Mech. **53**, 85–111 (2021).
140. T. A. A. Adcock, P. H. Taylor, S. Yan, Q. W. Ma, and P. A. E. M. Janssen, "Did the Draupner wave occur in a crossing sea?" Proc. R. Soc. London, Ser. A **467**, 3004–3021 (2011).
141. X. Barthelemy, M. L. Banner, W. L. Peirson, F. Fedele, M. Allis, and F. Dias, "On a unified breaking onset threshold for gravity waves in deep and intermediate water depth," J. Fluid Mech. **841**, 463–488 (2018).
142. T. Herr, V. Brasch, J. D. Jost, C. Y. Wang, N. M. Kondratiev, M. L. Gorodetsky, and T. J. Kippenberg, "Temporal solitons in optical microresonators," Nat. Photonics **8**, 145–152 (2014).
143. Y. K. Chembo and C. R. Menyuk, "Spatiotemporal Lugiato–Lefever formalism for Kerr-comb generation in whispering-gallery-mode resonators," Phys. Rev. A **87**, 053852 (2013).
144. M. Tlidi, M. Haelterman, and P. Mandel, "3d patterns and pattern selection in optical bistability," EPL **42**, 505–510 (1998).
145. M. Tlidi, M. Haelterman, and P. Mandel, "Three-dimensional structures in diffractive and dispersive nonlinear ring cavities," Quantum Semiclassical Opt. **10**, 869–878 (1998).
146. G. Morales and Y. Lee, "Ponderomotive-force effects in a nonuniform plasma," Phys. Rev. Lett. **33**, 1016–1019 (1974).
147. K. Nozaki and N. Bekki, "Solitons as attractors of a forced dissipative nonlinear Schrödinger equation," Phys. Lett. A **102**, 383–386 (1984).
148. D. J. Kaup and A. C. Newell, "Theory of nonlinear oscillating dipolar excitations in one-dimensional condensates," Phys. Rev. B **18**, 5162–5167 (1978).
149. M. Haelterman, S. Trillo, and S. Wabnitz, "Dissipative modulation instability in a nonlinear dispersive ring cavity," Opt. Commun. **91**, 401–407 (1992).
150. P. Kockaert, P. Tassin, G. Van der Sande, I. Veretennicoff, and M. Tlidi, "Negative diffraction pattern dynamics in nonlinear cavities with left-handed materials," Phys. Rev. A **74**, 033822 (2006).
151. Z. Ziani, G. Lévêque, A. Akjouj, S. Coulibaly, and A. Taki, "Characterization of spatiotemporal chaos in arrays of nonlinear plasmonic nanoparticles," Phys. Rev. B **100**, 165423 (2019).
152. U. Peschel, O. Egorov, and F. Lederer, "Discrete cavity solitons," in *Nonlinear Guided Waves and Their Applications* (Optical Society of America, 2004), p. WB6.
153. M. Clerc, M. Ferré, S. Coulibaly, R. Rojas, and M. Tlidi, "Chimera-like states in an array of coupled-waveguide resonators," Opt. Lett. **42**, 2906–2909 (2017).
154. M. Clerc, S. Coulibaly, M. Ferré, and M. Tlidi, "Two-dimensional optical chimera states in an array of coupled waveguide resonators," Chaos **30**, 043107 (2020).
155. K. Panajotov, M. Tlidi, Y. Song, and H. Zhang, "Discrete light bullets in coupled optical resonators," Opt. Lett. **46**, 4072–4075 (2021).
156. J. Cuevas-Maraver, P. G. Kevrekidis, and F. Williams, "The sine-Gordon model and its applications," *Nonlinear Systems and Complexity* (Springer, 2014).
157. Y. K. Chembo, D. Gomila, M. Tlidi, and C. R. Menyuk, "Theory and applications of the Lugiato–Lefever equation," Eur. Phys. J. D **71**, 299 (2017).
158. M. Tlidi, M. Le Berre, E. Ressayre, A. Tallet, and L. Di Menza, "High-intensity localized structures in the degenerate optical parametric oscillator: comparison

between the propagation and the mean-field models," Phys. Rev. A **61**, 043806 (2000).
159. X. Dong, C. Spiess, V. G. Bucklew, and W. H. Renninger, "Chirped-pulsed Kerr solitons in the Lugiato–Lefever equation with spectral filtering," Phys. Rev. Res. **3**, 033252 (2021).
160. D. Gomila, A. J. Scroggie, and W. J. Firth, "Bifurcation structure of dissipative solitons," Phys. D **227**, 70–77 (2007).
161. D. Turaev, A. G. Vladimirov, and S. Zelik, "Long-range interaction and synchronization of oscillating dissipative solitons," Phys. Rev. Lett. **108**, 263906 (2012).
162. K. Nozaki and N. Bekki, "Chaotic solitons in a plasma driven by an rf field," J. Phys. Soc. Jpn. **54**, 2363–2366 (1985).
163. K. Nozaki and N. Bekki, "Low-dimensional chaos in a driven damped nonlinear Schrödinger equation," Phys. D **21**, 381–393 (1986).
164. S. Wabnitz, "Suppression of interactions in a phase-locked soliton optical memory," Opt. Lett. **18**, 601–603 (1993).
165. M. A. Ferré, M. G. Clerc, S. Coulibally, R. G. Rojas, and M. Tlidi, "Localized structures and spatiotemporal chaos: comparison between the driven damped sine-Gordon and the Lugiato–Lefever model," Eur. Phys. J. D **71**, 172 (2017).
166. M. Tlidi and L. Gelens, "High-order dispersion stabilizes dark dissipative solitons in all-fiber cavities," Opt. Lett. **35**, 306–308 (2010).
167. P. Parra-Rivas, D. Gomila, M. A. Matías, S. Coen, and L. Gelens, "Dynamics of localized and patterned structures in the Lugiato–Lefever equation determine the stability and shape of optical frequency combs," Phys. Rev. A **89**, 043813 (2014).
168. P. Parra-Rivas, D. Gomila, L. Gelens, and E. Knobloch, "Bifurcation structure of localized states in the Lugiato–Lefever equation with anomalous dispersion," Phys. Rev. E **97**, 042204 (2018).
169. A. Vladimirov, R. Lefever, and M. Tlidi, "Relative stability of multipeak localized patterns of cavity solitons," Phys. Rev. A **84**, 043848 (2011).
170. S. Wabnitz, "Modulational polarization instability of light in a nonlinear birefringent dispersive medium," Phys. Rev. A **38**, 2018–2021 (1988).
171. T. Hansson, M. Bernard, and S. Wabnitz, "Modulational instability of nonlinear polarization mode coupling in microresonators," J. Opt. Soc. Am. B **35**, 835–841 (2018).
172. J. Fatome, B. Kibler, F. Leo, A. Bendahmane, G.-L. Oppo, B. Garbin, S. G. Murdoch, M. Erkintalo, and S. Coen, "Polarization modulation instability in a nonlinear fiber Kerr resonator," Opt. Lett. **45**, 5069–5072 (2020).
173. E. Averlant, M. Tlidi, K. Panajotov, and L. Weicker, "Coexistence of cavity solitons with different polarization states and different power peaks in all-fiber resonators," Opt. Lett. **42**, 2750–2753 (2017).
174. R. Suzuki, S. Fujii, A. Hori, and T. Tanabe, "Theoretical study on dual-comb generation and soliton trapping in a single microresonator with orthogonally polarized dual pumping," IEEE Photonics J. **11**, 1–11 (2019).
175. F. Copie, M. T. Woodley, L. Del Bino, J. M. Silver, S. Zhang, and P. Del'Haye, "Interplay of polarization and time-reversal symmetry breaking in synchronously pumped ring resonators," Phys. Rev. Lett. **122**, 013905 (2019).
176. M. Saha, S. Roy, and S. K. Varshney, "Polarization dynamics of a vector cavity soliton in a birefringent fiber resonator," Phys. Rev. A **101**, 033826 (2020).
177. P. Parra-Rivas, E. Knobloch, D. Gomila, and L. Gelens, "Dark solitons in the Lugiato–Lefever equation with normal dispersion," Phys. Rev. A **93**, 063839 (2016).

178. P. Parra-Rivas, D. Gomila, and L. Gelens, "Coexistence of stable dark-and bright-soliton Kerr combs in normal-dispersion resonators," Phys. Rev. A **95**, 053863 (2017).
179. P. Parra-Rivas, D. Gomila, F. Leo, S. Coen, and L. Gelens, "Third-order chromatic dispersion stabilizes Kerr frequency combs," Opt. Lett. **39**, 2971–2974 (2014).
180. M. Clerc, S. Coulibaly, and M. Tlidi, "Time-delayed nonlocal response inducing traveling temporal localized structures," Phys. Rev. Res. **2**, 013024 (2020).
181. M. G. Clerc, S. Coulibaly, P. Parra-Rivas, and M. Tlidi, "Nonlocal Raman response in Kerr resonators: Moving temporal localized structures and bifurcation structure," Chaos **30**, 083111 (2020).
182. P. Parra-Rivas, S. Coulibaly, M. Clerc, and M. Tlidi, "Influence of stimulated Raman scattering on Kerr domain walls and localized structures," Phys. Rev. A **103**, 013507 (2021).
183. B. Kostet, S. Gopalakrishnan, E. Averlant, Y. Soupart, K. Panajotov, and M. Tlidi, "Vectorial dark dissipative solitons in Kerr resonators," OSA Continuum **4**, 1564–1570 (2021).
184. B. Kostet, Y. Soupart, K. Panajotov, and M. Tlidi, "Coexistence of dark vector soliton Kerr combs in normal dispersion resonators," Phys. Rev. A **104**, 053530 (2021).
185. P. Coullet, C. Elphick, and D. Repaux, "Nature of spatial chaos," Phys. Rev. Lett. **58**, 431–434 (1987).
186. P. Coullet, "Localized patterns and fronts in nonequilibrium systems," Int. J. Bifurcation Chaos Appl. Sci. Eng. **12**, 2445–2457 (2002).
187. A. M. Turing, "The chemical basis of morphogenesis," Phil. Trans. R. Soc. B **237**, 37–72 (1952).
188. I. Prigogine and R. Lefever, "Symmetry breaking instabilities in dissipative systems," J. Chem. Phys. **48**, 1695–1700 (1968).
189. P. Glansdorff and I. Prigogine, *Thermodynamic Theory of Structure, Stability and Fluctuations* (Wiley, 1971).
190. G. Nicolis and I. Prigogine, *Self-Organization in Nonequibrium Systems* (Wiley-Interscience, 1977).
191. H. Haken, *Synergetics. An Introduction. Nonequilibrium Phase Trasitions and Self-Organization in Physics, Chemistry, and Biology* (Springer, 1977).
192. M. C. Cross and P. C. Hohenberg, "Pattern formation outside of equilibrium," Rev. Mod. Phys. **65**, 851–1112 (1993).
193. J. D. Murray, *Mathematical Biology*, Vol. 19 of Biomathematics (Springer, 1989).
194. K. Staliunas and V. Sánchez-Morcillo, *Transverse Patterns in Nonlinear Optical Resonators*, Springer Tracts in Modern Physics (Springer, 2003).
195. F. Arecchi, S. Boccaletti, and P. Ramazza, "Pattern formation and competition in nonlinear optics," Phys. Rep. **318**, 1–83 (1999).
196. L. Lugiato, F. Prati, and M. Brambilla, *Nonlinear Optical Systems* (Cambridge University Press, 2015).
197. M. Tlidi and M. G. Clerc, *Nonlinear Dynamics: Materials, Theory and Experiments* (Springer Proceedings in Physics, Springer, 2016), Vol. 173.
198. R. Lefever, "The rehabilitation of irreversible processes and dissipative structures' 50th anniversary," Philos. Trans. R. Soc., A **376**, 20170365 (2018).
199. H. Bénard, "Les tourbillons cellulaires dans une nappe liquide propageant de la chaleur par convection, en régime permanent," Ph.D. thesis (Université de Paris, 1901). These de doctorat Sciences physiques Faculté des sciences de l'Université de Paris 1901.
200. S. Coen and M. Haelterman, "Modulational instability induced by cavity boundary conditions in a normally dispersive optical fiber," Phys. Rev. Lett. **79**, 4139–4142 (1997).

201. W. Firth, A. Scroggie, G. McDonald, and L. Lugiato, "Hexagonal patterns in optical bistability," Phys. Rev. A **46**, R3609–R3612 (1992).
202. M. Tlidi, R. Lefever, and P. Mandel, "Pattern selection in optical bistability," Quantum Semiclassical Opt. **8**, 931–938 (1996).
203. M. Tlidi, "Three-dimensional crystals and localized structures in diffractive and dispersive nonlinear ring cavities," J. Opt. B **2**, 438–442 (2000).
204. M. Tlidi, S. Gopalakrishnan, M. Taki, and K. Panajotov, "Optical crystals and light-bullets in Kerr resonators," Chaos, Solitons Fractals **152**, 111364 (2021).
205. W. B. Jones and J. O'Brian, "Pseudo-spectral methods and linear instabilities in reaction-diffusion fronts," Chaos **6**, 219–228 (1996).
206. A. Kassam, *High Order Timestepping for Stiff Semilinear Partial Differential Equations* (University of Oxford, 2004).
207. L. N. Trefethen, *Spectral Methods in MATLAB* (SIAM, 2000).
208. Y. Saad, *Numerical Methods for Large Eigenvalue Problems* (SIAM, 2011).
209. F. Mitschke, G. Steinmeyer, and A. Schwache, "Generation of one-dimensional optical turbulence," Phys. D **96**, 251–258 (1996).
210. G. Steinmeyer, A. Schwache, and F. Mitschke, "Quantitative characterization of turbulence in an optical experiment," Phys. Rev. E **53**, 5399–5402 (1996).
211. Y. K. Chembo, D. V. Strekalov, and N. Yu, "Spectrum and dynamics of optical frequency combs generated with monolithic whispering gallery mode resonators," Phys. Rev. Lett. **104**, 103902 (2010).
212. M. Anderson, F. Leo, S. Coen, M. Erkintalo, and S. G. Murdoch, "Observations of spatiotemporal instabilities of temporal cavity solitons," Optica **3**, 1071–1074 (2016).
213. K. Panajotov, M. G. Clerc, and M. Tlidi, "Spatiotemporal chaos and two-dimensional dissipative rogue waves in Lugiato–Lefever model," Eur. Phys. J. D **71**, 176 (2017).
214. P. Manneville, *Dissipative Structures and Weak Turbulence* (Academic, San Diego, 1990).
215. D. Ruelle, "Large volume limit of the distribution of characteristic exponents in turbulence," Commun. Math. Phys. **87**, 287–302 (1982).
216. A. Pikovsky and A. Politi, *Lyapunov Exponents: A Tool to Explore Complex Dynamics* (Cambridge Univ. Press, 2016).
217. Z. Liu, M. Ouali, S. Coulibaly, M. Clerc, M. Taki, and M. Tlidi, "Characterization of spatiotemporal chaos in a Kerr optical frequency comb and in all fiber cavities," Opt. Lett. **42**, 1063–1066 (2017).
218. E. Ott, *Chaos in Dynamical Systems* (Cambridge Univ.Press, 2002).
219. P. Constantin, C. Foiaş, and R. Temam, *Attractors Representing Turbulent Flows* (American Mathematical Soc., 1985), Vol. 314.
220. D. A. Egolf and H. S. Greenside, "Relation between fractal dimension and spatial correlation length for extensive chaos," Nature **369**, 129–131 (1994).
221. T. Bohr and E. B. W. van de Water, "Spatiotemporal chaos," Nature **372**, 48 (1994).
222. D. A. Egolf and H. S. Greenside, "Characterization of the transition from defect to phase turbulence," Phys. Rev. Lett. **74**, 1751–1754 (1995).
223. A. Coillet, J. Dudley, G. Genty, L. Larger, and Y. K. Chembo, "Optical rogue waves in whispering-gallery-mode resonators," Phys. Rev. A **89**, 013835 (2014).
224. S. Coulibaly, M. Taki, A. Bendahmane, G. Millot, B. Kibler, and M. G. Clerc, "Turbulence-induced rogue waves in Kerr resonators," Phys. Rev. X **9**, 011054 (2019).
225. A. Montina, U. Bortolozzo, S. Residori, and F. T. Arecchi, "Non-Gaussian statistics and extreme waves in a nonlinear optical cavity," Phys. Rev. Lett. **103**, 173901 (2009).

226. S. Residori, U. Bortolozzo, A. Montina, F. Lenzini, and F. Arecchi, "Rogue waves in spatially extended optical systems," Fluct. Noise Lett. **11**, 1240014 (2012).
227. M. Bache, F. Prati, G. Tissoni, R. Kheradmand, L. Lugiato, I. Protsenko, and M. Brambilla, "Cavity soliton laser based on VCSEL with saturable absorber," Appl. Phys. B **81**, 913–920 (2005).
228. K. Panajotov and M. Tlidi, "Chaotic behavior of cavity solitons induced by time delay feedback," Opt. Lett. **39**, 4739–4742 (2014).
229. M. Tlidi and K. Panajotov, "Cavity solitons: dissipative structures in nonlinear photonics," Rom. Rep. Phys. **70**, 406 (2018).
230. N. N. Rozanov, "Kinetics of a solid-state laser with an additional moving mirror," Sov. J. Quantum Electron. **4**, 1191–1193 (1975).
231. R. Lang and K. Kobayashi, "External optical feedback effects on semiconductor injection laser properties," IEEE J. Quantum Electron. **16**, 347–355 (1980).
232. V.-C. S.-E. L. Devices, *Springer Series in Photonics*, H. Li and K. Iga, eds. (Springer-Verlag, 2002), Vol. 6, p. 133.
233. R. Michalzik, "Vcsel fundamentals," in *VCSELs* (Springer, 2013), pp. 19–75.
234. V. Taranenko, I. Ganne, R. Kuszelewicz, and C. Weiss, "Spatial solitons in a semiconductor microresonator," Appl. Phys. B **72**, 377–380 (2001).
235. S. Barland, J. R. Tredicce, M. Brambilla, L. A. Lugiato, S. Balle, M. Giudici, T. Maggipinto, L. Spinelli, G. Tissoni, T. Knoedl, M. Miller, and R. Jäger, "Cavity solitons as pixels in semiconductor microcavities," Nature **419**, 699–702 (2002).
236. X. Hachair, S. Barland, L. Furfaro, M. Giudici, S. Balle, J. R. Tredicce, M. Brambilla, T. Maggipinto, I. M. Perrini, G. Tissoni, and L. Lugiato, "Cavity solitons in broad-area vertical-cavity surface-emitting lasers below threshold," Phys. Rev. A **69**, 043817 (2004).
237. X. Hachair, F. Pedaci, E. Caboche, S. Barland, M. Giudici, J. Tredicce, F. Prati, G. Tissoni, R. Kheradmand, L. A. Lugiato, I. Protsenko, and M. Brambilla, "Cavity solitons in a driven VCSEL above threshold," IEEE J. Sel. Top. Quantum Electron. **12**, 339–351 (2006).
238. E. Averlant, M. Tlidi, H. Thienpont, T. Ackemann, and K. Panajotov, "Experimental observation of localized structures in medium size VCSELs," Opt. Express **22**, 762–772 (2014).
239. E. Averlant, M. Tlidi, H. Thienpont, T. Ackemann, and K. Panajotov, "Vector cavity solitons in broad area vertical-cavity surface-emitting lasers," Sci. Rep. **6**, 20428 (2016).
240. N. Rosanov and S. Fedorov, "Diffractive switching waves and autosolitons in laser with saturable absorber," Opt. Spectrosc. **72**, 1394–1399 (1992).
241. V. Taranenko, K. Staliunas, and C. Weiss, "Spatial soliton laser: Localized structures in a laser with a saturable absorber in a self-imaging resonator," Phys. Rev. A **56**, 1582–1591 (1997).
242. P. Genevet, S. Barland, M. Giudici, and J. R. Tredicce, "Cavity soliton laser based on mutually coupled semiconductor microresonators," Phys. Rev. Lett. **101**, 123905 (2008).
243. Y. Tanguy, T. Ackemann, W. Firth, and R. Jäger, "Realization of a semiconductor-based cavity soliton laser," Phys. Rev. Lett. **100**, 013907 (2008).
244. T. Elsass, K. Gauthron, G. Beaudoin, I. Sagnes, R. Kuszelewicz, and S. Barbay, "Fast manipulation of laser localized structures in a monolithic vertical cavity with saturable absorber," Appl. Phys. B **98**, 327–331 (2010).
245. K. Panajotov and F. Prati, "Polarization dynamics of vcsels," in *VCSELs* (Springer, 2013), pp. 181–231.
246. X. Hachair, G. Tissoni, H. Thienpont, and K. Panajotov, "Linearly polarized bistable localized structure in medium-size vertical-cavity surface-emitting lasers," Phys. Rev. A **79**, 011801 (2009).

247. G. J. de Valcárcel and K. Staliunas, "Excitation of phase patterns and spatial solitons via two-frequency forcing of a 1:1 resonance," Phys. Rev. E **67**, 026604 (2003).
248. G. J. de Valcárcel and K. Staliunas, "Pattern formation through phase bistability in oscillatory systems with space-modulated forcing," Phys. Rev. Lett. **105**, 054101 (2010).
249. C. Fernandez-Oto, G. De Valcárcel, M. Tlidi, K. Panajotov, and K. Staliunas, "Phase-bistable patterns and cavity solitons induced by spatially periodic injection into vertical-cavity surface-emitting lasers," Phys. Rev. A **89**, 055802 (2014).
250. M. Tlidi, A. Vladimirov, D. Pieroux, and D. Turaev, "Spontaneous motion of cavity solitons induced by a delayed feedback," Phys. Rev. Lett. **103**, 103904 (2009).
251. K. Panajotov and M. Tlidi, "Spontaneous motion of cavity solitons in vertical-cavity lasers subject to optical injection and to delayed feedback," Eur. Phys. J. D **59**, 67–72 (2010).
252. M. Tlidi, E. Averlant, A. Vladimirov, and K. Panajotov, "Delay feedback induces a spontaneous motion of two-dimensional cavity solitons in driven semiconductor microcavities," Phys. Rev. A **86**, 033822 (2012).
253. A. Pimenov, A. G. Vladimirov, S. V. Gurevich, K. Panajotov, G. Huyet, and M. Tlidi, "Delayed feedback control of self-mobile cavity solitons," Phys. Rev. A **88**, 053830 (2013).
254. A. Vladimirov, A. Pimenov, S. Gurevich, K. Panajotov, E. Averlant, and M. Tlidi, "Cavity solitons in vertical-cavity surface-emitting lasers," Philos. Trans. R. Soc., A **372**, 20140013 (2014).
255. C. Bonatto, M. Feyereisen, S. Barland, M. Giudici, C. Masoller, J. R. R. Leite, and J. R. Tredicce, "Deterministic optical rogue waves," Phys. Rev. Lett. **107**, 053901 (2011).
256. J. Zamora-Munt, B. Garbin, S. Barland, M. Giudici, J. R. R. Leite, C. Masoller, and J. R. Tredicce, "Rogue waves in optically injected lasers: origin, predictability, and suppression," Phys. Rev. A **87**, 035802 (2013).
257. A. N. Pisarchik, R. Jaimes-Reátegui, R. Sevilla-Escoboza, G. Huerta-Cuellar, and M. Taki, "Rogue waves in a multistable system," Phys. Rev. Lett. **107**, 274101 (2011).
258. J. A. Reinoso, J. Zamora-Munt, and C. Masoller, "Extreme intensity pulses in a semiconductor laser with a short external cavity," Phys. Rev. E **87**, 062913 (2013).
259. S. Coulibaly, M. Clerc, F. Selmi, and S. Barbay, "Extreme events following bifurcation to spatiotemporal chaos in a spatially extended microcavity laser," Phys. Rev. A **95**, 023816 (2017).
260. S. Barbay, S. Coulibaly, and M. G. Clerc, "Alternation of defects and phase turbulence induces extreme events in an extended microcavity laser," Entropy **20**, 789 (2018).
261. Y.-Y. Tsai, J.-Y. Tsai, and I. Lin, "Generation of acoustic rogue waves in dusty plasmas through three-dimensional particle focusing by distorted waveforms," Nat. Phys. **12**, 573–577 (2016).
262. J. Williams, "Plasma physics: rogue waves caught in 3D," Nat. Phys. **12**, 529–530 (2016).
263. M. Leonetti and C. Conti, "Observation of three dimensional optical rogue waves through obstacles," Appl. Phys. Lett. **106**, 254103 (2015).
264. R. Höhmann, U. Kuhl, H.-J. Stöckmann, L. Kaplan, and E. Heller, "Freak waves in the linear regime: a microwave study," Phys. Rev. Lett. **104**, 093901 (2010).

265. N. Akhmediev and J. Soto-Crespo, "Generation of a train of three-dimensional optical solitons in a self-focusing medium," Phys. Rev. A **47**, 1358–1364 (1993).
266. K. Staliunas, "Three-dimensional turing structures and spatial solitons in optical parametric oscillators," Phys. Rev. Lett. **81**, 81–84 (1998).
267. P. Lushnikov and M. Saffman, "Collapse in a forced three-dimensional nonlinear Schrödinger equation," Phys. Rev. E **62**, 5793–5796 (2000).
268. P. Drummond, H. He, and M. Werner, "Simultaneus solitary-wave solutions in a non-linear parametric waveguide," Phys. Rev. E **54**, 896–911 (1996).
269. B. A. Malomed, P. Drummond, H. He, A. Berntson, D. Anderson, and M. Lisak, "Spatiotemporal solitons in multidimensional optical media with a quadratic nonlinearity," Phys. Rev. E **56**, 4725–4735 (1997).
270. D. V. Skryabin and W. J. Firth, "Dynamics of self-trapped beams with phase dislocation in saturable kerr and quadratic nonlinear media," Phys. Rev. E **58**, 3916–3930 (1998).
271. D. V. Skryabin and W. J. Firth, "Generation and stability of optical bullets in quadratic nonlinear media," Opt. Commun. **148**, 79–84 (1998).
272. D. Mihalache, D. Mazilu, L.-C. Crasovan, I. Towers, A. Buryak, B. A. Malomed, L. Torner, J. Torres, and F. Lederer, "Stable spinning optical solitons in three dimensions," Phys. Rev. Lett. **88**, 073902 (2002).
273. D. Mihalache, D. Mazilu, J. Dörring, and L. Torner, "Elliptical light bullets," Opt. Commun. **159**, 129–138 (1999).
274. A. Kanashov and A. Rubenchik, "On diffraction and dispersion effect on three wave interaction," Phys. D **4**, 122–134 (1981).
275. N. Veretenov and M. Tlidi, "Dissipative light bullets in an optical parametric oscillator," Phys. Rev. A **80**, 023822 (2009).
276. M. Tlidi and P. Mandel, "Three-dimensional optical crystals and localized structures in cavity second harmonic generation," Phys. Rev. Lett. **83**, 4995–4998 (1999).
277. S. V. Fedorov, N. N. Rosanov, A. N. Shatsev, N. A. Veretenov, and A. G. Vladimirov, "Topologically multicharged and multihumped rotating solitons in wide-aperture lasers with a saturable absorber," IEEE J. Quantum Electron. **39**, 197–205 (2003).
278. N. N. Rosanov, S. V. Fedorov, and N. A. Veretenov, "Laser solitons in 1D, 2D and 3D," Eur. Phys. J. D **73**, 141 (2019).
279. J. Javaloyes, "Cavity light bullets in passively mode-locked semiconductor lasers," Phys. Rev. Lett. **116**, 043901 (2016).
280. F. Dohmen, J. Javaloyes, and S. V. Gurevich, "Bound states of light bullets in passively mode-locked semiconductor lasers," Chaos **30**, 063120 (2020).
281. E. G. Fedorov, A. V. Zhukov, R. Bouffanais, N. N. Konobeeva, E. V. Boroznina, B. A. Malomed, H. Leblond, D. Mihalache, M. B. Belonenko, N. N. Rosanov, and T. F. George, "External light control of three-dimensional ultrashort far-infrared pulses in an inhomogeneous array of carbon nanotubes," Phys. Rev. B **103**, 085111 (2021).
282. C. Milián, Y. V. Kartashov, and L. Torner, "Robust ultrashort light bullets in strongly twisted waveguide arrays," Phys. Rev. Lett. **123**, 133902 (2019).
283. M. Brambilla, T. Maggipinto, G. Patera, and L. Columbo, "Cavity light bullets: Three-dimensional localized structures in a nonlinear optical resonator," Phys. Rev. Lett. **93**, 203901 (2004).
284. L. Columbo, I. Perrini, T. Maggipinto, and M. Brambilla, "3d self-organized patterns in the field profile of a semiconductor resonator," New J. Phys. **8**, 312 (2006).
285. N. N. Rosanov, *Spatial Hysteresis and Optical Patterns*, Springer Series in Synergetics (Springer, 2002).

286. A. V. Buryak, P. Di Trapani, D. V. Skryabin, and S. Trillo, "Optical solitons due to quadratic nonlinearities: from basic physics to futuristic applications," Phys. Rep. **370**, 63–235 (2002).
287. B. A. Malomed, D. Mihalache, F. Wise, and L. Torner, "Spatiotemporal optical solitons," J. Opt. B **7**, R53–R72 (2005).
288. A. Champneys, "Homoclinic orbits in reversible systems and their applications in mechanics, fluids and optics," Phys. D **112**, 158–186 (1998).
289. G. W. Hunt, G. J. Lord, and A. Champneys, "Homoclinic and heteroclinic orbits underlying the post-buckling of axially-compressed cylindrical shells," Comput. Methods Appl. Mech. Eng. **170**, 239–251 (1999).
290. P. Woods and A. Champneys, "Heteroclinic tangles and homoclinic snaking in the unfolding of a degenerate reversible Hamiltonian–Hopf bifurcation," Phys. D **129**, 147–170 (1999).
291. P. Coullet, C. Riera, and C. Tresser, "Stable static localized structures in one dimension," Phys. Rev. Lett. **84**, 3069–3072 (2000).
292. J. Burke and E. Knobloch, "Localized states in the generalized Swift–Hohenberg equation," Phys. Rev. E **73**, 056211 (2006).
293. J. Burke and E. Knobloch, "Homoclinic snaking: structure and stability," Chaos **17**, 037102 (2007).
294. A. Champneys, "Editorial to homoclinic snaking at 21: in memory of Patrick Woods," (2021).
295. P. Parra-Rivas, E. Knobloch, L. Gelens, and D. Gomila, "Origin, bifurcation structure and stability of localized states in kerr dispersive optical cavities," IMA J. Appl. Maths **86**, 856–895 (2021).
296. D. C. Bentley and A. M. Rucklidge, "Localized patterns in a generalized Swift–Hohenberg equation with a quartic marginal stability curve," IMA J. Appl. Maths **86**, 944–983 (2021).
297. A. Zakery, *Optical Nonlinearities in Chalcogenide Glasses and Their Applications* (Springer, 2007).
298. G. Snopatin, V. Shiryaev, V. Plotnichenko, E. Dianov, and M. Churbanov, "High-purity chalcogenide glasses for fiber optics," Inorg. Mater. **45**, 1439–1460 (2009).
299. G. Dematteis, T. Grafke, and E. Vanden-Eijnden, "Rogue waves and large deviations in deep sea," Proc. Natl. Acad. Sci. **115**, 855–860 (2018).
300. G. Dematteis, T. Grafke, M. Onorato, and E. Vanden-Eijnden, "Experimental evidence of hydrodynamic instantons: the universal route to rogue waves," Phys. Rev. X **9**, 041057 (2019).
301. R. RajaRaman, *Solitons and Instantons; an Introduction to Solitons and Instantons in Quantum Field Theory* (North-Holland, 1982).
302. T. Schäfer and E. V. Shuryak, "Instantons in QCD," Rev. Mod. Phys. **70**, 323–425 (1998).

Mustapha Tlidi was born in Morocco. He received MD and PhD degrees in physics from the science faculty of the Université Libre de Bruxelles (ULB), Belgium, in 1989 and 1995, respectively. He is a research director with the Belgian National Science Foundation and Professor at ULB. His research focus is on systems far from equilibrium, nonlinear physics, laser physics, nonlinear optics, and plant ecology. He is the head of Physics of Dynamical Systems at ULB. He is currently teaching nonlinear optics, fiber optics, and laser dynamics at the master's level at the Physics Department, and general physics in the faculty of science and the faculty of Pharmacie.

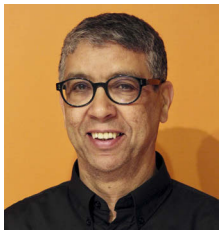

Majid Taki was born in Marrakesh, Morocco. He received the PhD degree in Physics from the University of Sophia Antipolis, Nice, France. His research interests are focused on superconductivity. He had a postdoctoral position at the University of Düsseldorf, Germany, and worked on the physics of plasma. Since 1989, he has been working at the Laboratoire de Physique des Lasers, Atomes et Molècules (PhLAM) and is a full Professor of Physics at the University of Lille. His main research interests deal with nonlinear optics, rogue waves, solitons and spatiotemporal chaos and turbulence in nonlinear spatially extended systems including fiber systems (optical cavities), optical parametric oscillators, and laser systems. He has supervised more than 12 PhDs and published more than 90 articles in peer-reviewed international journals, 80 conferences with 40 as an invited speaker. He is member of Scientific Committee of International Conference (Nonlinear Photonics) and Editor of the review *Nonlinear Science Letters B: Chaos, Fractal and Synchronization*. He conducts several national and international collaborations in Europe, USA, Australia, Mexico, and Chili. He is Head of the Nonlinear Optics and Photonics group at PhLAM laboratory, which belongs to French National Center of Scientific Research (CNRS).